OVERALL EFFECTIVENESS MEASUREMENTS AT ENGINE TEMPERATURES WITH REACTIVE FILM COOLING AND SURFACE CURVATURE

THESIS

Andrew J. Lynch, Second Lieutenant, USAF

AFIT-ENY-MS-15-M-244

DEPARTMENT OF THE AIR FORCE
AIR UNIVERSITY

AIR FORCE INSTITUTE OF TECHNOLOGY

Wright-Patterson Air Force Base, Ohio

AFIT-ENY-MS-15-M-244

OVERALL EFFECTIVENESS MEASUREMENTS AT ENGINE TEMPERATURES WITH REACTIVE FILM COOLING AND SURFACE CURVATURE

THESIS

Presented to the Faculty

Department of Aeronautics and Astronautics

Graduate School of Engineering and Management

Air Force Institute of Technology

Air University

Air Education and Training Command

In Partial Fulfillment of the Requirements for the

Degree of Master of Science in Aeronautical Engineering

Andrew J. Lynch, B.S.M.E.

Second Lieutenant, USAF

March 2015

AFIT-ENY-MS-15-M-244

OVERALL EFFECTIVENESS MEASUREMENTS AT ENGINE TEMPERATURES WITH REACTIVE FILM COOLING AND SURFACE CURVATURE

Andrew J. Lynch, B.S.M.E.

Second Lieutenant, USAF

Committee Membership:

Dr. M. D. Polanka
Chair

Maj J. L. Rutledge, PhD
Member

Maj D. Liu, PhD
Member

AFIT-ENY-MS-15-*M*-244

Abstract

The thesis presented here details the design, construction and initial testing of a rig for use with high temperature film cooling testing. The film cooling rig was supplied with hot mainstream gas from a well-stirred reactor operating on a propane/air mixture capable of multiple equivalence ratios. The Hastelloy test plates contained an internal cooling channel to allow for overall effectiveness measurements. Thermocouples on both the freestream and internal surfaces of the test plate provided temperature differences for heat flux calculations. The test plates had a quarter circle leading edge with a tapered trailing edge to provide surface curvature for the film cooling studies. The height of the test channel could be adjusted for multiple Mach numbers to be set for the mainstream flow. Using a plate containing five rows of holes in trenches and two rows of showerhead holes, methodology was developed for collecting and analyzing the necessary data to obtain net heat flux reduction and overall effectiveness results. This methodology was then applied to the same plate to gather comparative results for reacting versus non-reacting film cooling. It was discovered blowing ratios greater than unity were required to provide protection to the plate with reactive film, but the flame sheet at these blowing ratios extended more than 0.5 chord lengths past the trailing edge of the plate raising concerns for downstream cascades

Acknowledgments

First, I would like to thank my wife for putting up with all those nights I sat at my computer working on my thesis instead of spending time with her. Thank you to Dr. Polanka for his patience and guidance through this research process. Thank you to Andrew Shewhart, Capt Greiner, and Richard Zehring for their expertise with this research and a similar version of the test facility. A special thank you to ISSI for funding the manufacturing of the film cooling test plates. Finally, thank you to anyone who had to sit in the lab for hours with nothing to do so I could run my tests.

Table of Contents

Page

List of Figures

Page

List of Tables

Page

Nomenclature

γ	=	ratio of specific heats
η	=	adiabatic effectiveness
ρ	=	density
Φ	=	equivalence ratio
ϕ	=	overall effectiveness
τ	=	characteristic time
2r/*D*	=	radius of curvature to hole diameter
AFB	=	air force base
AFRL	=	Air Force Research Laboratory
A	=	area
a	=	speed of sound
C_p	=	specific heat
C	=	Celsius
CDAC	=	COAL Lab data acquisitions computer
CFD	=	computational fluid dynamics
COAL	=	combustion analysis laboratory
CRVP	=	counter-rotating vortex pairs
D	=	hole diameter
Da	=	Damkohler number $\left(\frac{\tau_{flow}}{\tau_{chem}}\right)$
DR	=	density ratio
F	=	Fahrenheit
FCR	=	film cooling rig
H*	=	non-dimensional fuel enthalpy
h	=	convective heat transfer coefficient
HCR	=	heat capacity ratio
I	=	momentum flux ratio
IR	=	infrared
K	=	Kelvin
k	=	thermal conductivity
M	=	blowing ratio, mass flux ratio
Ma	=	Mach number
$\dot{m}$	=	mass flow rate
NHFR	=	Net Heat Flux Reduction
P	=	pitch
p	=	static pressure
PIV	=	particle image velocimetry
PLIF	=	planar laser-induced fluorescence
Pr	=	Prandtl number ($c_p\mu/k$)
q"	=	heat flux
RF	=	recovery factor
Re	=	Reynolds number ($\rho Ux/\mu$)
SLR	=	single-lens reflex

T	=	temperature
t	=	thickness
U	=	flow velocity
UCC	=	ultra-compact combustor
VR	=	velocity ratio
WSR	=	well-stirred reactor
x	=	distance

Subscripts

0	=	no cooling
∞	=	freestream
ad	=	adiabatic flame
aw	=	adiabatic wall
c	=	coolant
chem	=	chemical
film	=	film
flow	=	flow
s	=	surface
t	=	total or stagnation

1. Introduction

The research presented in this paper deals with the cooling of turbine blades in a jet turbine engine. The basic design of such an engine involves compressing air through a series of compressor stages, adding and combusting a fuel in this higher pressure state, then expanding the combustion products through one or more turbine stages which are used to power the compressor stages and provide work output to a shaft. Demand for higher efficiency engines has driven the turbine inlet temperature beyond the material limits of the turbine components. To use existing material technologies at these high operating temperatures requires methods of reducing the wall temperature of the turbine components.

1.1 Background

Since the jet turbine engine was originally developed, designers have been seeking ways to increase the power to weight ratios, and the efficiencies of the engines. In a real engine this requires operating the engine at higher temperatures. Manufactures soon found themselves faced with the thermal material limits of the available materials for use in the turbine blades. Without a method of suppressing the blade material temperature, higher levels of engine efficiency could not be reached.

The use of film cooling and research into its properties and mechanisms has been studied for many decades. However, as engine manufactures push towards higher fuel/air ratios, higher temperatures, and higher pressures in the engine, the possibility of incomplete combustion species entering the turbine increases as well. This has a negative consequence of allowing combustion to occur within the film cooling layer due to the oxygen content within the cooling flow. Since the objective of a film layer is to remain

attached to the blade surface, any flame produced by a reaction between the coolant and the mainstream gases would occur adjacent to the blade surface. Thus the challenge is to protect the blade from the nearby presence of this flame.

A majority of film cooling studies have been conducted at either low temperatures, or over flat plates. Additionally, the mainstream Mach number in many of these studies were well below unity. These studies did provide excellent insight into the underlying fluid physics affecting film cooling, but their use for reactive film is limited. Previous studies into reactive film layers have determined it is possible to protect and cool the blade wall by using film cooling schemes which produce well developed, even sheets of coolant air. However, there exists little data regarding reactive film cooling protection schemes over a curved surface, and the effects of Mach number on the film flame dynamics and structure.

1.2 Objectives

There were three primary objectives of this thesis. First, finish the design and construction of a test rig capable of testing reactive and non-reactive film cooling schemes over a surface with curvature at multiple Mach numbers with a engine representative temperatures. Second, develop the data acquisition methods required to obtain net heat flux reduction and overall effectiveness values for various cooling schemes. Third, apply the reduction techniques for evaluating and comparing film cooling results at these elevated temperatures when the thermal conditions are properly matched for reactive and non-reactive film.

2. Literature Review

Film cooling became a major means to cool turbine blades starting in the 1970's. Using air from the high pressure compressor to provide this cooling air decreases the engine's overall efficiency, so optimizing film cooling schemes for maximum protection with the least amount of air is the driving objective for film cooling. The majority of the research in film cooling has been conducted at temperatures close to ambient. These conditions are not representative of an actual aircraft jet engine which is operated at high temperatures, pressures, and Mach numbers. However, low temperature and flat plate experiments are simpler to conduct, and yield some comparative results, but they do not match realistic operating conditions. As engine temperatures and pressures are pushed higher to achieve better engine efficiencies, there is the chance of unburned fuel species reacting with the film cooling layer and producing a flame near the blade and liner surfaces. Some of these effects have been recently studied at AFIT. The goal of this thesis is to extend this research and examine the effects of surface curvature and Mach number on this reactive film by building a new testing facility capable of studying the effects of these parameters.

2.1 Basics of Film Cooling:

A number of important parameters and equations have been identified for the study of film cooling. As the goal of film cooling is to reduce convective heat flux to the turbine blade surface, the primary governing equation is Newton's Law of Cooling as given by Equation 2-1.

$$q'' = h(T_{film} - T_s) \qquad \text{Equation 2-1}$$

q'' is the heat flux into the surface, h is the convective heat transfer coefficient, T_s is the surface temperature, and T_{film} is the temperature of the film layer. Bogard and Thole [1], and Dittmar *et al.* [2] note the difficulty in using Newton's Law of Cooling comes from the elusive nature of measuring both h and T_{film}. h is highly dependent on the geometry of the surface and the freestream flow conditions. Furthermore, h is not a constant value from upstream to downstream locations. It is higher near the leading edge than it is at the trailing edge [3] On a surface with no film cooling, $T_{film} = T_\infty$ where T_∞ is the freestream temperature. However, with film cooling, T_{film} is somewhere between the coolant temperature (T_c) and T_∞. A common temperature used for T_{film} is the temperature of the wall required for an adiabatic wall (T_{aw}).

T_{aw} is the temperature the wall would achieve if there was no heat transfer through it, thus it is called an adiabatic wall temperature. It is important to note the adiabatic wall temperature is affected by the Mach number of the main stream flow through the recovery factor (RF) for T_∞. The recovery factor expresses the gain in temperature of the fluid due to being brought to rest; if this process occurs adiabatically and isentropically, the recovery factor is 1 in Equation 2-2 [4]. Kays and Crawford note the recovery factor is usually approximated at $Pr^{1/3}$ for turbulent boundary layers [5].

$$\frac{T_{recovery}}{T} = RF\left[1 + \frac{\gamma - 1}{2}(Ma)^2)\right] \qquad \text{Equation 2-2}$$

It is more useful to express film cooling results as a non-dimensionalized temperature called film effectiveness or adiabatic effectiveness (η) as given by Equation 2-3 [1,2].

$$\eta = (T_\infty - T_{aw})/(T_\infty - T_c) \qquad \text{Equation 2-3}$$

Thus, η is a measure of how well the film protects the wall. The closer the value is the unity, the better the cooling scheme. Since modern turbine engines use a combination of internal cooling and film cooling, adiabatic effectiveness is often studied to isolate the effects of the film cooling [1]. However, blades are made from metals which are highly conductive, which means they are never adiabatic in actual operation. Furthermore, the high conductivity of the blade means that backside cooling has a substantial effect on the surface temperature, thus the effects of the internal cooling scheme should not be ignored as noted by Davidson *et al.* [6].

To account for the effect of the internal cooling the overall effectiveness (ϕ) is utilized and is given by Equation 2-4.

$$\phi = (T_\infty - T_s)/(T_\infty - T_c) \qquad \text{Equation 2-4}$$

T_c is the internal channel coolant temperature at the film cooling holes and represents the lowest achievable surface temperature. T_s is the actual surface temperature of the blade at a given condition. The biggest advantage of overall effectiveness over adiabatic effectiveness is the T_s can be measured directly while T_{aw} typically needs to extrapolated by plotting the wall temperature vs heat flux (q'') at multiple points as shown by Dittmar *et al.* [2]. For film cooling studies done at engine temperatures, the use of highly conductive metal surfaces is required for survivability reasons making the estimation of the adiabatic wall temperature even more difficult than it is for low temperature where insulative foams can be used for the models.

The effectiveness of the coolant is affected by the convective heat transfer coefficients of the internal channels and the mainstream flow over the blade. The impact of the internal heat transfer impacts the surface temperature through the plate based on its

conductivity and thickness, thus the Biot number, shown in Equation 2-5, is an important parameter to match between the laboratory and the engine. *h* is the convective heat transfer coefficient, *t* is the thickness of the blade wall, and *k* is the conductivity of the blade material. For turbine blades and vanes, the Biot number is typically between 0.1 and 1.5 [2].

$$Bi = \frac{ht}{k} \qquad \text{Equation 2-5}$$

T_{aw} can be obtained directly by constructing the test plate out of near-perfect insulators and correcting for the small amount of conduction the material still provides. Typically the test plate will be constructed from a foam or plastic which makes them suitable for low temperature studies where the freestream temperature is less than 500 K[2, 6, 7, 8]. However, these materials cannot survive at the high temperatures found in actual engines. For experiments conducted at representative engine temperatures, thermally resistive materials must be used. Ceramics could be used and provide approximate adiabatic conditions similar to the low thermal conductivity properties of the foams, but their brittle nature makes them impractical. Therefore, high temperature metals such as stainless steels and nickel superalloys as typically found in actual engines would be a more practical material choice for high temperature test plates. Another drawback of using ceramics is their low thermal conductivity has a large impact on the Biot number and could easily prevent the Biot number from matching actual engine values. This difference would need to be accounted for in the analysis.

Both ϕ and η are dependent on a large number of variables, but extensive research has identified the largest contributors. Bogard and Thole, Eberly and Thole, and Greiner

et al. have recognized density ratio (*DR)*, defined by Equation 2-6, as one of the primary drivers of η [1, 7, 9].

$$DR = \rho_c/\rho_\infty \qquad \text{Equation 2-6}$$

ρ_c is the density of the coolant, and ρ_∞ Typical engines conditions have a *DR* between 1.8 and 2 [1].

Eberly and Thole [7] specifically examined the effect of *DR* on η. Using cylindrical holes with a 6.7D spacing and a 30 degree injection angle, they studied the flow dynamics and effectiveness of two different density ratios; 1.2 and 1.6. Thermal measurements showed higher η values for the higher *DR* at all blowing ratios. The difference between the effectiveness values at high and low *DR* increased with blowing ratio. Centerline effectiveness values can be up to 40 percent higher for *DR* = 1.6 versus the *DR* = 1.2 case [7]. The cause of this impact of density ratio will be more apparent in the following paragraphs.

Velocity ratio (*VR*), mass flux ratio or blowing ratio (*M*), and momentum flux ratio (*I*) have also been identified as major parameters of interest in film cooling research. Their definitions are given by Equation 2-7, Equation 2-8, and Equation 2-9 respectfully.

$$VR = U_c/U_\infty \qquad \text{Equation 2-7}$$

$$M = \frac{\rho_c U_c}{\rho_\infty U_\infty} = DR \times VR \qquad \text{Equation 2-8}$$

$$I = \frac{\rho_c U_c^2}{\rho_\infty U_\infty^2} = DR \times VR^2 \qquad \text{Equation 2-9}$$

U_c is the velocity of the coolant, and U_∞ is the freestream velocity. These parameters each quantify a different aspect of the coolant interaction with the freestream. *VR* scales the

shear layer development, while *M* scales the thermal transport of the film, and *I* scales the jet dynamics, specifically affecting whether the jet will separate or remain attached [1]. Equation 2-7, Equation 2-8, and Equation 2-9 show why *DR* is such an important parameter. If *DR* is matched to the engine condition, than matching any one of *VR*, *M*, or *I* matches the other two by definition. If *DR* is not matched, the experimenter must choose whether to match *M* or *I*. As these parameters scale the results of different phenomena of the film, the results will be affected by not matching both parameters.

Eberly and Thole also performed a PIV analysis of the flow around the coolant holes. The data indicate the coolant jet remains well attached for both *DR* at an $M = 0.6$. At a unity blowing ratio there is a slight detachment of the jet near the hole for the lower *DR*. At a blowing ratio of 2, the jet is completely separated from the wall for both *DR*. Additionally, PIV data shows velocities at the hole significantly higher than the freestream indicating the presence of counter-rotating vortex pairs (CRVPs). The CRVPs are much stronger for the lower *DR*. This mixing effect was also seen when examining the turbulence intensity levels with the lower *DR* showing significantly more turbulence levels near the hole than the higher *DR* case for the high blowing ratio. Time resolved flow field plots of low *DR* in the near hole region showed a number of shear layer vortices. The main factor leading to the formations of both the CRVPs and the shear layer vortices is *I* [7]. Thus, a higher *DR* allows for higher *M*, while keeping *I* low which keeps the jet attached and reduces the strength of CRVPs and shear layer vortices which can entrain hot mainstream air down to the blade surface.

As the ultimate goal of film cooling is to reduce the surface temperature of the airfoil. This can be accomplished by reducing the net heat flux into the blade surface

represented by the Net Heat Flux Reduction (*NHFR*) is sometimes used. *NHFR* is simply the reduction in heat flux to the surface with film cooling versus without film cooling and is via Equation 2-10 [10].

$$NHFR = 1 - \frac{q''_f}{q''_0} = 1 - \frac{h_f}{h_0}\left(1 - \frac{\eta}{\phi}\right) \qquad \text{Equation 2-10}$$

In this equation, q''_f is the heat flux with film cooling, and q''_0 is the heat flux without film cooling. Since most studies are conducted analyzing η without a method to acquire ϕ, ϕ is assumed to be constant. The higher *NHFR* is, the more effective the film cooling scheme is. Additionally, some algebraic manipulation allows it to be expressed in terms of the adiabatic effectiveness, overall effectiveness, and augmentation of the convective heat transfer coefficient ($\frac{h_f}{h_0}$), or the ratio of *h* with film cooling over *h* without film cooling. In this manner it is apparent that NHFR can be maximized by reducing h_f or by increasing η. Since typically h_f is actually increased due to the injection process of adding coolant, it is typically desirous to generate highly effective cooling schemes. *NHFR* is a method of non-dimensionalizing the heat flux for more general applications. It would typically have values between 0 and 1. Negative values are possible if the film cooling increases the heat flux to the plate.

Rutledge *et al.* [11] recognized that heat flux, or net heat flux reduction was not the most important parameter when considering film cooling's effectiveness at increasing a blade or vane's survivability. In fact, the increase in the convective heat transfer coefficient from film cooling may outweigh the reduction in surface temperature such that the heat flux increases. The reduction in surface temperature is the goal of film

cooling, not the reduction in heat flux. With this in mind, Rutledge *et al.* proposed using the net increase in overall effectiveness, $\Delta\phi$, given in Equation 2-11.

$$\Delta\phi = \phi - \phi_0 = \frac{T_{s0} - T_s}{T_\infty - T_c} \qquad \text{Equation 2-11}$$

ϕ is the overall effectiveness with film cooling. ϕ_0 is the overall effectiveness without film cooling, but with the equivalent internal cooling. Likewise, T_{s0} and T_s are the surface temperatures without and with film cooling respectively. T_∞ is the freestream temperature. T_c is the coolant temperature which would be held constant for both cases. Thus, $\Delta\phi$ provides a non-dimensional reduction in the surface temperature due to film cooling regardless of the change in heat flux or heat transfer coefficient [11]. While this relationship was developed to compare no film cooling to cases with film, similar comparisons could be made between different cooling schemes, different coolants, different freestream Mach numbers, or reactive versus nonreactive conditions.

2.2 Hole Geometry

The physical design of the film cooling scheme plays a critical role in its performance. The size, shape, orientation, location, and spacing of the holes all affect the resulting film effectiveness. Bogard and Thole note film holes are typically oriented 25 to 35 degrees from the surface in the streamwise direction. The low angle to the surface is to help prevent the jet from separating which significantly reduces film effectiveness. Additionally, holes on the leading edge of a blade are typically oriented normal to the surface of the blade in the streamwise direction, but are slanted in the radial direction [1]. This angle along the radial direction of the blade is referred to as a compound angle, and the holes on the leading edge are called showerhead holes due to their similar appearance

to a bathroom showerhead. A depiction of showerhead holes can be seen in Figure 2-1 [12].

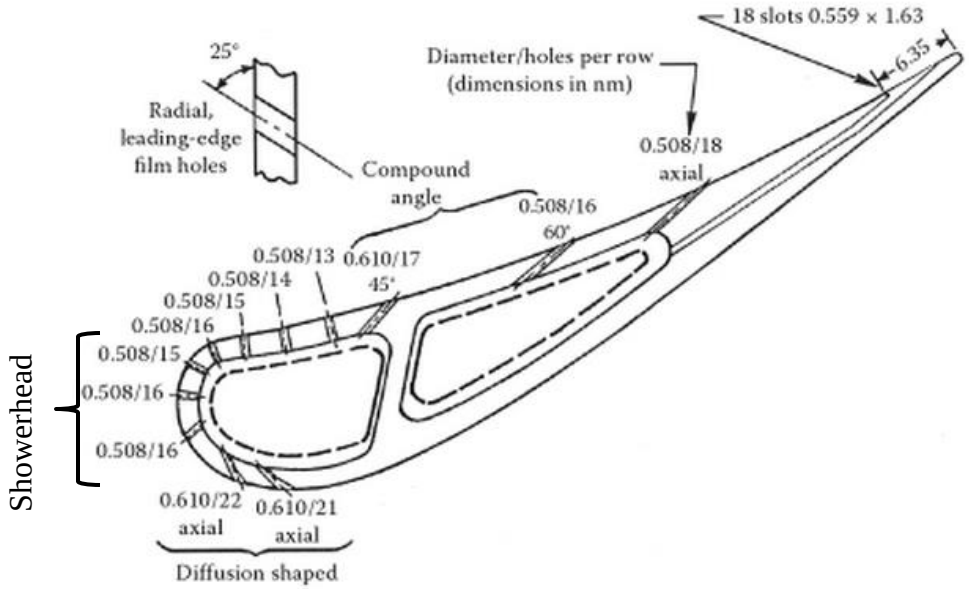

Figure 2-1: Depiction of film cooling hole arrangement (image from Han *et al.* [12])

Simple film cooling holes have a cylindrical cross-section and have no additional contouring. Cylindrical holes are by far the most common hole type used due to their relatively low cost of manufacturing. Long continuous slots are commonly studied to provide baseline ideal cases for film effectiveness. Slots can lay down an even sheet of coolant over the span of the surface at low I which help keep the coolant attached. However, slots severely degrade the structural integrity of the blades due to the large amount of material removed, and the lack of support for the upper surface [1, 14]. In order to gain some of the benefits of slots, namely a more even distribution of coolant, without degrading the structural integrity of the blade fan-shaped holes have been studied. Fan-shaped holes are usually cylindrical holes which have had their outlets flared

by adding a laid-back angle and/or by widening the hole in the spanwise direction. Polanka *et al.* note this flaring of the hole reduces the momentum flux ratio at the exit and helps the jet remain attached to the wall [15]. Laid-back and flare angles in the 10 to 15 degree range are common in the literature [1].

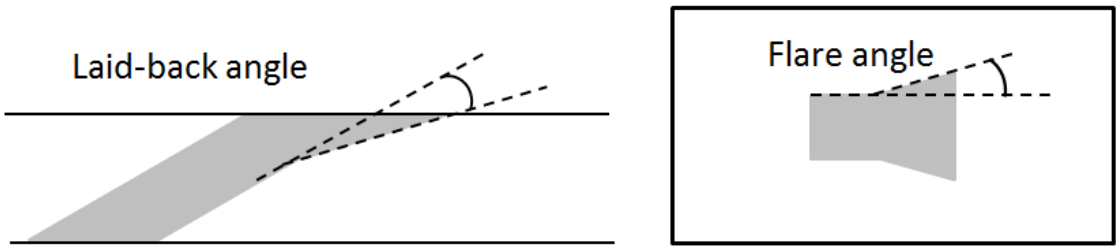

Figure 2-2: Cartoon of a fan-shaped hole.

While fan-shaped holes were an improvement over conventional cylindrical holes, they still failed to match the effectiveness of the slot. Bunker [14] began to study slots fed by cylindrical holes, or trenches. Trenches are short slots which do not penetrate all the way through the blade wall. The idea was coolant from the cylindrical holes could spread out in the spanwise direction before it is injected into the mainstream flow. This has the effect of providing nearly the same even sheet seen from slots, but without the structural disadvantage. Also the total coolant flow can be less than a slot since the trench is being supplied by cylindrical holes [14]. Figure 2-3 shows a perspective cross section view of a simple trench.

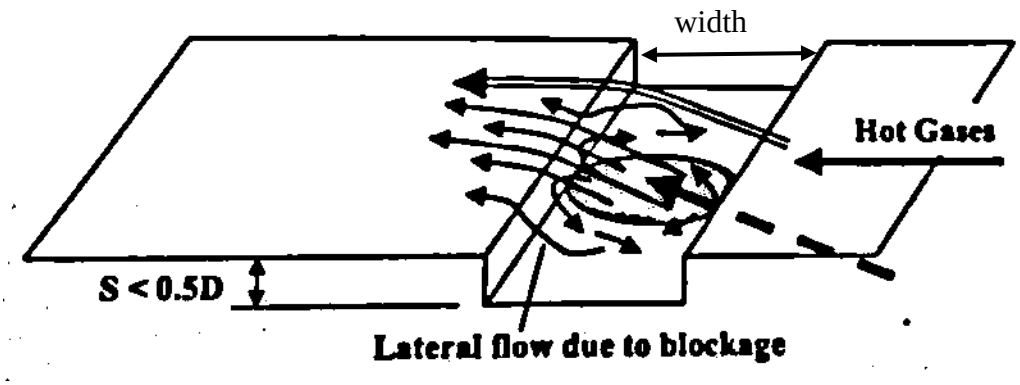

Figure 2-3: Drawing of a shallow trench configuration and the coolant flow patterns (image from Bunker [14]).

Bunker conducted a study with several different trench configurations. Each trench was supplied coolant from 12 cylindrical holes. Two deep trench configurations were tested both with a depth of 3 hole diameters, one with a width of 1.13 diameters, and the other with a width of 1.5 diameters. Additionally, he considered holes with a 60 degree radial angle, and holes with a 30 degree axial angle. At low *M*, the trenches with the axial holes resulted in twice the film effectiveness over the trenches with radial holes. However, the effectiveness of the trenches with radial holes was found to scale well with *M*. This is contrary to radial holes alone [16] which have little dependence on *M*. Furthermore, the narrower slot produced higher η values over the wide slot. However, Bunker notes such deep trenches have little practical use for turbines because of the amount of material removed.

Therefore, Bunker examined the performance of a shallow trench with a depth of only 0.5 diameters supplied by 30 degree axial holes with the width set equal to the surface profile of the holes, or 2 diameters. The shallow trenches produced an increase in η of 50 to 75 percent at downstream distances within 40 diameters of the trench over the same axial cylindrical holes without the trench. The even cooling produced is attributed

to the partial blockage of the flow path of the hole by the trench wall forcing the coolant to distribute within the trench before injecting into the freestream. Finally, the shallow nature of the trenches would allow for them to be easily formed during the application of thermal protective coating [14].

2.3 Hole Spacing and Full Coverage Film Cooling

The spacing, or pitch (*P*), of the holes affect whether the coolant from the holes will act independently or not. The row pitch is the distance between rows of holes. A hole pitch is the distance between holes in a row. The hole pitch is typically between three and eight hole diameters (*D*) [1]. Multiple rows of holes can also be used to build up a more substantial layer of coolant. Row spacing also varies widely, but full coverage film cooling schemes typically have row pitches between 3 and 8 [1]. Full coverage film cooling is commonly used in combustor liners, turbine end walls and other places in the engine which may encounter extreme thermal loads.

Harrington *et al.* [8] conducted a study of full-coverage film development using normal holes with a length to diameter ratio of one. Their test plate was constructed from polyurethane with 6 mm diameters with a row pitch and spacing pitch of 7.14. In order to obtain a *DR* of 1.7, the coolant air was cooled to -90 C. The team examined blowing ratios of 0.25 and 0.65. The first test utilized only a single row of coolant holes, which provided a baseline to compare full coverage results with superposition estimates based on the equation presented by Sellers [17] given in Equation 2-12. Superposition is an estimation method by which results for a single row are summed to provide an approximation for the impact of multiple rows of holes.

$$\eta = \sum_{i=1}^{N} \eta_i \prod_{j=0}^{i-1} (1 - \eta_j) \; where \; \eta_0 = 0 \qquad \text{Equation 2-12}$$

Harrington *et al.* found a fully developed effectiveness profile by the fourth row for the lower blowing ratio, and by the eighth row for the higher blowing ratio. Up to those respective row counts, the superposition predictions were consistent with the experimental data. However, superposition would predict continually increasing adiabatic effectiveness after the coverage is fully developed making it ineffective for large row counts. Harrington *et al.* state the cause is the interaction of the upstream coolant jet with downstream jets which superposition does not consider. As the higher blowing ratio gave higher η values for the fully developed film coverage, the researchers also examined a case with a unity blowing ratio. However, the coverage was still fully developed by the eighth row indicating the additional coolant was not beneficial. The film effectiveness topped at 0.35 for the fully developed coolant [8].

Andrews [18] conducted a study of full coverage cooling as is typically found in combustor liners. He examined the effects of having a backside air duct versus a plenum air supply, and the effects of hole pitch. Andrews' test plates had a constant normal hole spacing of 10.16 mm, but varied the hole diameter between 0.937 mm and 2.235 mm. The tightest hole spacing consistently produced the highest overall effectiveness values for all blowing ratios due to the even distribution of coolant over the plate. As the blowing ratio approached 3, the overall effectiveness climbed to over 0.80. Furthermore, the back side air duct produced highest effectiveness than the plenum for the same mass flow and hole size. This benefit declined moving towards the trailing edge of the plate due to the internal flow reducing to zero flow at that location. The largest difference in

overall effectiveness of 0.2 between the duct and plenum was for the largest hole spacing close to the leading edge of the plate where the internal flow rate is highest. With a mass flux rate of 0.4 kg/(m^{2}s), which corresponds to a M of approximately 1, the highest effectiveness of 0.73 was achieved using a hole spacing of 4.6 D at 100 mm downstream from the leading edge [18].

2.4 Scaling Factors

Due to the immense cost and complexity of performing film cooling studies at engine conditions with high temperatures and pressures, most studies are performed at near standard atmospheric temperatures and pressures. However, fluid properties are not constant between engine and rig temperatures. The properties also do not vary linearly with temperature, which can cause scaling issues between room temperature experiments, and actual engine conditions. Therefore, film effectiveness results obtained from these low temperatures experiments will not match engine conditions. The question is, how close do they match and what parameters are most important to obtain acceptable results?

Greiner *et al.* [9] performed a CFD study using Fluent® to determine which parameters needed to be matched in order to obtain the same results from a room temperature experiment as a high temperature baseline case. For the baseline case, T_{inf} = 1829 K, T_c = 625 K, U_∞ = 49.4 m/s, U_c = 16 m/s, and M = 0.946. All the cases were performed for a fan-shaped hole with 10 degrees of layback and flare. Parameters of particular interest were Prandtl (*Pr*), Equation 2-13, and Reynolds (*Re*), Equation 2-14, numbers of both the freestream and coolant. However, real fluid properties prohibit these parameters from being matched between the low temperature and the high temperature test [9].

$$\mathrm{Pr} = \frac{C_p \mu}{k}$$ Equation 2-13

$$Re = \frac{\rho U L}{\mu}$$ Equation 2-14

The first case matched *M* and freestream Reynolds number (Re_∞) as is commonly done in many studies. The *DR* was set to 1.18. Overall, η matched the baseline case well, especially far downstream from the hole. It under predicted η close to the hole and counter-rotating vortex pairs (CRVPs) were seen. This is indicative of increased jet separation over the baseline case. The separation was a result of an increased *I* from decreased *DR* while still matching *M*. Case 2 was identical to Case 1, except for coolant Reynolds number (Re_c) was matched instead Re_∞. Results were similar to Case 1, with even more pronounced separation near the hole leading to a severe under-prediction of near hole η [9].

Case 3 matched *DR* and *M*. The increased momentum of both the freestream and coolant flows produced much stronger CRVPs than either of the first two cases which increased mixing near the hole reducing η. However, the jet remained well attached far downstream leading to an overprediction of η. Case 4 matched all parametric ratios by creating artificial fluids in FLUENT. Results were similar to case 3 instead of the baseline case. Case 5 built on Case 4, but also matched Re_∞ and Re_c. This forced the viscosity to not match and consequently the *Pr*'s were around 2.3 which is more representative of liquids rather than 0.7 of most gases. Case 5 vastly overpredicted η showing the importance of matching absolute values of *Pr*. Case 6 matched all parametric ratios, and also matched *Re* values with the baseline case. This produced excellent results

by matching the baseline case well. However, Case 6 is not usable in actual laboratory experiments because of its use of imaginary fluids [9].

Greiner *et al.* performed two more cases which could be performed in a laboratory experiment. Case 7 matched M, DR, and Re_∞. Case 8 matched M, DR, and Re_c. Case 7 overpredicted the centerline η while case 8 underpredicted centerline η. Both cases produced reasonable agreement with the baseline case on their own, but the average of the two cases produced almost an exact match with the baseline case. Greiner *et al.* note the cost of performing both experiments may not be justified by the small increase in the accuracy of the results. Greiner *et al.* continued the study by looking at the accuracy of Cases 7 and 8 for a lower M and a higher M. Case 9 repeated the baseline case, but with $M = 0.5$ instead of being close to unity. Cases 10 and 11 matched the same parameters as Cases 8 and 7 respectively. Since the jet is still well attached, results were similar to those seen when $M = 1$. Case 12 repeated the baseline case with $M = 3$. Case 13 matched Re_∞ while Case 14 matched Re_c. Due to jet separation, Case 13 resulted in a large underprediction of η near the hole while Case 14 produced a large overprediction of η. However, the over and under prediction were of similar magnitude allowing the average of the two cases to result in almost a perfect match to the Case 12. Greiner *et al.* note that for separated jets significant benefits can be achieved by performing both cases instead of jet matching Re_c which is sufficient if the jet remains well attached [9].

Rutledge and Polanka [19] performed a CFD study on a representative showerhead hole located on a quarter cylinder leading edge. The hole had a compound angle with a 90 degree streamwise component and 70 degree spanwise component. The hole was 21.5 degrees up from the stagnation line on a quarter circle followed by a flat surface. Like

Greiner *et al.*, their goal was to find important non-dimensional parameters which need to be matched between a high temperature baseline case and low temperature laboratory experiment. Of particular interest was the heat capacity ratio (*HCR*) described in Equation 2-15.

$$HCR = \frac{\rho_c U_c C_{p,c}}{\rho_{inf} U_{inf} C_{p,\infty}} \qquad \text{Equation 2-15}$$

$C_{p,c}$ and $C_{p,\infty}$ are the specific heat values of the coolant and freestream respectively. Rutledge and Polanka found that *HCR* has a large impact on *NHFR*. At engine conditions, *HCR* is typically around 0.8 while at room temperature experiments it is near unity. Using the results from a unity *HCR* laboratory experiment will overpredict *NHFR* by up to 8.6 percent [19].

2.5 Reactive Film Cooling

As turbine engines rely on the combustion of hydrocarbon fuels, certain elements of the engine will be exposed to the flames created from the combustion of these hydrocarbons. Protecting these components is important for the longevity and integrity of the parts and produces unique challenges to designers. The combustor is the most obvious location for combustion to be occurring within close proximately to metal surfaces of the engine's interior. In certain high-performance engines, an afterburner may be added for additional power which exposes aft sections and the nozzle of the engine to a high temperature flame. However, it is also possible for combustion to occur within the early turbine stages as the result of fuel rich streaks or high engine equivalence ratios [23]. Furthermore, researchers have been examining advanced combustor designs which significantly shorten the combustor section of the engine [21]. All of these reasons

demonstrate the need for an understanding of film cooling techniques in a reactive environment.

2.5.1 Motivation for Reactive Film Studies

Combustors by nature, are a highly reactive environment. Still, the combustion must occur within a containment vessel capable of handling the high temperatures and pressures. Cooling the components in a combustor has been an area of research since the early days of the jet engine. Combustors usually utilize some form of full coverage film cooling similar to the pattern used by Harrington *et al.* [8] described above. A modern combustor uses liners which are cooled by a combination of impingement and full coverage film cooling [20].

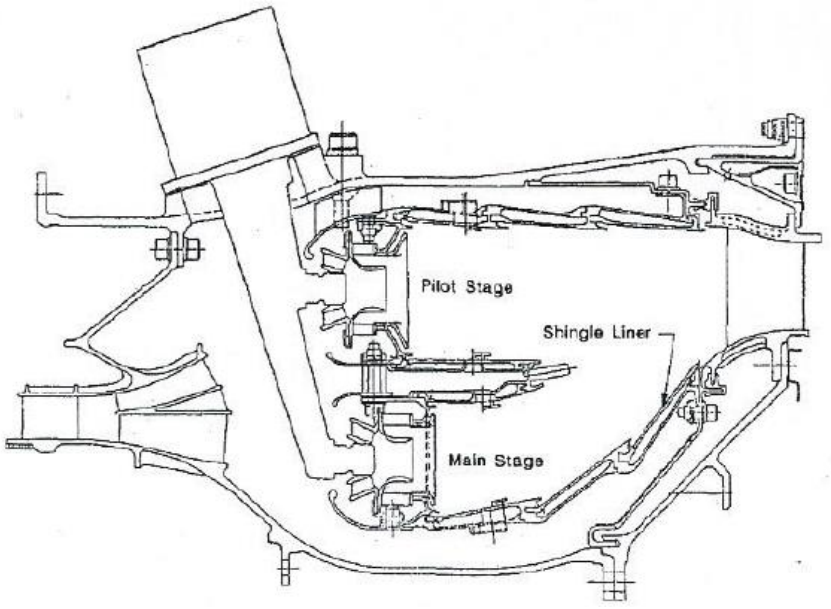

Figure 2-4: Cross section of an E^3 combustor (image from Bahr [20]).

Combustor liner cooling is typically well approximated in flat plate studies because the walls of the combustor liner do not have the extreme curvatures found on turbine blades. However, research has been progressing on new generation combustors called

Ultra-Compact Combustors (UCC). As noted by Johnson and Polanka [21], the goal of a UCC is to reduce engine weight by shortening the length of the combustor. Johnson and Polanka performed a CFD study on the cooling required in a UCC where the combustion occurred in a circumferential cavity. A strong axial core flow passes inside the circumferential cavity over a series of hybrid vanes. These vanes act as both the compressor exit vanes, and the nozzle guide vanes for the turbine. The vanes are exposed to high temperature combustor flow. Johnson and Polanka concluded the suction side will need cooling and that the gas flowing over the blades will be fuel rich making reactions likely Figure 2-5 shows the predicted temperature profile on a portion of a hybrid vane. The combustion occurs in the cavity on the top of the front portion of the vane. Thus, flame and combustible species will be in imminent contact with the blade surface [21].

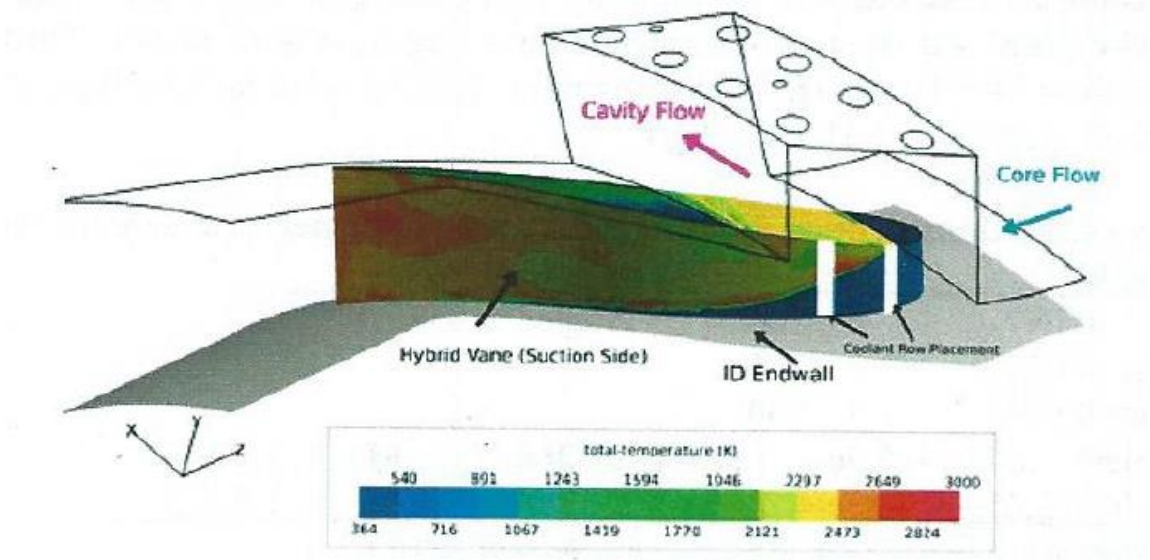

Figure 2-5: Predicted temperature profile of UCC hybrid vane [21]

2.5.2 Reactive Turbine Cooling

As engine manufacturers seek to make more efficient engines, they will naturally seek to increase the turbine inlet temperature. Increasing this temperature means running the combustor closer to a stoichiometric mixture. Lukachko *et al.* [22] note as the combustor temperature and pressure increase, combined with the increasing fuel fraction, the concentrations of CO, OH, H, and O at equilibrium will increase. These species can contain up to 10 percent of the fuel's energy which could react when they encounter oxygen rich film cooling air. They sought to quantify the heat release that could be expected in the turbine from these reactive species [22]

Lukachko *et al.* note the Damkohler number (*Da*) is the characteristic parameter for the heat release. *Da* is a ratio of the flow time to the chemical time as shown in Equation 2-16.

$$Da = \frac{\tau_{flow}}{\tau_{chem}} = \frac{\frac{L}{u_\infty}}{\tau_{chem}} \qquad \text{Equation 2-16}$$

τ_{flow} is the characteristic flow time and τ_{chem} is the characteristic reaction time. The flow time can be thought of as the time required for the flow traveling at velocity u_∞ to pass over a surface of length *L*. Lukachko *et al.* used the total temperature change (ΔT_t) as a measure of the progression of the reaction. Ignition occurs at a ΔT_t of 5 percent, with the reaction completing at a ΔT_t of 95 percent. The time needed to progress from ignition to reaction complete is the chemical time. The reaction times were calculated using the fastest possible reaction times with the hotter mainstream temperature. The flow time was determined by the chord length of the blade divided by the flow velocity. If the *Da* was much less than unity, the reaction would not have time to progress while it was in contact

with the blade. Thus, the heat load on the blade from the reaction was minimal. Conversely, if the *Da* was larger than unity, the reaction would reach completion over the blade causing large amounts of local heating. Finally, if the *Da* was near unity, the blade would experience fairly even heating over its length [22].

Kirk *et al.* [23] continued the work of Lukachko *et al.* [22] by performing shock tube experiments to generate quasi-steady state flows with a variety of chemistries. As their test rig utilized a flat test plate, the flow time was defined as the time required for the flow to transverse 10 *D*. The freestream flow used an Argon/Ethylene mixture. Argon was chosen for its inertness and high specific heat ratio allowing the exact heat release potential of the mainstream to be controlled. Furthermore, Ethylene has a short ignition time. The freestream Mach was fixed at 0.3. Finally, the test plate itself has two sets of cooling holes each fed with an independent coolant supply allowing for both reactive and non-reactive film cooling cases to be tested simultaneously. One set used nitrogen and the other used air [23].

To compare the freestream fuel levels, Kirk *et al.* defined a non-dimensional fuel enthalpy (*H**) given by Equation 2-17.

$$H^* = \frac{T_{ad} - T_{t,inf}}{T_{t,inf}} \qquad \text{Equation 2-17}$$

T_{ad} is the adiabatic flame temperature. *M* was varied between 0.5 and 2 for the tests. *H** was varied between 0.005 and 0.8 determined by the amount of ethylene mixed with the freestream Argon. The data were considered in three ranges of *H**: low below 0.03,

medium between 0.06 and 0.24, and high between 0.18 and 0.8. Freestream temperatures were varied between 1,000 K and 2,800 K. The *Da* was varied between 0 and 30 [23].

A baseline test with an un-cooled side and a non-reactive cooled side with *M* set to unity showed a *NHFR* of 10 to 35 percent on the cooled side. Kirk *et al.* found high *Da* and high *H** increased the heat flux augmentation about 30 percent. The level of increase in augmentation decreased with lower *Da* and *H**. Furthermore, low *H** prevents augmentation from exceeding 10 percent for any *Da*, and a *Da* less than unity restricts augmentation to less than 5 percent even at high *H**. A comparison of attached jets with a *M* of 0.5, and detached jets with a *M* of 2 showed significantly more augmentation for the attached jet when conditions favor high augmentation. Kirk *et al.* concluded that although a non-reactive cooling scheme could produce values for η between 0.15 and 0.3, the same cooling configuration could result in η values between -0.1 and -0.4. Thus, a reactive film could actually heat the wall it is attempting to cool and no film cooling at all would produce a lower heat load on the wall [23].

Polanka *et al.* [15] built on the work of Kirk *et al.* by conducting CFD and experimental studies of various hole geometries in a fuel rich environment. They examined the performance of cylindrical normal holes, angled cylindrical holes, fan-shaped holes, and an angled slot. For the CFD study, they used Chemkin, a combustion chemical analyzer software, to determine the combustion products from a propane-air Well-Stirred Reactor (WSR) running at equivalence ratios of 0.95 and 1.5. The blowing ratio for the CFD study was set to unity. For the experimental studies, they used a high temperature flat plate test rig capable of using either air or nitrogen as a cooling to produce both reactive, and non-reactive cases. The test rig's mainstream air was supplied

by the combustion products of an upstream propane-air WSR running at equivalence ratios from 0.6 to 1.7. The coolant blowing ratio was varied between 0.5 and 2. Their experimental rig can be seen in Figure 2-6. The cooling hole insert could be exchanged between tests to allow different cooling configuration to be examined [15].

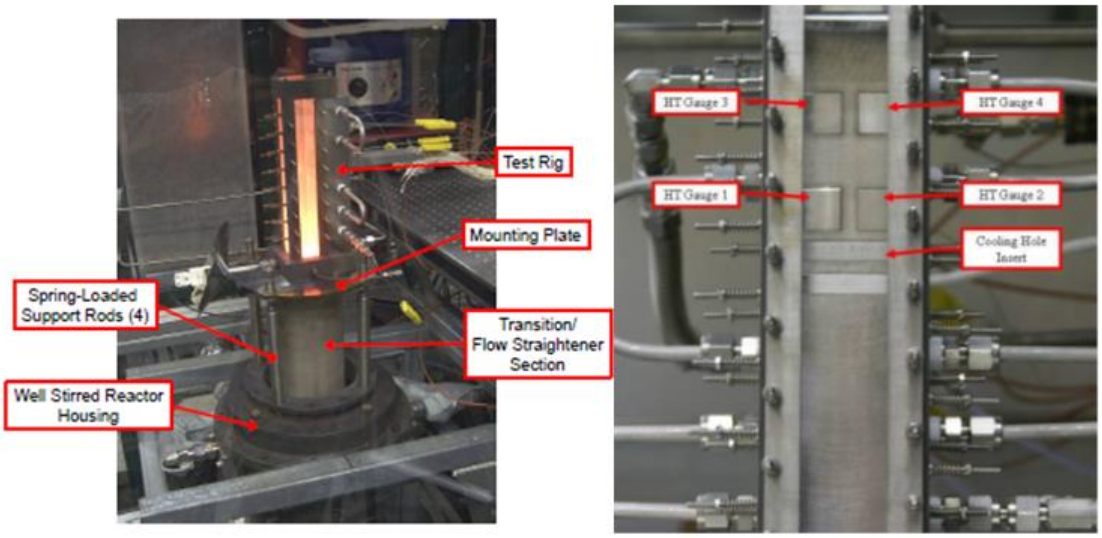

Figure 2-6: Experimental rig used by Polanka *et al.* [15] and Bohan *et al.* [24].

Polanka *et al.* found that for equivalence ratios below unity, combustion does not occur within the film. In these cases, the CFD showed a detached jet for the normal hole, and attached jets for the angled cylindrical and fan-shaped holes. Additionally, no reaction occurred in the CFD model at the higher fuel fraction when nitrogen was used as a coolant. This was also seen in the experimental studies and is as expected since the reaction can only occur in the presence of oxygen rich coolant. However, when air was used as a coolant, the CFD code predicted a short region of effective cooling followed by a dramatic increase in film temperature and a negative η as low as -0.26 for the fan-shaped hole which produced the worst case. These results were confirmed in the

experimental study with a visible flame just downstream of the coolant holes. The heat flux gauge downstream of the holes recorded the largest increase in heat flux for the fan-shaped holes, with a slightly lower increase for the cylindrical angled holes. An analysis of η also resulted in negative values for an air coolant with the fan-shaped holes having the lowest effectiveness values. Effectiveness values for the nitrogen coolant closely matched other published literature for similar hole geometries and blowing ratios. Overall, Polanka *et al.* found that fan-shaped holes are detrimental in the reactive case for the same reason they are beneficial in the non-reactive case: the coolant jet remains well attached to the wall. In the reactive case this also means the flame is well attached to the wall and the driving temperature is much higher than freestream and is also much closer to the wall [15].

Given the results of Kirk *et al.* and Polanka *et al.*, other researchers sought to find ways to effectively cool the wall with a reactive film. Bohan *et al.* [24] sought to do this using a sacrificial row of film to consume the combustible species in the freestream preventing combustion from occurring farther down the surface. Bohan *et al.* used a WSR running at an equivalence ratios of 0.6 to 1.5 to provide hot, fuel-rich freestream air to the same test rig used by Polanka et al [15] seen in Figure 2-6. Bohan *et al.* looked at placing three different hole configurations upstream of fan-shaped holes. Fan-shaped holes were chosen for the downstream protected holes because previous research showed fan-shaped holes resulted in the highest augmentation with a reactive film [15]. The team tested a 30 degree angled slot, fan-shaped holes, two staggered rows of normal holes, as well as a blank plate upstream for a baseline comparison [24].

Bohan *et al.* found no increase in heat flux for equivalence ratios below stoichiometric. The blank plate upstream showed an increase in heat flux of up to 17 percent from using air instead nitrogen for the downstream holes with an *M* of 1.5 and an equivalence ratio of 1.3. Furthermore, they found the greater increases in heat flux at high blowing ratios, until the jet begins to separate from the wall when the blowing ratio approaches 2. The normal upstream holes produced no appreciable mitigation of the increase in heat flux. Planar laser-induced fluorescence (PLIF) using OH concentrations showed a large reaction plume just downstream of the normal holes as seen on the left side of Figure 2-7. A second reaction plume is seen just downstream of the fan-shaped holes the goal was to protect showing the normal holes were ineffective at consuming the combustible species near the wall. Conversely, the upstream slot showed good protection of the fan-shaped holes according with an increase in heat flux of less than 5 percent when using air instead of nitrogen as a coolant for a slot blowing ratio between 1 and 3. PLIF showed the reaction zone remained near the wall with a slight shift away from the wall at the injection site of the downstream holes [24].

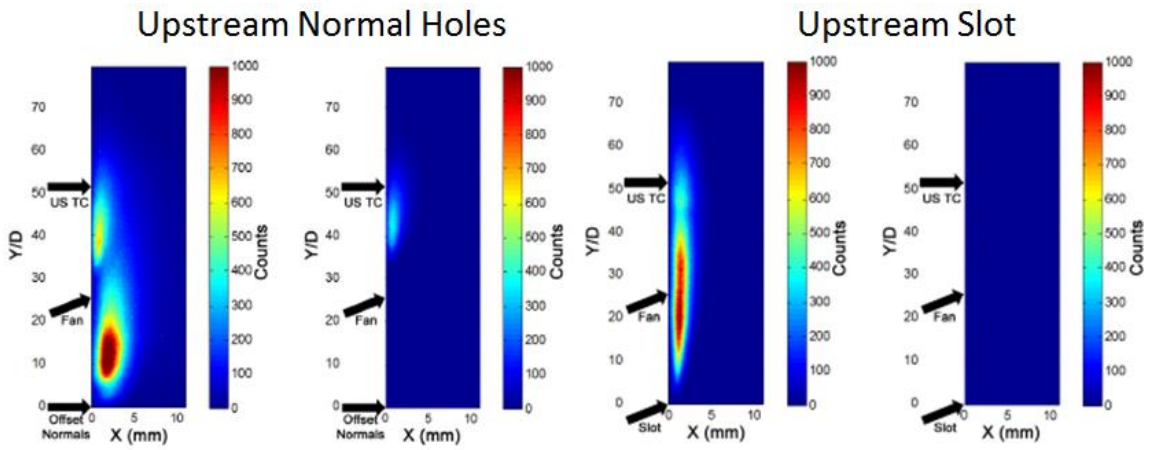

Figure 2-7: PLIF OH concentration measurements for air (left) versus nitrogen (right) upstream coolant [24].

Lynch *et al.* [25] reported a study on wall protection schemes in a high temperature reactive environment. Used similar experimental setup to Bohan *et al.* [24] and Polanka *et al.* [15], to examined several different multiple row cooling schemes, seen in Figure 2-8, and analyzed their performance using *NHFR*. They examined 5 rows of cylindrical holes, 5 rows of slots, 5 rows of trenches supplied by the same holes as the cylindrical holes, and a plate with a backwards facing step (BFS) also containing a total of 5 rows of staggered holes. The mainstream flow was supplied by a propane-air WSR running at an equivalence ratio of 1.3. They varied the blowing ratio from 0.5 to 3. Furthermore, they compared the performance of each cooling scheme between a nitrogen coolant and air. This allowed comparison between non-reactive and reactive cases respectively.

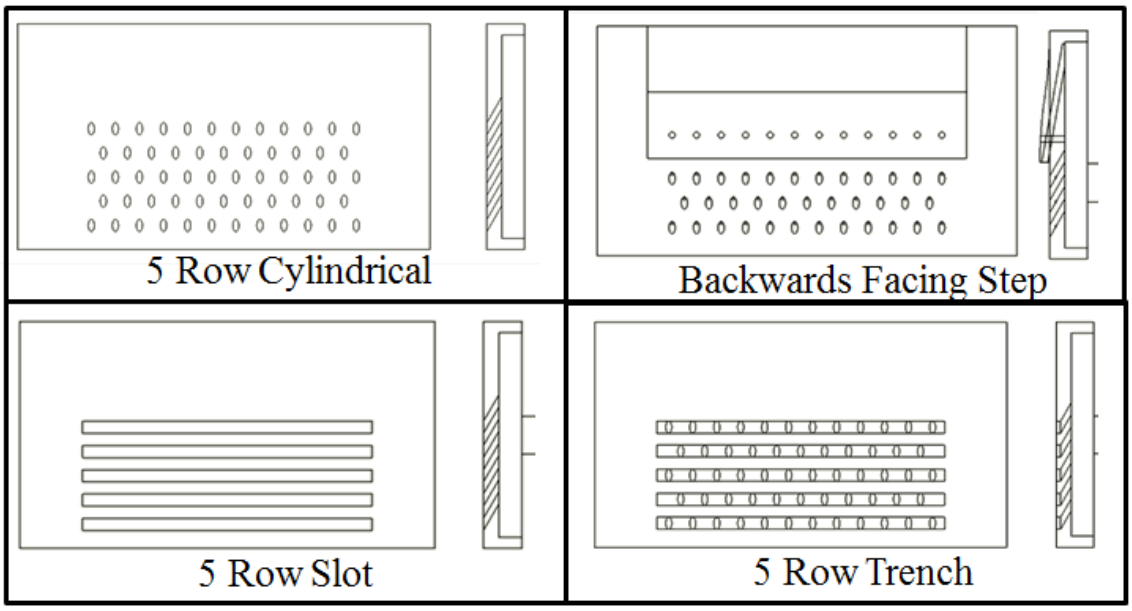

Figure 2-8: Heat mitigation cooling geometries examined by Lynch *et al.* [25].

Overall, Lynch *et al.* found the higher blowing ratios produced higher *NHFR* values. In all cases, the Nitrogen supplied holes outperformed the air supplied holes. As expected based on previous studies, the 5 row slot configuration supplied by Nitrogen provided the highest *NHFR*. Figure 2-9 shows the overall results from Lynch *et al.* As mentioned previously, slot configurations are not practical due to the reduced structural integrity of the blade, but trenches may provide some of the benefits of the trench in terms of performance. Their results appear to confirm that hypothesis of the trench being a beneficial cooling scheme. It is especially noticeable over a blowing ratio of 1.5 as the trenches continue to provide benefit from increased coolant flow whereas the traditional cylindrical holes start to show a decrease in *NHFR* [25].

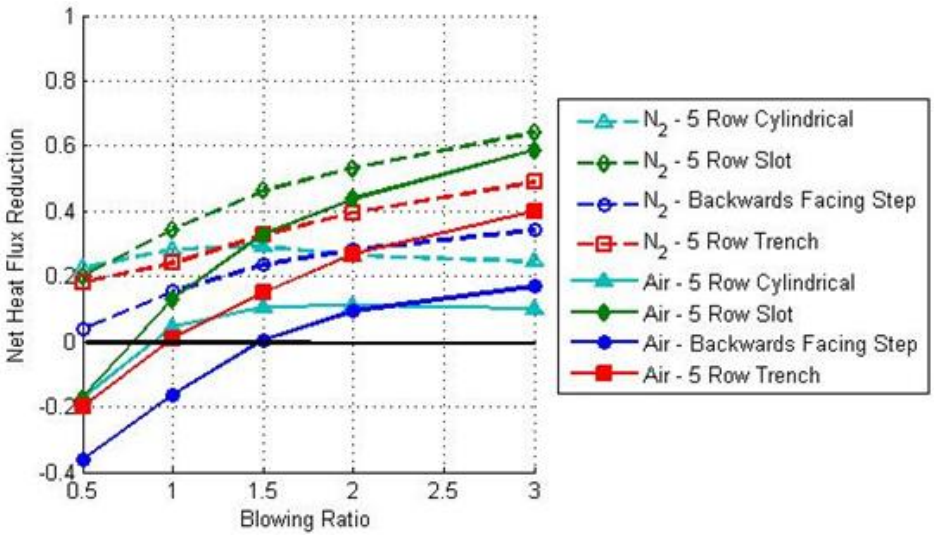

Figure 2-9: *NHFR* vs blowing ratio at x/*D* = 22 (from Lynch *et al.* [25]).

Shewhart [26] examined the surface temperature of the test plates used by Lynch *et al.* [25] using an FLIR SC6700 IR camera. A flame filter was used to block the emissions from any participating media between the test plate and the camera. IR access to the test plate was provided through an optical grade sapphire window. The camera was calibrated by using the known surface temperature of the heat transfer gauge block. The surface temperature data was in agreement with the *NHFR* data. The slot performed the best, followed by the trench, then the BFS, and finally the cylindrical holes [26].

Shewhart was able to demonstrate that it is possible to cool the wall even in a reactive environment by using the correct cooling scheme. Polanka *et al.* had found the preferred fan-shaped holes used in non-reactive cooling were a sub-optimal choice in a reactive environment [15]. No cooling at all providing lower heat flux than cooling in a reactive environment with the fan-shaped holes. At this point, it appears the trench configuration may be a practical scheme moving forward in the search of protecting blades from the flame created by unburnt fuel species. However, all of these reactive

studies presented here have been conducted at a low Mach number over a flat test plate. The effects of curvature, and the flame's dependence on Mach number is not currently well understood [26].

2.6 Mach Number and Curvature Effects

Turbines extract power from the fluid by turning the flow. This turning angle can often be over 90 degrees in the high pressure turbine meaning the blades will have a large amount of curvature in them. The blade is often described as having two sides; a pressure side which has concave curvature, and a suction side with convex curvature. Most film cooling studies are performed over flat plates for simplicity to decrease cost or to reduce the complexity of flow interactions. Schwarz *et al.* [27] notes that for coolant with a *VR* less than unity, the coolant jets will turn move towards convex walls and away from concave walls. The trend is reversed for *VR* greater than unity [27].

Schwarz *et al.* performed a study over a convex surface with 135 degrees of turning. The radius of curvature of the surface was 10.1 cm. The hole diameter was varied in order to study the effects of radius of curvature to hole diameter (*2r/D*). Schwarz *et al.* found the lower the curvature value, the higher the film effectiveness. Furthermore, the lower curvature values can sustain high momentum flux ratios prior to the coolant jet separating. With a *2r/D* of 94, the peak laterally averaged effectiveness of 0.21 was seen with an *I* of 0.5. With a *2r/D* of 61, the peak laterally averaged effectiveness of 0.25 was seen with an *I* of 0.6. Furthermore, higher density ratios allowed for higher blowing ratios which increased the effectiveness by providing more coolant to dilute the near wall temperature. The high density ratios allowed the momentum flux ratios to be kept low to prevent separation [27].

Gritsch *et al.* [28] studied the effects of Mach number on film effectiveness. Gritsch *et al.* used a de Laval nozzle to create test section mainstream Mach numbers up to 1.2. Coolant was supplied by a single 10 mm diameter hole angled at 30 degrees from the surface in the streamwise direction. Three hole configurations were tested; a cylindrical hole, a fan-shaped hole, and a laid-back fan-shaped hole. The test surface was constructed from a low conductivity, high temperature plastic. Surface temperature measurements were made with a combination of thermocouples and an IR camera. Blowing ratios of 0.5, 1.0 and 1.5 were evaluated [28].

Gritsch *et al.* found little difference in film effectiveness from changing the mainstream Mach number from 0.3 to 0.6 with the cylindrical hole. Increasing the Mach number to 1.2 resulted in a large increase in effectiveness. Gritsch *et al.* hypothesize this is due to the jet obstructing the mainstream flow causing several additional shocks to form ultimately resulting in the jet rapidly turning back towards the surface. For the fan-shaped holes, the increase in effectiveness is less pronounced at the supersonic Mach number. However, the fan-shaped holes both provided small increases in effectiveness at a Mach number of 0.6 versus 0.3 [28].

3. Experimental Setup

The work presented in this thesis is an expansion of the work accomplished by Lynch *et al.* [25] and Shewhart [26] whose work culminated a study of reactive film over at flat plate at low mainstream Mach numbers. The main goal of this research is to study overall effectiveness of a non-reactive and reactive film over a plate with surface curvature. With that goal, a new test facility was constructed to enable these parameters to be examined.

This test rig was composed of two primary components; a well-stirred reactor and the film cooling test section. The facility was housed in the Combustion Optimization and Analysis Laser Laboratory (COAL Lab) at AFIT at Wright-Patterson AFB, OH. A schematic of the overall layout of the experimental rig can be seen in Figure 3-1. Shewhart [26] had completed the majority of the design of the well-stirred reactor and the test section for the film cooling rig. The details of the test block assembly still needed to be completed along with the integration of the rig into the laboratory space including the new flow lines and the new controllers for the rig. The following sections outline the details of the hardware built for this investigation and the instrumentation and controls developed and implemented to complete the goals of this thesis.

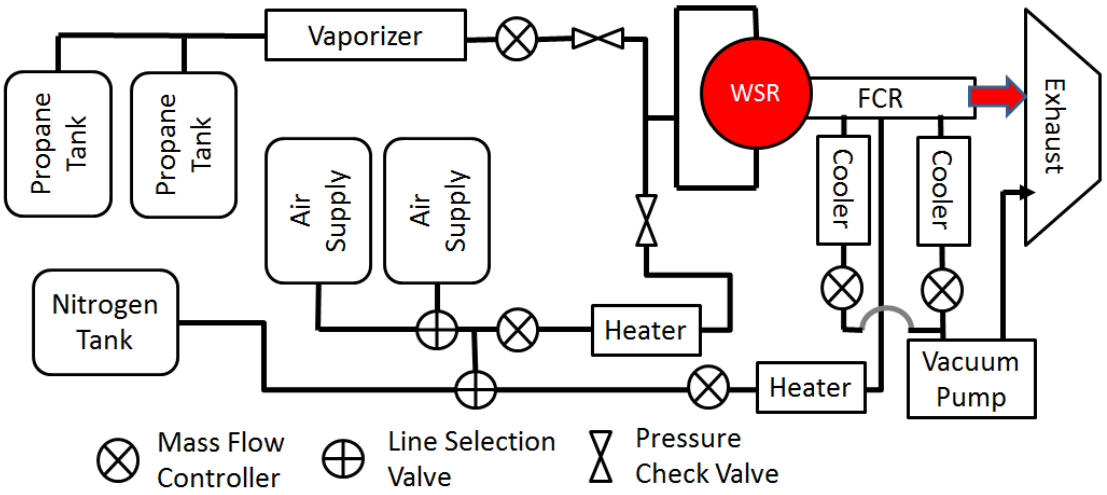

Figure 3-1: Schematic of the flow layout for the experimental setup.

3.1 Well-Stirred Reactor

The Film Cooling Rig (FCR) was provided a controlled mixture of fuel and air from a Well-Stirred Reactor (WSR) based on the design by Nenniger *et al.* [29] and Stouffer *et al.* [30]. The WSR consists of a jet ring inserted between two half toroids as depicted in Figure 3-2, and clamped together between the upper and lower plates on the right side of Figure 3-2. The WSR was operated with a propane/air mixture at a range of equivalence ratios. The combustion products exhausted through a circular exit port in the center of the upper toroid and passed through a flow straightener to remove the swirl. A ceramic transition section after the flow straightener changes the cross section of the channel from the 2,027 mm^2 circular exit of the WSR to the 1,290 mm^2 rectangular entrance to the film cooling rig (FCR). A more detailed description of the assembly components will be provided in the following paragraphs.

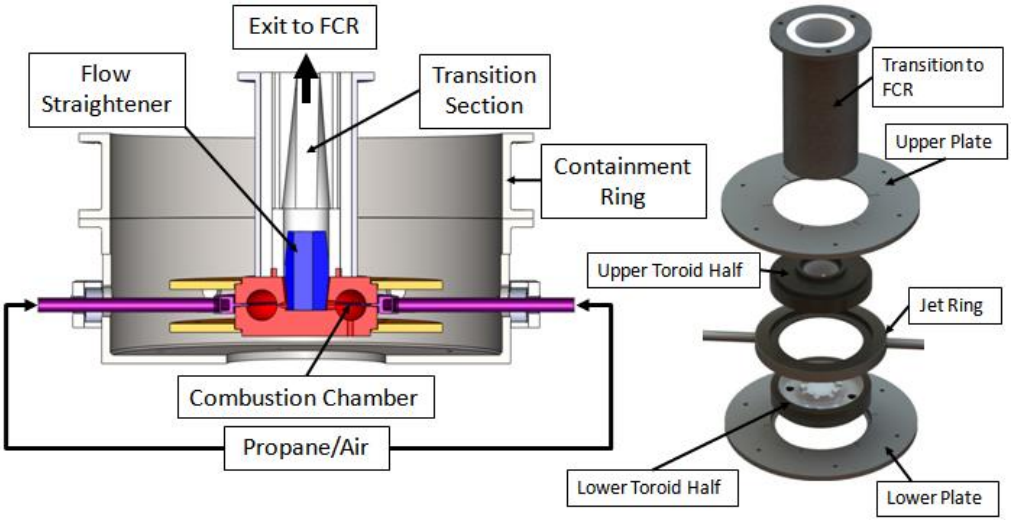

Figure 3-2: Cross section view (left) and exploded view (right) of the WSR.

Inside the WSR toroid, left side of Figure 3-3, the jet ring was fed a premixed supply of air and gaseous propane through fourty-eight 1.6 mm diameter holes angled at 20 degrees to induce swirl. In the bottom of the lower toroid, there were four ports. One of the ports was used to position a B-type thermocouple in the combustion toroid to monitor the combustion temperatures. A second port was used to inject the starting flame from the igniter detailed below. The remaining two ports were unused, but were put in place for flexibility of additional probes to be inserted into the WSR. The inside surface of the toroid was coated with a Yttria-stabilized zirconia ceramic thermal protective coating to reduce the thermal load to the Hastelloy X body of the WSR. Additionally, water coolant loops seen on the right side of Figure 3-3, were located on the outer surface of both toroid halves to provide additional cooling to the WSR. To monitor the temperature of the WSR, four K-type thermocouples were mounted at 90 degree intervals around each toroid half. Two K-type thermocouples were mounted on the jet ring.

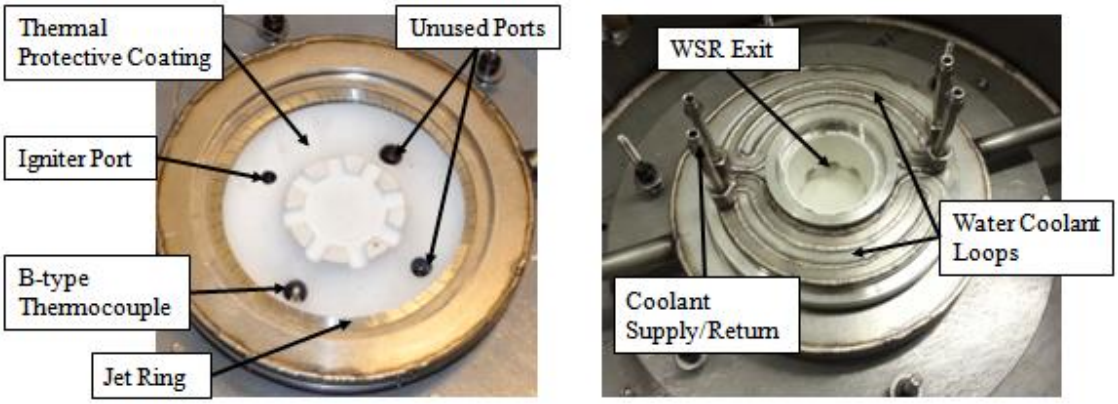

Figure 3-3: Lower toroid and jet ring (left), upper toroid (right)

The igniter used can be seen Figure 3-4. The internal channel features have been outlined using dashed lines. The igniter was machined out of a 25 mm thick 316 stainless steel plate. The length is 76 mm and the width is 51 mm. Three 1/4 inch Swagelok® connectors were screwed into the block to provide air and ethylene in ports, and a flame exit port. A spark plug provided the ignition of the Ethylene/air mixture. A short length of 1/4 inch stainless steel tubing connected the flame exit port of the igniter to the igniter port of the WSR.

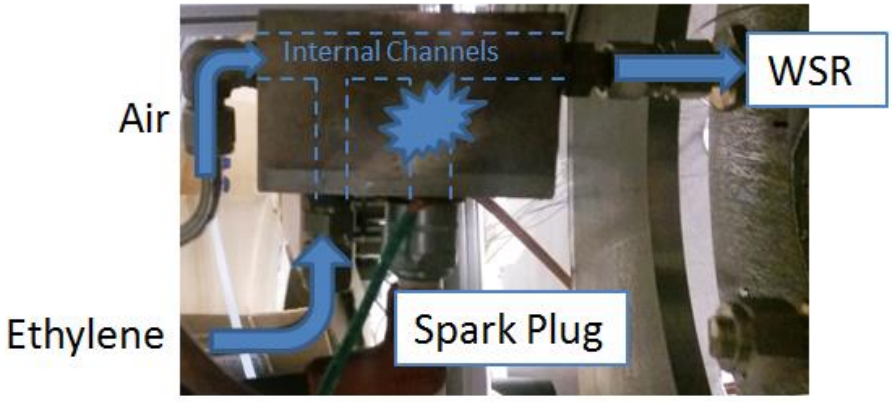

Figure 3-4: Igniter block for the WSR

The WSR was mounted inside of a 3/8 inch thick steel containment ring to protect the surrounding laboratory space from a possible explosion. As seen in Figure 3-5, the

containment ring was mounted to an extruded aluminum frame to hold the rig off of the floor and provide easier access to the bottom of the rig. The rig can be easily removed from the test bay for maintenance by disconnecting the supply lines and lifting it out on the mounting frame. Also shown in Figure 3-5 are the 10 psi check valves located on

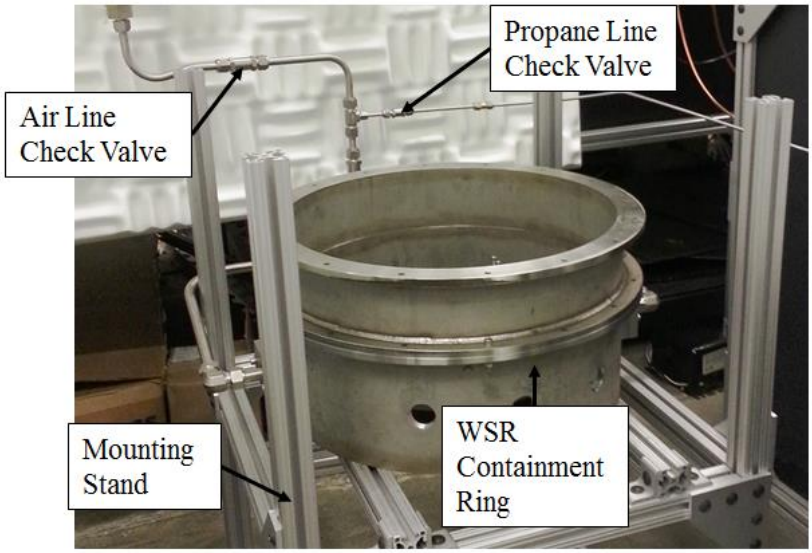

Figure 3-5: WSR containment ring and mounting stand

both the air and propane lines to prevent backflow.

The transition section was comprised of three components, a stainless steel chimney, a soft outer ceramic piece, and firm inner ceramic piece as seen in Figure 3-6. The inner piece was made from nine 25.4 mm thick Type FBD Zirconia discs supplied by Zircar Zirconia, Inc. The outer diameter was 76.2 mm. The inner cross-section tapered from a 50.8 mm diameter circle to a 25.4 mm by 50.8 mm rectangle. Two 6.4 mm holes in each disc kept them aligned by inserting an alumina rod into each set of holes. The outer ceramic piece was a Type ZYC Zirconia cylinder with a 76.2 mm inner diameter and an outer diameter 101.6 mm outer diameter. The Type FBD Zirconia has a consistency similar to blackboard chalk while the Type ZYC Zirconia is much softer. The Type ZYC

is better than the Type FBD at handling the thermal stress without cracking, but the soft structure of the Type ZYC suffers from erosion when exposed to high speed flows. The stainless steel chimney was made from 6.4 mm thick steel and was intended to support a majority of the weight of the film cooling rig. The flow straightener was made from Zirconcia 904 ceramic adhesive and cast in molds at AFRL. It is held in place by notches in bottom disc of the ceramic stack. Corresponding teeth on the end of each blade of the flow straightener fit into these notches to prevent the straightener from moving or rotating. The flow straightener was identical to the one used by Shewhart [26].

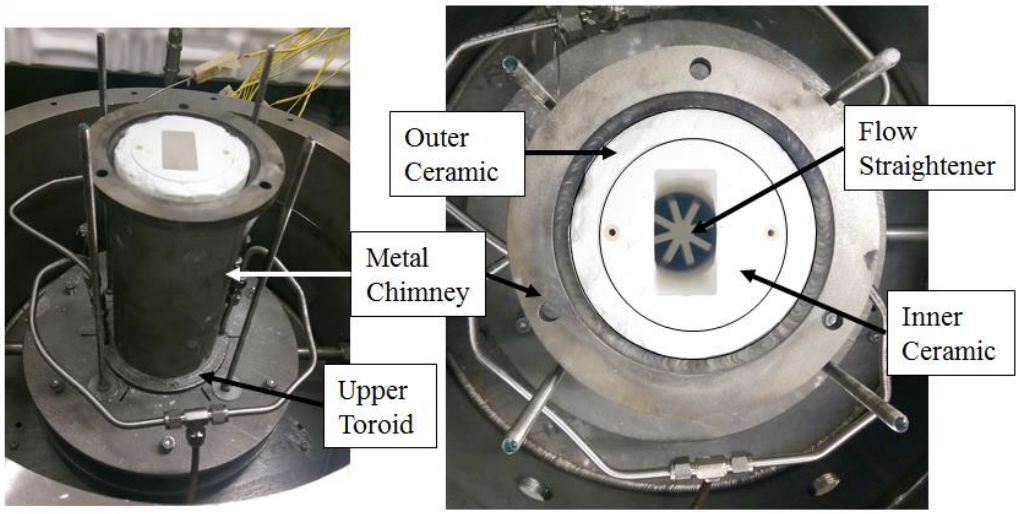

Figure 3-6: WSR to FCR transition section

3.2 Film Cooling Rig

The Film Cooling Rig (FCR) was mounted on top of the transition section of the WSR. The FCR, seen in Figure 3-7 provided a versatile platform for testing film cooling schemes. A modular design allowed for test plates and instrumentation blocks to be interchanged as needed. Fused Silica windows allowed optical diagnostic access of the test channel, while a sapphire window provided IR access to the test plate. The plate

opposite of the test piece was movable to allow for variations of the mainstream Mach number by varying the test channel flow area. Cooling loops on the backside of the main block allowed the test plate side channel wall temperature to be controlled. Details of these components will be presented throughout this section.

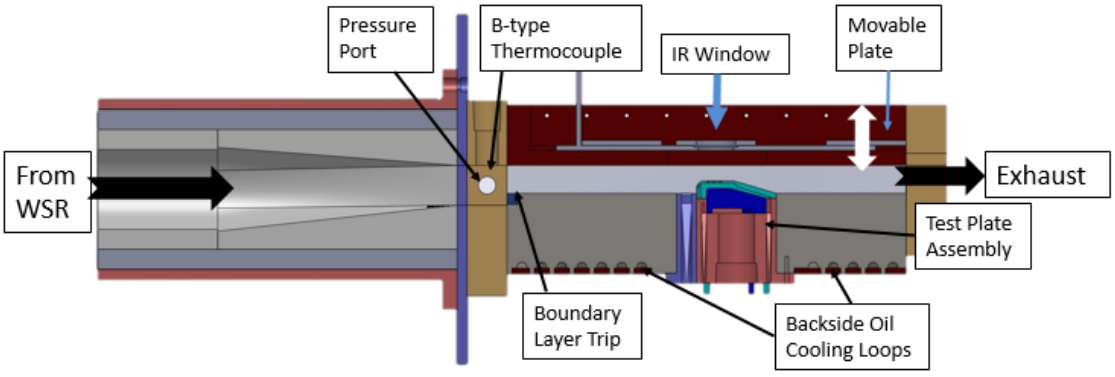

Figure 3-7: 3-*D* model cross-sectional view of the film cooling rig.

The weight of the FCR was primarily carried by the stainless steel chimney. Four ¼ inch threaded steel stabilizing rods anchored the transition plate to the upper plate of the WSR, as seen in Figure 3-8. Springs under the nuts prevented stresses of thermal expansion from becoming a major concern. Three bolts attached the transition plate to the chimney. A layer of FiberFrax® between the transition plate and the chimney helped create an air tight seal. Four bolts attached the base plate to the transition plate. The main block is attached to the base plate with two countersunk bolts with the bolt head on the bottom side of the base plate. The front block was fixtured to the base plate with two bolts.

To assemble the FCR, first the transition plate was bolted to the top of the chimney. The main block was bolted to the base plate before mounting it to the transition plate because the bolt heads were located between the transition plate and the base plate. Then

the base plate/main block assembly was bolted to the transition plate. The front plate was then connected to the base plate. Finally, the top bracket plate was bolted to both the main block and front block. From this point, all of the additional attachments could be mounted onto the FCR.

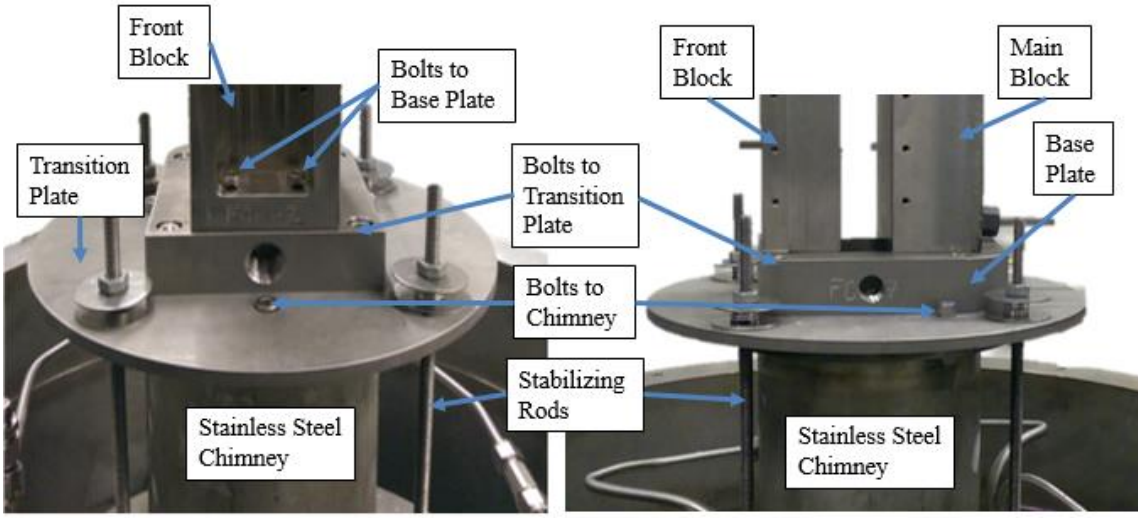

Figure 3-8: Mounting of the FCR to the WSR.

Figure 3-9 displays a rendering of the Main Block of the FCR with flow passing over the top of the image from left to right. A 7 mm step at the start of the block was designed to trip the boundary layer on the test plate side of the channel to turbulent. This allowed the boundary layer profile to be more predictable for estimating the amount needed to be removed by the boundary layer bleed slot described in Section 3.3. A rectangular slot was cut into the block to mount both the test block assembly and boundary layer bleed slot. Heat transfer oil was supplied to coolant loops on the backside of the Main Block by 1/4 inch stainless steel tubes adjacent to the test block mounting slot as seen in Figure 3-10. This allowed the highest level of temperature control immediately adjacent to the test plate. The oil coolant exited through 1/4 inch tubes near inlet and outlet of the test

channel. Seven #5-40 threaded holes were drilled into the block on each side to mount plates to hold the quartz side channel windows in place.

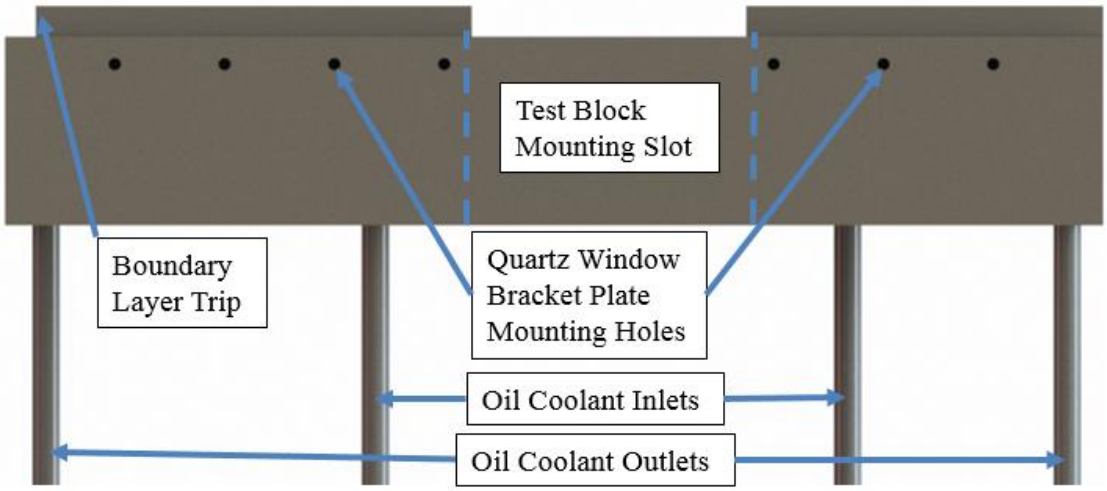

Figure 3-9: 3-*D* rendering of the Main Block of the FCR

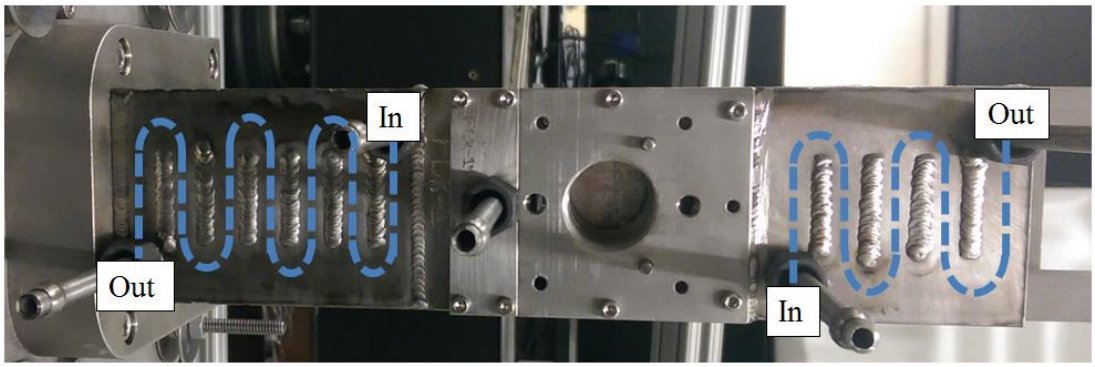

Figure 3-10: Backside view of the main FCR block. The paths of the oil coolant loops have been marked.

Figure 3-11 shows a view of the FCR looking at the Front Block. The Front Block had threaded holes on both sides, visible in Figure 3-8 and Figure 3-12, to mount the other quartz window bracket in place so that the quartz window was held on both sides. The IR Window Plate held a 25 mm diameter sapphire window in place and was able to be adjusted left and right in the picture to provide viewing of different locations along the

test plate with an IR camera. The IR window plate was held in place with brackets mounted in eight holes with #5-40 thread.

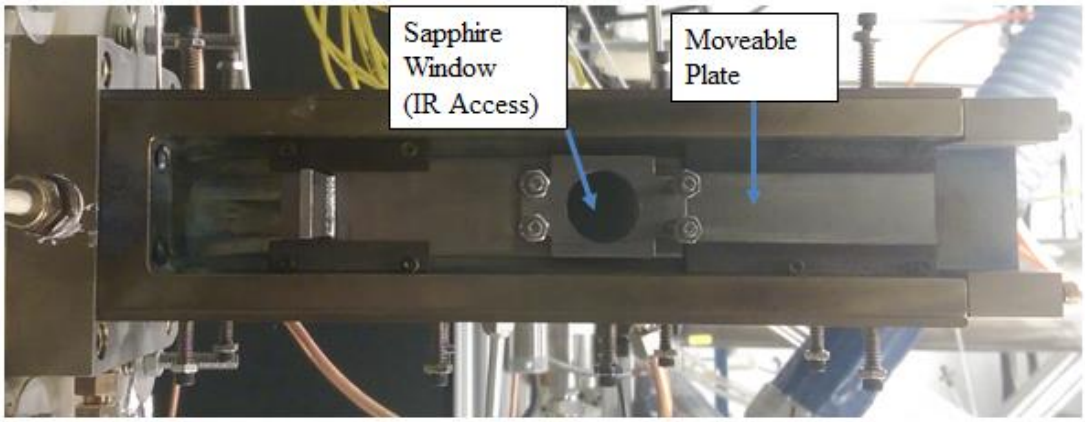

Figure 3-11: View of the Front Block of the FCR, flow is left to right.

Figure 3-12 shows a side view of the assembled FCR. Flow moved from bottom to top of the image with the WSR out of view of the bottom of the image. The flow's temperature and static pressure were measured in the base plate at the inlet to the FCR. This allowed an initial Mach number to be calculated since mass flow rate, and cross-sectional area were also known. With the WSR operating with a 600 SLPM air supply, the Mach number in the base plate was approximately 0.06. Just before the test plate, a portion of the boundary layer on the test plate side channel wall was sucked off. The flow naturally accelerates over the test plate due to a reduction in area. Static pressure taps were placed on the channel wall opposite of the quartz window to measure the corresponding pressure drop to estimate the Mach number over the test plate using isentropic relationships. A thermocouple inserted into the flow at the rig exit measured the FCR exit temperature so the freestream temperature over the test plate could be better approximated.

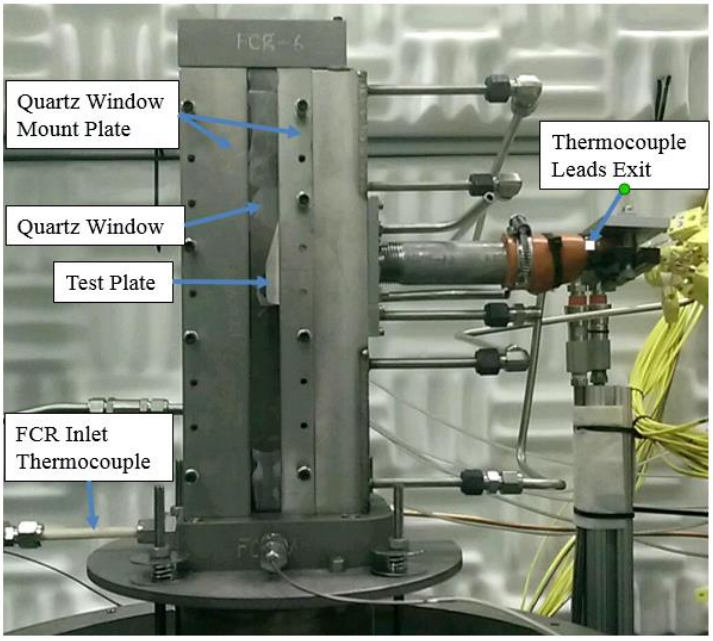

Figure 3-12: Assembled Film Cooling Rig

The rig exhausted out the top into a fume hood. The fume hood was exhausted outside using two fans located in the ducting. For maximum airflow, baffles were used to close off the exhaust hoods for the other test rigs located in the lab with the control box shown in Figure 3-13. To operate the test rig, the "UCC" damper switch was flipped to the "ON" position while the "HVOF" damper, which was used for a separate facility, was left off. Two fans controlled by individual power switches supply the exhaust flow. Details of the startup procedure can be seen in Appendix A.

Figure 3-13: Damper control box switches

3.3 Test Block Assembly

The test block assembly was a modular, removable assembly inserted into the slot cut into the main block of the FCR. The test block assembly provided a flexible platform for testing multiple cooling configurations, including showerhead rows, trenches on the flat section, cylindrical holes on the flat section, and combinations of showerhead and flat section cooling. The test block assembly provided both the boundary layer bleed for the test wall, and the coolant gas for the film cooling studies. Additionally, thermocouples were imbedded into the assembly to provide temperature and heat flux measurements of the test plate and surrounded flows.

The test block assembly, seen in Figure 3-14, is an assembly of three parts, the main cooling block, the lower insert, and the test plate. All three pieces were made from Hastelloy X alloy. The lower insert and test plate were mounted to the main cooling block using 3.2 mm diameter rods with threaded tips on the lower insert and the test plate pass through holes on the main cooling block; four rods for the test plates, and two on the lower insert. The lower insert and the test plate were secured in place with nuts on the

back side of the main cooling block. The main cooling block was attached to the main block of the FCR with four bolts. Three of the clearance holes for these bolts can be seen in Figure 3-14.

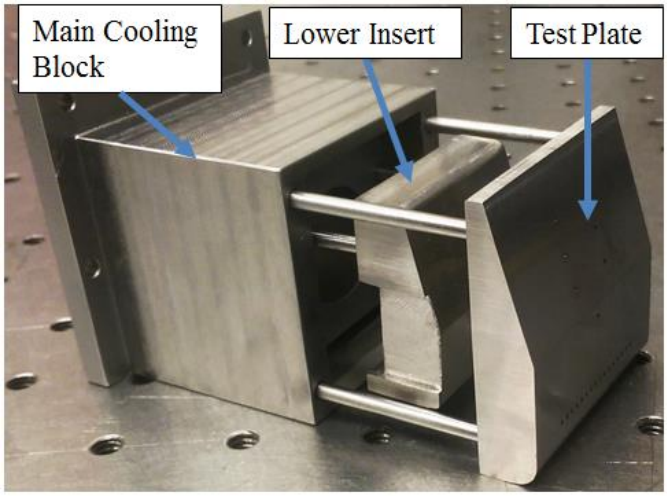

Figure 3-14: Test block assembly

Figure 3-15 shows a cross sectional view of the test block assembly including the boundary layer bleed slot. The large gap in the center of the assembly is for routing the thermocouple leads which will be described in more detail in Section 3.3.1. The lower slot is to remove a majority of the approach boundary layer. The boundary layer bleed gas removed was 20 to 25 SLPM depending on the test condition. Using standard turbulent boundary layer velocity profiles from White [31], about 1.1 mm of the boundary layer thickness was drawn away achieving a minimum velocity striking the test plate of 75 percent of the freestream. The boundary layer bleed and cooling exit flows were driven using a vacuum pump.

Film coolant flow was provided through a supply port on the lower portion of the assembly as viewed in Figure 3-15. Excess coolant could be removed by a separate port at the top of the image. The flow of all three ports was controlled by MKS 1500 series

thermal mass flow controllers. This allowed the level of film cooling and internal cooling to be controlled. The amount of film cooling supplied was calculated based on the Mach number over the flat section of the test plate. The plate with the most coolant hole area contained 93 0.51 mm diameter holes. In order to prevent coolant stagnating in the exit side of the channel with this plate, additional coolant was supplied equivalent to the coolant required for two rows of holes on the flat section; i.e. 31 holes. This extra 31 holes of coolant was removed through the cooling exit port so that the blowing ratio of the film was unaffected. If flow dynamics allow, plates with less than 93 holes will still have the same amount of coolant supplied to the inlet for each blowing ratio. However, the flow through the exit port will be increased so that the blowing ratio is maintained.

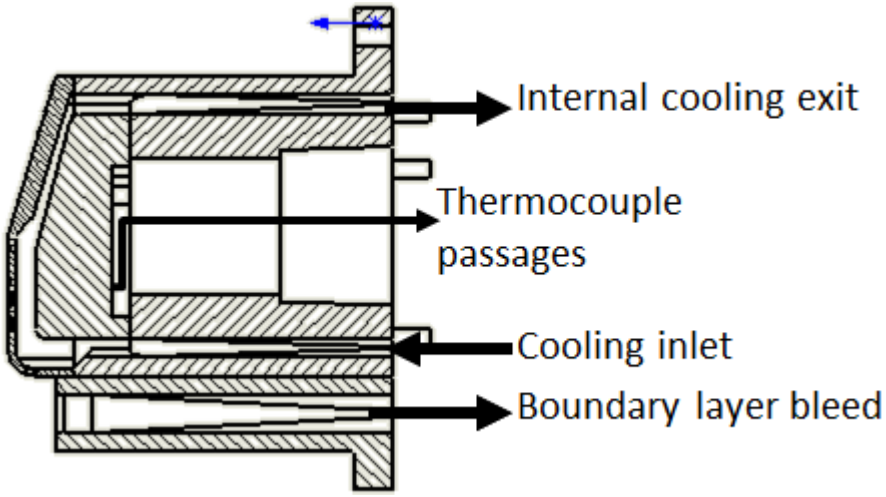

Figure 3-15: Cross section view of test block assembly with boundary layer bleed slot.

As the coolant mass flow increased, it was neccesary to preheat the gas to achieve the desired 730-750 K temperature in the internal channel. The coolant was heated using an Omega AHPF-121 1200 W inline heater placed between the coolant mass flow

controller, and the coolant inlet port of the test plate assembly. The power of the heater was controlled using a dial operated variable power supply box.

The boundary layer bleed gas, and the coolant withdraw flow needed to be cooled from 1450 K to below 340 K prior to passing through their repsective mass flow controllers. The boundary layer bleed air was flowed through a concentric tube, counter-flow heat exchanger 1.2 m in length. Cooling was supplied with the upper WSR toriod coolant water flowing overing the outside of a ¼ inch diameter copper tube carrying the boundary layer bleed gas. The outer tube was contructed from ½ inch steel tubing. At the base of the heat exchanger, the gas entered a stagnation chamber which doubled as a water trap to allow the water vapor to condense out of the gas prior to entering the mass flow controller. The water trap was connected to the flow line using swagelok fittings allowing it be be disconnected and emptied at the end of each day. The water was estimated to be approximately nine percent of the mass flow.

The coolant withdraw flow also needed to be cooled, but since it did not require the same level of cooling as the boundary layer bleed as it only needed to be cooled from a maximum of 900 K. Also, it did not require a water trap since the flow was dry air or nitrogen. The flow passed through a ¼ inch copper tube which looped for about 1 m in a bucket of water before mass flow controller.

3.3.1 Test Plate Instrumentation

The test plate assembly also contained 18 thermocouples to provide heat flux measurements and calibration data for the IR camera. Their locations can be seen in Figure 3-16. Seven surface thermocouples recorded the wall temperature of the freestream side of the test plate. Each surface thermocouple had a duplicate on the

backside of the test plate. Together, these thermocouples provided the ability to calculate the heat flux through the test plate at each thermocouple location using Fourier's Law seen in Equation 3-1.

$$q'' = k\frac{dT}{dx} \qquad \text{Equation 3-1}$$

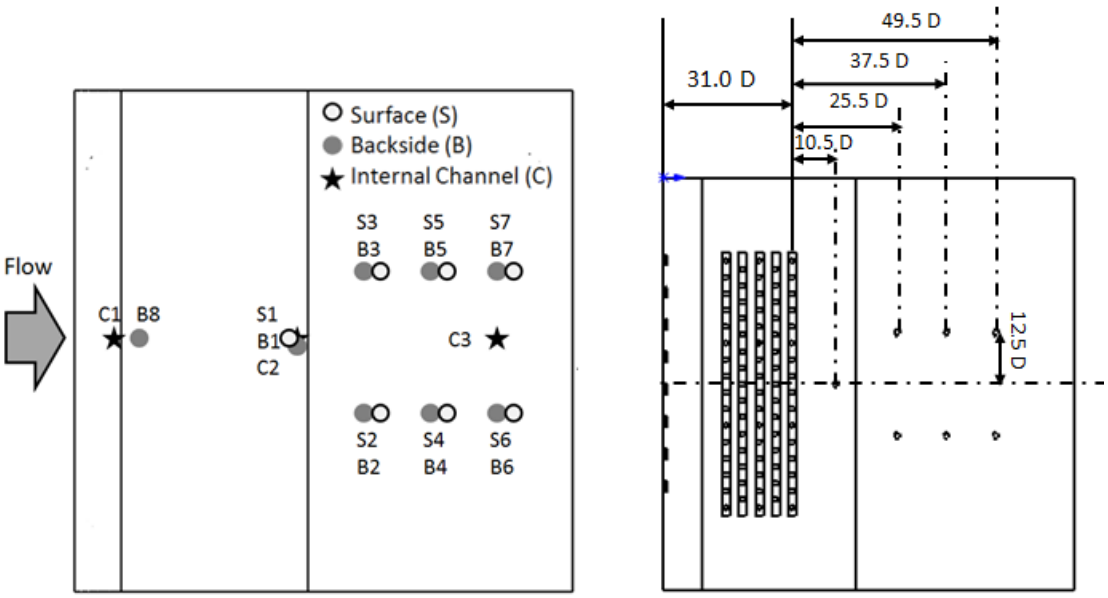

Figure 3-16: Thermocouple placement on the test plates

The conductivity of the Hastelloy X is provided by the manufacturer and can be approximated using Equation 3-2 [32].

$$k\left(\frac{W}{m\cdot K}\right) = 0.0194\left(\frac{W}{m\cdot K^2}\right) * T\,(K) + 4.0\left(\frac{W}{m\cdot K}\right) \qquad \text{Equation 3-2}$$

The nominal wall thickness at each thermocouple location is given in Table 3-1. The thickness tolerance was specified ± 0.13 mm. The thermocouple placement of the backside thermocouples was approximately within 1 mm of a line passing through the surface thermocouple, and normal to the surface and extending to the backside surface of the test plate. However, the backside thermocouples were placed by hand on the lower

insert and bent to protrude through the internal channel to touch the backside of the test plate when the test block assembly is assembled. The exact streamwise and spanwise placement of the backside thermocouples was not seen as critical due to the high conductivity of the Hastelloy. A displacement of 1 mm would not affect the temperature measurement by more than a few Kelvins. Furthermore, due to the recessed cavity in the test plate that created the internal channel, the final location of the thermocouples on the test plate could not be measured. However, this method of locating the backside thermocouples had some unseen shortcomings which limited the ability to accurately obtain the backside wall temperature, mainly ensuring the thermocouples made contact with the backside wall. A more detailed discussion of this problem is presented in Chapter 4.

Table 3-1: Nominal test plate wall thickness

Location	Wall Thickness (mm)
B1	1.27
B2	3.175
B3	3.175
B4	3.175
B5	3.175
B6	3.175
B7	3.175
B8	1.27

With the approximate heat flux known at several locations on the test plate, the convective heat flux coefficient of the internal channel was estimated using Equation 2-2. The wall temperature was provided by the backside surface thermocouples. The internal channel temperature was measured using three thermocouples leaving the convective heat transfer coefficient as the only unknown. The overall effectiveness could be computed using Equation 2-4. C1 was used for the coolant temperature. A surface mapping of the

overall effectiveness was generated through use of the IR camera to capture the surface temperature of the test plate. The setup and calibration of the IR camera will be discussed in Section 3.4.

Routing the thermocouples required machining passages into the test block assembly seen in Figure 3-17. Recesses were cut into the sides and the mating surface of the lower insert to allow the thermocouple lead to pass around and underneath the lower insert. A 22.2 mm diameter hole in the center of the main cooling block was large enough for miniature 2-prong connectors on the thermocouples to pass through. A 102 mm length of ¾ inch steel pipe was screwed into the external side of the main cooling block. This allowed silicone to be used to seal the pipe without melting or catching fire from the heat of the FCR.

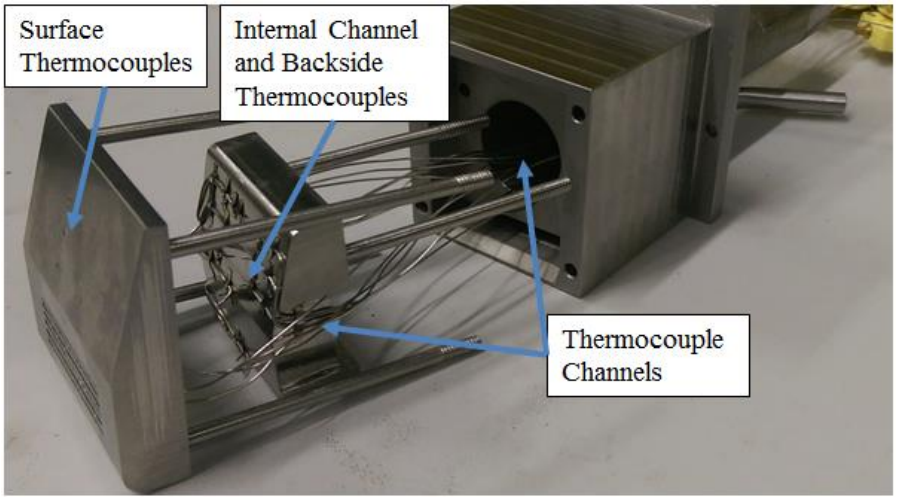

Figure 3-17: Thermocouple routing through the test block assembly.

3.3.2 Test Plates

Figure 3-18 shows a cross sectional view of a test plate. The radius of the leading edge was 4.76 mm to give the test plate a *2r/D* of 18.7 with the hole diameter of the film

cooling holes equal to 0.51 mm. The hole diameter was chosen to match the work of Shewhart [26] and Lynch *et al.* [25]. The curvature of the test plate was chosen based on the geometry used by Rutledge *et al.* [19]. The thickness of the test plate over the region of film cooling injection is 1.27 mm to be consistent with literature for a *t/D* of 2.5. The wall thickness was increased in the taper section to provide more accurate heat flux measurements from thermocouple pairs 2 through 7.

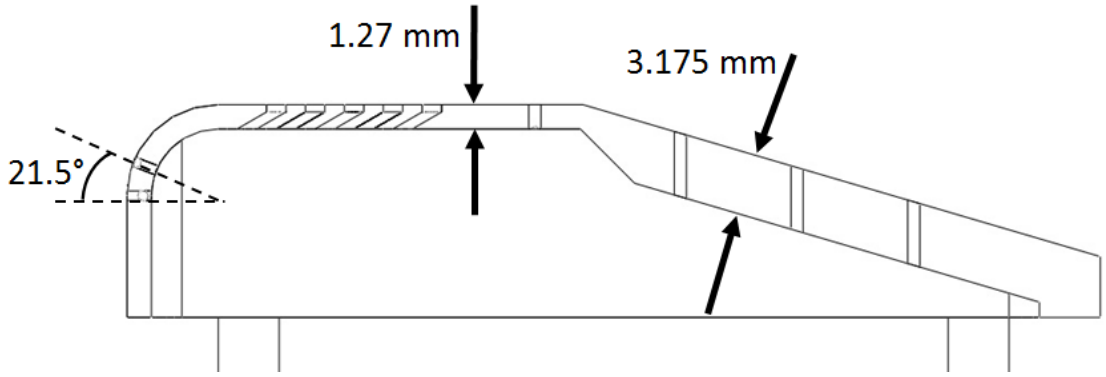

Figure 3-18: Cross sectional view of a test plate.

Three plates were constructed in this study as seen in Figure 3-19. The first plate was the "One Row Cylindrical". It contained a single row of 16 coolant holes with a 30 degree angle and a 4 *D* pitch. The row was located 14 *D* from the leading edge of the plate. This plate will provide a baseline for future studies for row build up analysis similar to the work by Shewhart [26] for flat plate studies.

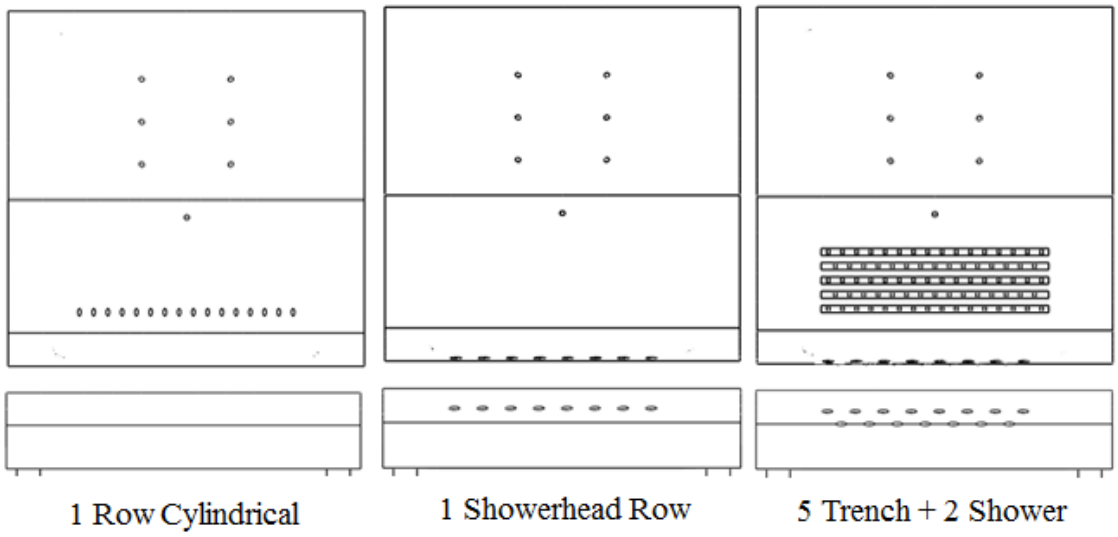

Figure 3-19: Test plate hole configurations

The second plate was the "One Showerhead Row". The holes on this plate were a scaled down replica of the hole used by Rutledge *et al.* [19]. The plate had eight film cooling holes located 21.5 degrees from the start of the quarter circle as seen in Figure 3-18. The hole orientation had a 90 degree streamwise component and a 70 degree spanwise component. The hole spacing was 7.86 *D*. This plate will be used to study the contribution of the heat release from reactive leading edge cooling and enabling scaling analyses between room temperatures and combustion temperatures.

The third plate was the "5 Trench + 2 Shower". This plate contained the same row of showerhead coolant as the "One Showerhead Row" plate, plus an additional row of identical holes located on the start of the quarter circle with a staggered offset. The flat surface of the test plate contained 5 rows of holes in trenches which Lynch *et al.* [25] found to be effective at reducing heat flux, even with reactive film. The first row was located the same 14 *D* downstream from the leading edge as the row on the "1 Row Cylindrical" plate. The rows had a 4 *D* spacing. Each trench was 2 *D* in width, 62 *D* in

length, and 0.75 *D* deep. The coolant holes had a 30 degree streamwise angle and a 4 *D* pitch. This plate was designed to simulate the cooling of the entire suction side of a turbine blade. Planned future cooling configurations will include three rows of cylindrical holes, five rows of cylindrical holes, and five rows of trenches possibly combined with different combinations of showerhead coolant rows.

3.4 IR and Optical Cameras

A FLIR SC 6700 IR camera system was used for this study to capture surface temperature measurements of the test plate. The camera was connected to a computer running ExaminIR camera control software. The IR camera viewed the test plate through the 25 mm diameter sapphire window shown in Figure 3-11. None of the preset factory calibrations proved useful for this study due to an unknown radiation surface characteristic of the test plate, and the high surface temperatures. Therefore, a custom calibration had to be conducted. The camera was set to record 30 frames per second for two seconds. The frame integration time used was 0.01008 ms. A 3.75 to 4.02 micron passband filter was used as this range did not contain any emissions or absorptions from the combusted product flow in the test section. Therefore, the IR camera was able to directly observe the airfoil surface over this wavelength band. A frame size of 120 by 120 pixels was used.

The raw IR camera data contains the number of "counts" recorded by each pixel of the sensor. This is a measure of the radiative heat flux of the captured by the camera and it can be expressed using Equation 3-3 where *a* and *b* are constants.

$$counts = aT^4 + b \qquad \text{Equation 3-3}$$

The constant *a* represents a combination of Boltzman's constant, the emissivity of the surface, and the transmissivity of the sapphire window. The constant *b* is an offset to account for the camera's inability to detect radiative emissions below a certain threshold. For the calibration, 60 frames recorded by the camera were averaged into a single image. The temperature was acquired using the surface thermocouples. The corresponding "counts" measurement was taken from the averaged IR image from a location immediately next to each surface thermocouple. The value over each thermocouple could not be used because the thermocouple weld had a different emissivity than the rest of the test plate. Using Excel, a plot of "counts" versus T^4 was generated and a linear regression trend line was fit to the data as shown in Figure 3-20. This trend line gave the values for *a* and *b* of 3.882 E-9 and 3,320 respectively, and an R^2 value of 0.9899. Using MATLAB, the IR images could be converted from counts into temperature contours by computing surface temperature using Equation 3-3 with the known *a* and *b* values. The data plotted came from multiple days of testing at equivalence ratios of 0.8 and 1.3. Thus, the calibration was valid for both reactive and non-reactive film studies.

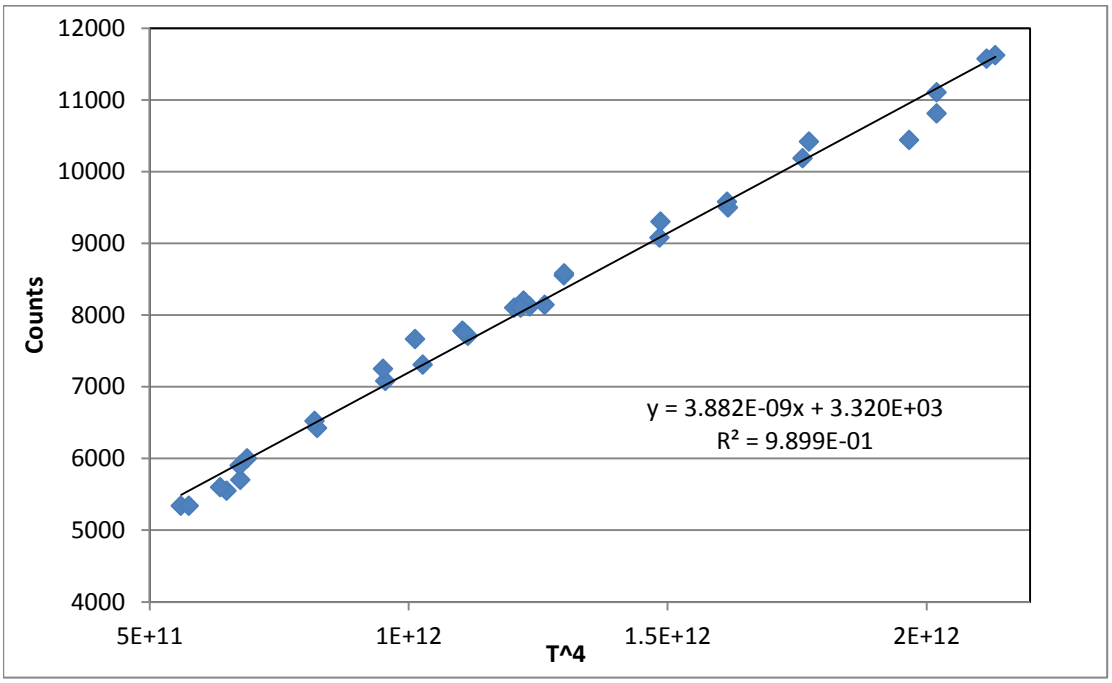

Figure 3-20: IR calibration plot

To gain a better understanding of the extent of the reactive film, visual images were acquired with a Nikon D5100 Digital SLR camera viewing through the side quartz window. The camera settings were 2 second shutter time, ISO 100, and f/16 aperture setting. The long shutter time averages out any unsteady effects, and the small aperture setting was used to maintain contrast in the image.

3.5 Laboratory Equipment

This experiment was housed in the Combustion Optimization and Analysis Laser Laboratory (COAL Lab) at AFIT. The new FCR makes maximum use of the facilities and equipment already in place: the COAL Lab Control and Data Acquisitions computer (CDAC), fume exhaust hoods, compressed air supply, and access to a tank farm with calibration gases for the emissions analyzer, compressed liquid propane tanks and vaporizers, ethylene-air ignitor, a Nitrogen tank, and a Mokon oil cooling system.

The WSR air control, thermocouples, and pressure measurements were accomplished using the COAL Lab CDAC through a Labview program based on the pre-existing program designed to operate the lab's Ultra Compact Combustor. A bank of 16 thermocouple jacks was added to the thermocouple panel jack array in the test cell and integrated into the Labview code to provide the capacity required to operate both the new WSR and FCR in conjunction with the lab's existing Ultra Compact Combustor facility. This board contained ports for 14 Type-K and two Type-B thermocouples. Pressure measurements were made using an Iridium pressure system operated through a Labview user interface.

Compressed air could be supplied by two sources, either the lab's dedicated compressor, or from the building's supply which is shared with the adjacent labs. Since the air requirement for testing is around 1 kg/min, air was usually taken from the building's main supply. Figure 3-21 shows the valve options for the lab's compressed air supply lines. The WSR was supplied using the ¾" line, and the air film coolant was supplied using the 3/8" line. Nitrogen film coolant had a separate supply line which connected to the 3/8" air line at a three-way valve allowing the coolant gas to be switched during testing.

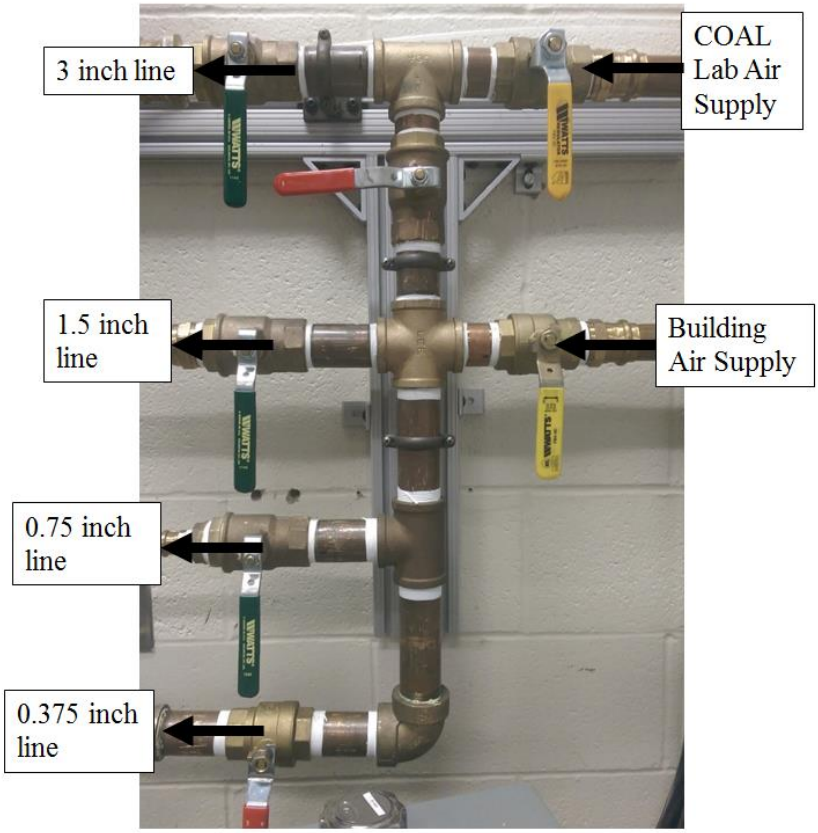

Figure 3-21: Air supply selection valve assembly

Propane was supplied from up to four compressed liquid propane tanks located in the tank farm outside of the lab seen in Figure 3-22. The propane was vaporized in Zimmer liquid propane vaporizers located next to the propane tanks in the tank farm. Each vaporizer was connected to two of the 120 gallon liquid propane tanks. Inside the lab, the propane mass flow rate is controlled with a Brooks Instruments 5853i mass flow controller.

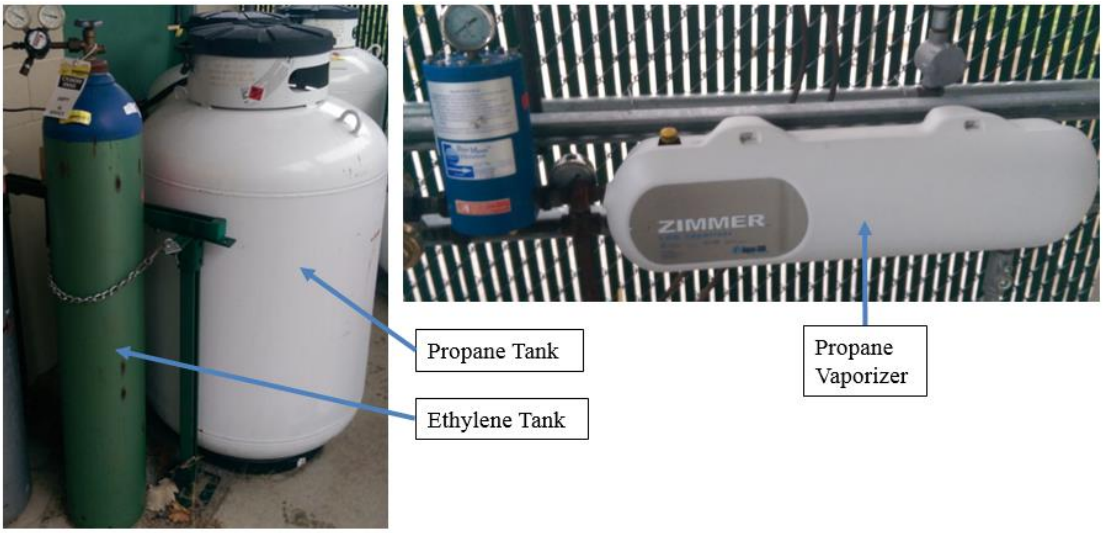

Figure 3-22: Propane and Ethylene tanks (left), propane vaporizer (right)

The integration of the Brooks 5853i mass flow controller into the system for controlling the propane mass flow to the WSR encountered several problems. The use of the Brooks controller for the propane was done to allow the three MKS 1500 series controllers that had previously handled the propane flow to be available for use with the coolant and boundary layer bleed flows. The calibration procedure for the mass flow controllers is provided in Appendix B.

The Brooks controller had not been used for many years, and a new 15 pin *D*-sub data cable to connect the controller to the Brooks 154 control box had to be soldered. Initial testing showed the controller to be functioning properly. However, when it was installed into the system, and set up for calibration, control over the flow was lost. The controller would provide no flow up to 6 percent of its capacity, provide controlled flow between 6 and 15 percent, and went to a fully open valve above 15 percent. The troubleshooting section of the owner's manual provided several possible causes: partially blocked sensor tube, improper sensor winding impendences, or a faulty control board. The sensor

winding impendences were within manufacturer specifications and the sensor tube was cleaned with methanol and 0.007” piano wire as specified by the manual. Neither action solved the problem so the Brooks controller was returned to the manufacturer for repair and the problem was reported to be a faulty control board. Once the Brooks mass flow controller was repaired it was reinstalled in the lab and appeared to function normally.

A Mokon oil thermal management system, pictured in Figure 3-23 provides cooling for the backside wall of the FCR. The machine uses an oil based heat transfer fluid and was operated at 300 degrees F for these studies.

Figure 3-23: Mokon thermal management system

3.6 Uncertainty Analysis

Understanding the potential error in the data is important to drawing conclusions from the data. This analysis was conducted using a constant odds, or root-sum-square method which is given in Equation 3-4.

$$\delta R = \left\{ \sum_{i=1}^{N} \left(\frac{\partial R}{\partial X_i} \delta X_i \right)^2 \right\}^{1/2} \quad \text{Equation 3-4}$$

R is the parameter of interest, X is variable of the parameter, and δX is the uncertainty of that variable. Table 3-2 shows the error percentages for the overall effectiveness measurements. These values were provided by the thermocouple manufacturer. Using typical values seen during the study, the typical error for overall effectiveness is 0.013.

Table 3-2: Error values for overall effectiveness

Variable	Error	Typical Values
T_∞	0.5 %	1430 K
T_c	0.75 %	735 K
T_s	0.75%	1050 K
$\delta\phi$ typical	0.013	

A typical error for the thermal conductivity is given in Table 3-3. This error was based on Equation 3-2 where T is the average temperature between the surface and the backside. With values for the conductivity typically in the range of 20 to 23 $\mathrm{W/m^2K}$, this is a potential error of about 0.5 percent

Table 3-3: Error values for thermal conductivity of the test plate

Variable	Error	Typical Values
$T_{surface}$	0.75 %	1070 K
$T_{backside}$	0.75%	950 K
δk typical	$0.11 \frac{W}{m^2K}$	
k typical	$22 \frac{W}{m^2K}$	
% error	0.5 %	

For the heat flux measurements, the error values are listed in Table 3-4. The thickness error is a combination of the 0.127 mm manufacturing tolerance, and an estimated 0.25 mm placement error based on the radius of the thermocouple probes which are 0.5 mm in

diameter. The typical heat flux values were based on the nominal values for the temperatures, conductivity, and wall thickness (L). The thicker wall provides a more accurate heat flux measurement with an error of 15 percent versus 37 percent for the thin wall location.

Table 3-4: Error values for heat flux

Variable	Error	Typical Values Location 1	Typical Values Locations 2-7
L	0.377 mm	1.27 mm	3.125 mm
$T_{surface}$	0.75 %	1050 K	1070 K
$T_{backside}$	0.75 %	1000 K	950 K
k	0.5 %	$22\ \frac{W}{m^2K}$	$22\ \frac{W}{m^2K}$
$\delta q''$ typical		$3.2\ x\ 10^5\ W/m^2$	$1.3\ x\ 10^5\ W/m^2$
q" typical		$8.7\ x\ 10^5\ W/m^2$	$8.4\ x\ 10^5\ W/m^2$
% error		37 %	15 %

Table 3-5 shows error values for net heat flux reduction which is a comparison of two heat flux values. From the heat flux error analysis above, much of the uncertainty is a result of the potential error in the thickness calculation for the heat flux. This would be a bias error affecting both measurements equally so it would be appropriate to remove the thickness uncertainty from the heat flux for determining the net heat flux reduction error. For this analysis, a typical value for *NHFR* was taken as 0 such that the no-film heat flux and the film cooling heat fluxes are equal. Even though the thickness uncertainty was set to 0, the thin wall magnifies the effect of the temperature uncertainty so that the overall *NHFR* uncertainties are still large.

Table 3-5: Error values for net heat flux reduction

Variable	Error	Typical Values Location 1	Typical Values Locations 2-7
q_0'' or q''	22 %	$8.7\ x\ 10^5\ W/m^2$	
q_0'' or q''	9.0 %		$8.4\ x\ 10^5\ W/m^2$
$\delta NHFR$ typical		0.31	0.13

Table 3-6 shows the error values for the internal channel convective heat transfer coefficient. A bulk of the error in the values is a result of the uncertainty in the heat flux measurements as their percent error is much higher than the temperature.

Table 3-6: Error values for internal channel convective heat transfer coefficient

Variable	Error	Typical Values Location 1	Typical Values Locations 2-7
q"	37 %	$8.7\ x\ 10^5\ W/m^2$	
q"	15 %		$8.4\ x\ 10^5\ W/m^2$
$T_{backside}$	0.75 %	1000 K	950 K
$T_{coolant}$	0.75 %	735 K	735 K
δh typical		$510\ W/m^2K$	$610\ W/m^2K$
h typical		$3300\ W/m^2K$	$3900\ W/m^2K$
% error		15 %	16 %

3.7 Start-up Issues

Up to this point, the discussion has been focused on the design and assembly of the test facility. This section outlines some of the difficulties encountered during the early stages of operation. While the test rig shared many common elements with previous rigs, this was the first time a rig of this design was run at AFIT. As such, the facility required different air flow lines, propane supply and controllers, and rig ignition system, which presented new challenges and obstacles that had to be solved. Early attempts to start the WSR could not produce a stable flame and the rig exhibited a tendency to detonate and extinguish rather than ignite. An examination of the problem revealed that while the ignitor spark plug was firing, there was a significant variation in the flow reading provided by the Brooks mass flow controller, even if no flow was possible or commanded.

Two factors lead to this result. First, the spark plug was not well grounded, and this had been a known problem in the lab. Increasing the size of the grounding wire did little to solve the problem. There was a number of metal tubes connecting the WSR/FCR back to the flow control box where the Brooks mass flow controller was mounted. This was providing a grounding path back through the mass flow controller and giving the Brooks control box an errant signal while the spark plug was firing. This problem was solved by mounting the mass flow controller on a silicon pad and placing a short length of plastic tubing on each side of the controller to insulate it from the spark plug. Additionally, the transformer box powering the spark plug had been replaced recently. The technician who installed the new transformer laid the 120 volt alternating current power cable in the same cable tray as the data cables for the mass flow controllers. None of these cables were shielded allowing for electromagnetic interference. The spark plug transformer power cable was moved to a separate cable tray. These two solutions reduced the variance in the propane flow reading from 7 SLPM to 1 SLPM while the spark plug was firing. With this steadier fuel flow, the rig ignited with a stable flame on a more consistent basis.

The detonations caused by the varied propane flow were undesirable because they caused the quartz and sapphire windows to shift in their mounts, and could damage the ceramics lining the WSR toroid and the ceramic structure on the inside of the transition stack between the WSR and FCR. After a week of successful testing, where data at a Mach number of 0.11 was obtained, the rig was run at a higher Mach number. A drop in the WSR water coolant flow prompted an emergency shutdown to prevent damage to the WSR from overheating. An attempt was made to restart the rig and several detonations occurred without a stable flame which caused the sapphire and quartz windows to shift

requiring the rig to be shut down completely and cooled down to allow the windows to be repositioned. Those two detonations were the latest in around 20 or more that occurred previously when the propane flow control was not stable during ignition.

The next time the rig was brought to test conditions, when the air flow was increased from 400 SLPM to 600 SLPM and the equivalence ratio was increased from 0.8 to 1.3, a "pop" was heard accompanied by an ejection of ceramic pieces from the FCR. The sound of the rig changed significantly as well. Disassembling the rig revealed the bottom piece of the 9 discs which compose the ceramic transition stack had been broken into several dozen pieces. Additionally, the flow straightener had broken into two halves.

The lower three discs of the transition stack were replaced with a piece of Type ZYC zirconia instead of the Type FBD of the original discs. Type ZYC is softer and more easily crushed than Type FBD which is why the later was originally used, but was not on hand for a quick replacement of the part. A new flow straightener was also put into place. The rest of the ceramic stack suffered some damage from the adjustments that had to occur to replace the lower three discs and the flow straightener. Figure 3-24 shows a view down the transition section from the FCR end after the repair was completed. Cracks running in the flow direction of the channel can be seen in the discs. This is typical after the transition section has been exposed to the high temperatures of the rig and is not a concern. However, several small pieces of some of these discs did fall out while moving the stack during the repair of its base.

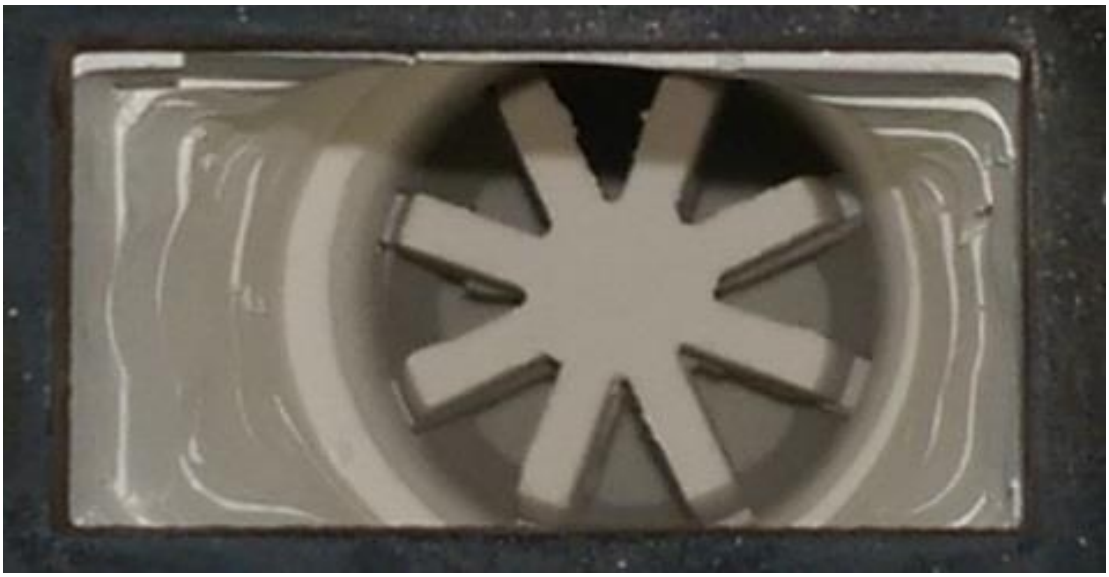

Figure 3-24: A view down the transition section after repair

With the rig repaired, testing was resumed. Again, as the rig was taken to the 600 SLPM of WSR air with an equivalence ratio of 1.3, some unsteadiness in the propane flow caused some small detonations in the rig. The propane supply and the vaporizer are located outside and move through 15 to 20 meters of tubing outside before coming into the laboratory. Suspecting the vaporizer was not capable of sustaining the fuel flow demand without transitioning the fuel back to a liquid state, a second vaporizer was operated in parallel and the equivalence ratio was reduced to 0.8 to test the non-reactive cases first. The rig was successfully brought to a 600 SLPM air flow at an equivalence ratio of 0.8 and held for several minutes. However, a large piece of the ceramic stack loosened into the flow and became stuck in the test section as seen in Figure 3-25. It is suspected a back pressure wave suddenly blocked part of the flow path. The back pressure reduced the propane flow causing the controller is increase the valve opening to maintain the desired flow. As the pressure wave caused by the channel blockage subsided, the propane flow controller overshot the setpoint causing the rig to reach a very

fuel rich state quickly setting off a weak detonation. With the flow path partially blocked, the propane mass flow controller was unable to stabilize and the rig had to be shut down. Testing could not continue as the ceramic transition stack had become structurally unstable and incapable of surviving test condition. A new ceramic stack assembly has been ordered, but did not arrive in time to allow for additional data to be taken for this thesis. However, enough data was acquired to accomplish the goals of the thesis.

Figure 3-25: Large piece of the ceramic transition stack wedged in test section

4. Experimental Results

The first objective of this research was to construct a rig capable of conducting film cooling research at engine temperatures while acquiring overall effectiveness and net heat flux reduction measurements. Chapter 3 outlined the successful completion of this objective. The second and third objectives of developing data acquisition methods to obtain NHFR and overall effectiveness, and refining reduction techniques for evaluating and comparing film cooling results at elevated temperatures will be presented in this chapter.

The test matrix shown Table 4-1 was completed to help characterize the performance of the rig and will be useful for future work which can make use of the full capability of the rig. The results presented here were all obtained with "5 Trench + 2 Shower" test plate with a mainstream Mach number over the test plate of 0.11. The calculation of the mass flow required for a given blowing ratio was based on the ninty-three 0.51 mm diameter holes in the test plate. To simulate the coolant sent to the trailing edge of a blade, and provide additional coolant flow in the internal channel, the equivalent flow of two rows of trenches (31 holes) was added to the total coolant flow, and was also withdrawn from the channel without being ejected as film. However, this extra coolant was not withdrawn from the internal channel for the $\Phi = 0.86$ cases due to the withdraw line being connected to the incorrect mass flow controller.

Several of the blowing ratios contain the phrase "high h." This is to identify the coolant supply and withdraw flows were increased an identical additional amount to leave the blowing ratio of the film unchanged. The amount of increase was two rows equivalent film cooling. The amount of increase was equal to an additional blowing ratio

of 0.5 of coolant. Thus, M = 0.5 high h contained the same total coolant inlet flow as M = 1. This enabled an elevated internal coolant flow (and thus a higher internal h) without changing the blowing ratio (comparing M = 0.5 and M = 0.5 high h, for instance) and also two different blowing ratios at the same total coolant mass flow (comparing M = 0.5 high h with M = 1.0, for instance).

Table 4-1: Completed Test Matrix, all flow values in SLPM.

Daily Repeatability					
WSR Air	**WSR Propane**	***M***	**Air Film**	**Air In**	**Air Out**
400	13.2	0	0	0	0
400	13.2		8	10	2
Nitrogen, Equivalence Ratio = 0.86					
WSR Air	**WSR Propane**	***M* (Intended)**	**N_2 Film**	**N_2 In**	**N_2 Out**
600	21.2	0	0.0	0.0	0.00
600	21.2	0.66 (0.5)	10.7	10.7	0.00
600	21.2	1.33 (1.0)	21.4	21.4	0.00
600	21.2	1.99 (1.5)	32.1	32.1	0.00
600	21.2	2.66 (2.0)	42.8	42.8	0.00
Air, Equivalence Ratio = 0.86					
WSR Air	**WSR Propane**	***M* (Intended)**	**Air Film**	**Air In**	**Air Out**
600	21.2	0	0	0	0.00
600	21.2	0.66 (0.5)	10.3	10.3	0.00
600	21.2	1.33 (1.0)	20.7	20.7	0.00
600	21.2	1.99 (1.5)	31.0	31.0	0.00
600	21.2	2.66 (2.0)	41.4	41.4	0.00
600	21.2	4.0 (3.0)	62.1	62.1	0.00
Air, Equivalence Ratio = 0.8					
WSR Air	**WSR Propane**	***M***	**Air Film**	**Air In**	**Air Out**
600	19.8	0	0.0	0	0
600	19.8	0.5	8.2	10.9	2.72
600	19.8	0.5 high h	8.2	20.9	12.72
600	19.8	1	16.3	21.8	5.44
600	19.8	1 high h	16.3	31.8	15.44
600	19.8	1.5	24.5	32.6	8.16
600	19.8	1.5 high h	24.5	42.6	18.16
600	19.8	2	32.6	43.5	10.88
600	19.8	2 high h	32.6	53.5	20.88
600	19.8	3	49.0	65.3	16.32
Air, Equivalence Ratio = 1.3					
WSR Air	**WSR Propane**	***M***	**Air Film**	**Air In**	**Air Out**
600	32.0	0	0.0	0	0
600	32.0	0.5	8.2	10.9	2.72
600	32.0	0.5 high h	8.2	21.8	13.64
600	32.0	1	16.3	21.8	5.44
600	32.0	1 high h	16.3	32.6	16.40
600	32.0	1.5	24.5	32.6	8.16
600	32.0	1.5 high h	24.5	43.5	19.00
600	32.0	2	32.6	43.5	10.88
600	32.0	2 high h	32.6	53.4	20.80
600	32.0	3	49.0	65.3	16.32

4.1 Net Heat Flux Reduction and Overall Effectiveness

The second objective of this research was to develop the methods required to obtain net heat flux reduction and overall effectiveness values for a variety of film cooling schemes. The instrumentation for acquiring these measurements was discussed in Chapter 3. A representative airfoil with an internal cooling channel was instrumented to allow testing to be conducted in a realistic engine temperature flow environment. Thermocouples were placed on both the internal and external surfaces of the airfoil wall to measure surface temperatures for heat flux measurements, and the internal cavity cooling flow temperature was measured for the overall effectiveness measurements. Table 4-2 displays the thermocouple data acquired for the high equivalence ratio (Φ) test sweep provided here for reference. Similar data was acquired for the other test cases. These data sets were processed to provide heat flux and overall effectiveness.

Table 4-2: Thermocouple data for Φ = 1.3 tests

M	0	0.5	0.5 high h	1.0	1.0 high h	1.5	1.5 high h	2.0	2.0 high h	3.0
WSR Core (K)	1757	1769	1758	1745	1723	1755	1731	1746	1743	1715
FCR Inlet (K)	1611	1616	1615	1610	1608	1614	1607	1609	1609	1606
FCR Outlet (K)	1299	1313	1310	1320	1317	1332	1327	1341	1339	1354
T_∞ **(K)**	1455	1465	1462	1465	1462	1473	1467	1475	1474	1480
$T_{coolant}$ **(K)**	1034	892	809	808	733	740	741	738	736	735
Surface 1 (K)	1180	1224	1204	1117	1099	1009	1014	952	948	897
Surface 2 (K)	1122	1208	1175	1148	1133	1066	1066	1007	1000	944
Surface 3 (K)	1127	1206	1154	1113	1084	1013	1004	952	940	896
Surface 4 (K)	1102	1192	1152	1147	1127	1070	1066	1011	1003	944
Surface 5 (K)	1102	1192	1149	1142	1118	1060	1054	998	989	932
Surface 6 (K)	1066	1152	1120	1139	1122	1083	1081	1031	1026	960
Surface 7 (K)	1068	1154	1112	1124	1097	1054	1044	998	987	934
Backside 1 (K)	1177	1181	1155	1070	1041	964	965	913	906	863
Backside 2 (K)	1034	1002	914	902	862	847	845	824	816	799
Backside 3 (K)	1002	963	794	797	720	725	720	736	723	733
Backside 4 (K)	995	1024	924	906	874	819	814	787	771	752
Backside 5 (K)	982	993	844	875	796	805	779	806	782	777
Backside 6 (K)	1019	1080	1005	1017	969	945	923	899	878	840
Backside 7 (K)	983	1006	868	918	810	861	824	856	807	815

4.1.1 Determination of Heat Flux

Heat flux was calculated using Fourier's Law given in Equation 3-1. *dT* was the temperature difference across the wall at a given location. For example, using data from Table 4-2 at Location 1 with *M* = 1;

$$dT_1 = T_{surface\,1} - T_{backside\,1} = 1117\ K - 1070\ K = 47\ K$$

likewise for the other locations. The wall thickness, *dx* is listed in Table 3-1 for each location and for Location 1 $dx_1 = 1.27$ mm. The average thermal conductivity, *k*, is calculated from Equation 3-2 where *T* is the average temperature of the surface and backside temperature measurements. For this case, *k* = 25.1 W/(m·K). Thus,

$$q_1'' = 25.1\ \left(\frac{W}{m \cdot K}\right) * \frac{47\ K}{1.27\ x\ 10^{-3}\ m} = 9.3\ x\ 10^5\ W/m^2$$

With the heat flux known, it is also possible to calculate the internal channel convective heat transfer coefficient using Newton's Law of Cooling. The channel coolant temperature at this condition was measured behind the showerhead holes at 808 K. The resulting heat transfer coefficient is calculated by:

$$h_1 = \frac{q_1''}{T_{backside\,1} - T_{coolant}} = \frac{\left(9.3\ x\ 10^5\ \frac{W}{m^2}\right)}{1070\ K - 808\ K} = 3500\ \frac{W}{m^2 K}$$

4.1.2 Calculating Net Heat Flux Reduction

Net heat flux reduction was a desired parameter for the first part of the second objective to provide a comparison with Lynch *et al.* [25] and Shewhart [26] as a way to assess the performance of the film. Recall from Equation 2-10 that net heat flux reduction (*NHFR*) is a comparison to the heat flux through the plate with film cooling versus without film cooling. The comparison can be made whether the film is chemically reacting or not. When Lynch *et al.* [25] and Shewhart [26] performed their analysis, they

used the heat flux with no cooling for their baseline no film cooling heat flux. This value was higher than most of their film cooling heat fluxes generating positive *NHFR* values. However, the values for heat flux calculated in this study for no cooling yielded a heat flux an order of magnitude lower than the heat flux values with cooling as shown in Section 4.3.3. The low no cooling heat flux value was a result of the lack of coolant air flow in the internal cooling channel acting as an insulating layer reducing the heat flux as the air gains temperature. If the no cooling heat flux value was used, the resulting *NHFR* would be on the order of -30 which indicate the film has a large detrimental effect, but surface temperature measurements shown in Table 4-2 show this not to be true.

This raised awareness to an important parameter that was not being properly controlled between the cooling and no cooling cases; the backside condition. When Shewhart [26] conducted his heat transfer studies, the backside condition of the instrumentation block was constant throughout all blowing ratios. His instrumentation block was over 40 mm thick with a backside condition of free convection in the laboratory. The instrumentation for this rig was the test plate itself which has a coolant channel for its backside. The heat transfer characteristics of this channel change with blowing ratio as more or less coolant was flowed through it and the coolant temperature varied. When no film cooling is used, the air in this channel slowly absorbed heat resulting in a temperature between 1000 K and 1040 K depending on the external condition, and how much time it was provided to absorb heat.

The question is: what needs to be matched on the backside between heat transfer measurements with and without film cooling in order to obtain *NHFR* values? The initial thought was the channel coolant mass flow needed to be matched. So a test was

conducted where it was intended to have internal cooling only where the mass flow for each test case matched the coolant withdraw flow for each blowing ratio with coolant, seen in Table 4-3. However, since the plate was not changed to a plate without film cooling holes, it was possible for some freestream to be ingested into the showerhead holes, mixing with the coolant flow, and then be ejected from downstream trench holes. In the film cooling tests, the channel exit temperature exceeded the channel inlet temperature or was within a few degrees as expected due to heating of the coolant as it moved through the channel. However, in this case, the channel inlet thermocouple recorded higher temperatures than the exit. The channel inlet thermocouple is located beneath the showerhead coolant holes, so freestream gas was likely ingested through those holes and passed over the channel inlet thermocouple causing it to read high.

Table 4-3: Internal cooling only test set with recorded channel coolant temperatures.

M **equivalent**	**Coolant Supplied (SLPM)**	**Coolant Withdrawn (SLPM)**	**Channel Inlet Temp (K)**	**Channel Exit Temp (K)**	**Typical Inlet Temp (K)** $\Phi = 1.3$	**Typical Exit Temp (K)** $\Phi = 1.3$
0.5	2.72	2.72	978	909	892	924
1	5.44	5.44	901	872	808	835
1.5	8.16	8.16	863	839	739	775
2	10.88	10.88	838	815	738	757
3	16.32	16.32	793	778	735	736

The heat flux did increase over the no coolant cases shown in Figure 4-1 as the coolant flow was increased, but the heat flux values are still lower than the film values. For example, the heat flux for M = 1 at thermocouple Location 1 calculated in Section 4.1.1 was 930,000 W/m^2. However, the internal cooling case with the match channel flow resulted in a heat flux of only 280,000 W/m^2. The heat flux increased with increased

coolant flow and the resulting reduction in coolant temperature. However, the coolant temperature did not match the film cooling case at each blowing ratio due to preheating as it entered the rig. A matching coolant temperature would be 730-750 K for blowing ratios equal to or greater than unity. Therefore, matching the channel coolant flow did not match the backside heat transfer condition between film cooling and no film cooling. The higher coolant temperatures, 863K instead of approximately 739 K for M = 1.5 for example.

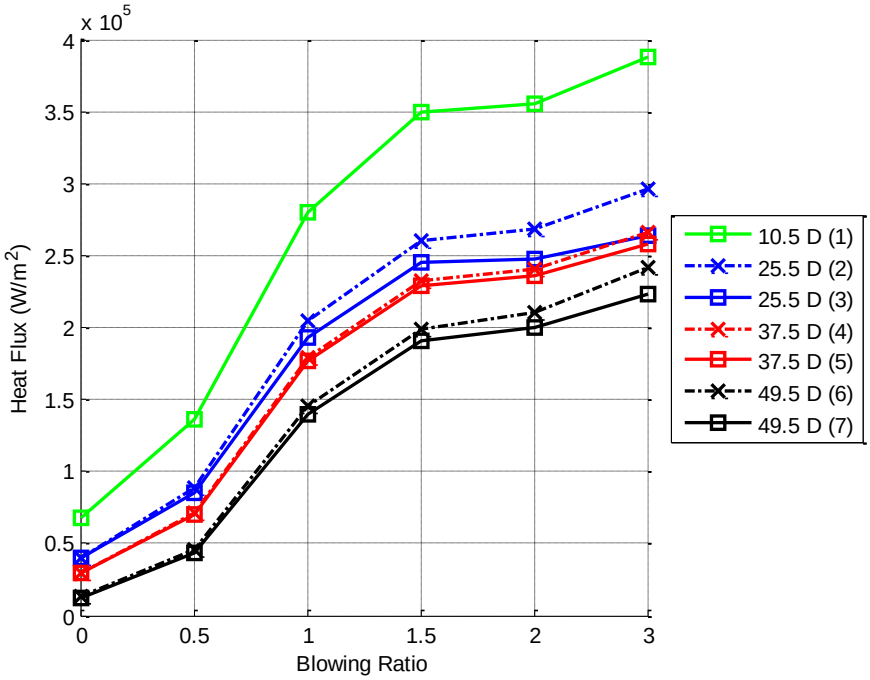

Figure 4-1: Heat flux versus blowing ratio equivalent with internal cooling flow only matching internal cooling flow with film

Matching the internal channel temperature is required because it would create the same driving condition without film cooling as with the film cooling. Increased coolant flow could reduce the channel coolant temperature to match the film cooling cases, but also matching the convective heat transfer coefficient would be difficult. A test set would

need to be conducted to gather heat flux measurements with internal cooling only using a test plate without film cooling holes while trying to match the coolant temperature for each blowing ratio. This solid surface test plate would prevent the ingestion issues seen with attempting to provide a no film condition using a film cooling model as presented in Table 4-3. This would then provide the necessary no-film cooling heat flux values for use in *NHFR*.

In order to provide an example for the calculation of *NHFR*, Table 4-4 displays the recorded surface temperatures from the internal cooling only case. Heat flux can be calculated using a one-dimensional series circuit analogy as shown in Equation 4-1.

$$q'' = \frac{T_s - T_c}{\frac{dx_{wall}}{k_{wall}} + \frac{1}{h}} \qquad \text{Equation 4-1}$$

In this equation, T_s is the external surface temperature. T_c is the internal channel coolant temperature. dx_{wall} and k_{wall} are the wall thickness and wall thermal conductivity, respectively. h is the internal channel convective heat transfer coefficient. Purely for the purpose of demonstration here, the no-film heat flux was calculated using T_s from Table 4-4. The values for T_c and h were taken from the film cooling results in Table 4-2 to have a pseudo matched backside condition.

Table 4-4: Recorded surface temperatures with internal cooling only.

***M* Equivalent**	**Surface 1 (K)**	**Surface 2 (K)**	**Surface 3 (K)**	**Surface 4 (K)**	**Surface 5 (K)**	**Surface 6 (K)**	**Surface 7 (K)**
0.5	1144	1094	1089	1071	1070	1038	1035
1	1126	1082	1073	1060	1057	1030	1025
1.5	1113	1071	1060	1049	1047	1022	1016
2	1108	1065	1049	1042	1039	1017	1008
3	1096	1050	1025	1025	1019	1004	989

Using the values from their respective tests described above for M = 1, or its internal cooling only equivalent, a no-film cooling heat flux value at Location 1 was calculated as follows.

$$q_0'' = \frac{1126\ K - 808\ K}{\frac{1.27\ mm}{25.1\frac{W}{m\ K}} + \frac{1}{3500\frac{W}{m^2 K}}} = 950{,}000\ W/m^2$$

This no-film heat flux value, and the film cooling heat flux value of 930,000 W/m^2 calculated in Section 4.1.1 can then be applied to Equation 2-10 to calculate NHFR as follows:

$$NHFR = 1 - \frac{q''}{q_0''} = 1 - \frac{930{,}000\frac{W}{m^2}}{950{,}000\frac{W}{m^2}} = 0.021$$

While this is not an actual *NHFR* measurement, it does outline the methodology required to obtain *NHFR* for use in future comparative studies. The no-film cooling heat flux reference case for use in *NHFR* calculations must have matching backside conditions to the film cases. The most important parameter being the internal channel temperature since temperature gradient is the largest driver of heat flux. The convective heat transfer coefficient does play a role, but as will be seen in Section 4.3.3 its variation with coolant mass flow is small. Therefore, a method of acquiring *NHFR* has been developed completing the first part of the second objective. It is worth stressing this method is much different from the methods commonly described in the literature where the no-cooling heat flux is acquired by simply shutting down the coolant flow. The reason for the difference is this study uses a representative blade model with an internal coolant cavity. Most film cooling studies use a plenum fed coolant scheme with solid body heat flux

gauges downstream which are not affected by the coolant condition, whereas the blade wall in this study was heavily affected by the coolant condition.

4.1.3 Determination of Overall Effectiveness

The second part of the second objective was the methodology to obtain overall effectiveness measurements. Overall effectiveness, ϕ, is calculated using Equation 2-4. A freestream temperature measurement was not made adjacent to the test plate, but since the test plate was located midway between the FCR inlet and FCR outlet, the average of those two measured temperatures was used for T_∞. In this case, T_∞ = 1465 K. The surface temperature was measured directly with the surface thermocouples that were imbedded in the test plate. The coolant temperature was measured with the internal channel thermocouple located behind the showerhead holes, identified as "C1" in Figure 3-16. Continuing with the example using the values from Table 4-2 for M = 1, the overall effectiveness measurement at Location 1 is computed as follows.

$$\phi_1 = \frac{T_\infty - T_{surface\,1}}{T_\infty - T_{coolant}} = \frac{1465\ K - 1117\ K}{1465\ K - 808\ K} = 0.53$$

In addition to the thermocouple measurements of the surface temperature, an IR image was also taken of the surface for each test condition. The image was processed to provide surface temperatures following the method described in Section 3.4. The image was then further processed to display overall effectiveness where the surface temperature from the image was used in the overall effectiveness calculation and the coolant temperature was assumed to be constant across the span and length of the image. Figure 4-2 shows a sample IR image processed to map overall effectiveness. This image was obtained with M = 1 with a reactive film. The IR images provide information of the performance of the film across the entire surface, not just the locations of the

thermocouples. In this image, the flow is moving from bottom to top and the showerhead rows are ejecting coolant towards the left side of the image. At Location 1 in the image Φ = 0.53, matching the value calculated from the surface thermocouple. Thus, with the ability to calculate overall effectiveness values not only using the thermocouple data, but also the IR images, the second objective of the research to develop the methodology for determining *NHFR* and overall effectiveness values is complete.

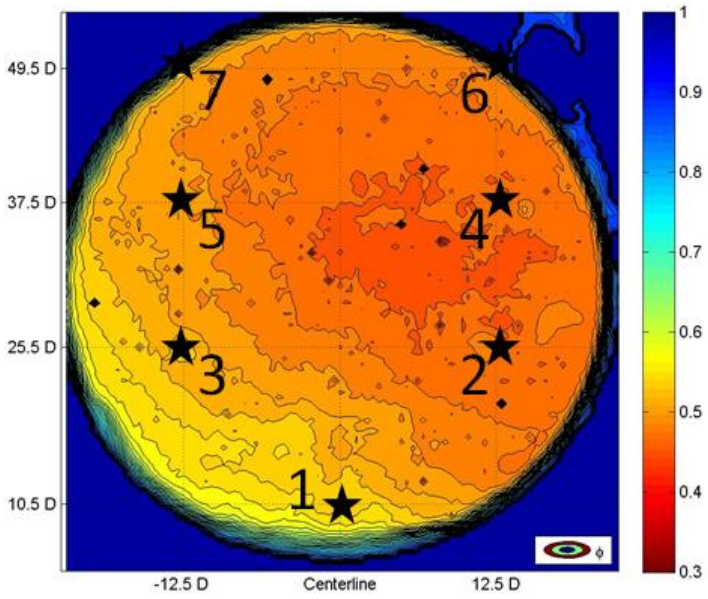

Figure 4-2: Sample IR Φ image with the surface thermocouple locations identified

4.2 Daily Repeatability

With objective 2 complete, the focus of the research shifted to quantifying the results. As tests were conducted over multiple days, it was important to quantify the day to day variability in the rig's operating condition. This was conducted at the conditions shown in the top section of Table 4-1. Figure 4-3 shows the temperature measurements of several thermocouples across four different test days. Overall, the day to day variations were

small. The difference between the air Φ = 0.8 and Φ = 1.3 days was less than 15 K for the WSR inlet temperature. The difference between the two days previously mentioned and the two days at Φ = 0.86 was partially a result of re-calibrating the propane mass flow controller. The zero flow reading for the Φ = 0.86 days was 0.4 SLPM of propane, it was corrected to 0.0 SLPM for the Φ = 0.8 and 1.3 testing.

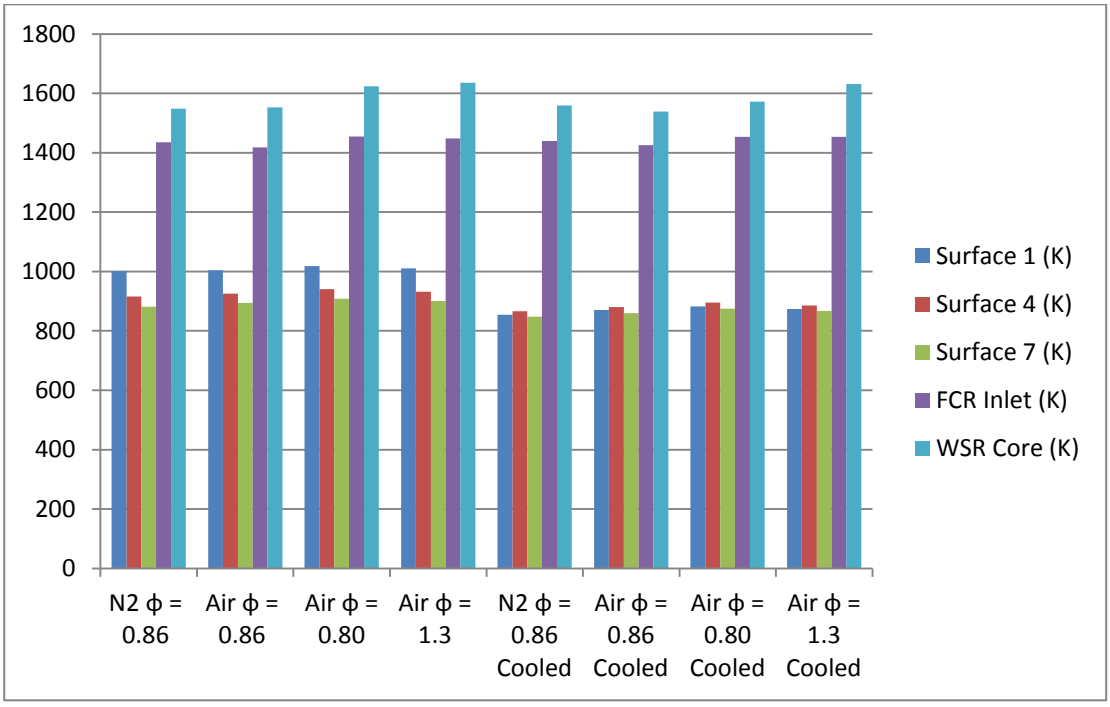

Figure 4-3: Repeatability temperature measurements

4.3 Reactive Versus Non-Reactive Film Studies

The third objective of the research was to develop the technique for evaluating and comparing film cooling studies for different conditions at engine temperatures. These variations in condition could include changes to the film cooling scheme, changes in blowing ratio, freestream Mach number, freestream equivalence ratio, or changes in coolant gas to provide reactive or non-reactive coolant. This study looked specifically at

the differences between air and nitrogen in a nonreactive case. The primary parameter was blowing ratio which was varied between 0 and 3.0. The goal was to study the effects or reactions uncovered by setting the equivalence ratio to either 1.3 or 0.8. The performance metrics for the comparisons were *NHFR* and overall effectiveness (ϕ).

4.3.1 Comparison of Air to Nitrogen at Low Fuel/Air Ratio

There was a desire to verify the film cooling performance of pure nitrogen versus air. Nitrogen would be the non-reactive coolant of choice for high equivalence ratio flows. The goal of this set of tests was to verify that the performance of air in a low freestream Φ case was comparative to a nitrogen coolant in the non-reactive condition. Then any difference between the performance of air and nitrogen in a high freestream Φ environment would be attributed to secondary reactions. The test plate with five rows of trenches and two showerhead rows was selected for this comparison. To accomplish this, it was intended to run both air and nitrogen as coolant with the WSR reactor operating at an equivalence ratio of 0.8. However, there was an error with calculating the propane flow required for this fuel/air ratio. During the initial two days of testing, 1.88 kg/m^3 was used for the standard density of propane in the calculations. This corresponds to the 20 °C standard, but the mass flow controller for the propane operates on a 0 °C standard which results in a density for propane of 2.01 kg/m^3. This difference in density resulted in 21.2 SLPM of propane being supplied to the WSR instead of the intended 19.8 SLPM, which increased the equivalence ratio from 0.8 to approximately 0.86 as shown in Table 4-1. The density value in the calculation was corrected, but after the supply of Nitrogen available had been consumed.

Furthermore, in the initial test where air was used as a coolant, the FCR inlet temperature was 50-60 K higher than it was for the test nitrogen was used as a coolant. There was also a noticeable orange flame at the FCR exit during the air test day. If a flame formed at the oxygen rich exit plane of the FCR, it is also possible a flame formed from the oxygen rich film cooling. It would have been difficult to see an orange flame in the film due to the background being orange as well from the glow of the hot surfaces of the flow channel. Because of the higher temperature and the noticeable flame at the FCR exit, this initial air data was not used for the air to nitrogen comparison.

With the issues above in mind, a comparison was made between the nitrogen blowing ratio sweep with the slightly richer than intended WSR equivalence ratio, and the equivalence ratio of 0.8 blowing ratio sweep with air coolant. Figure 4-4 displays heat flux measurements versus blowing ratio for air and nitrogen with the WSR operating at an equivalence ratio of 0.8 and 0.86 for air and nitrogen respectively. If nitrogen and air cool similarly for a non-reactive film layer, then there should be an agreement between the two. The results were close, but there was a noticeable difference between the air and nitrogen, particularly at the higher blowing ratios. This was likely a result of the air having had internal coolant flowing through the internal cavity. The flowing coolant of the air cases, versus the stagnate coolant of the nitrogen cases would have lowered the backside wall temperature. The lower backside wall temperature increased the heat flux as seen on Figure 4-4 with a 10 and 50 K lower temperature reading for the air set versus the nitrogen set depending on the location and blowing ratio. The 10.5 *D* location was close to the final row of coolant, so it likely experienced sufficient mixing with the incoming coolant to maintain consistent wall temperatures for both cases.

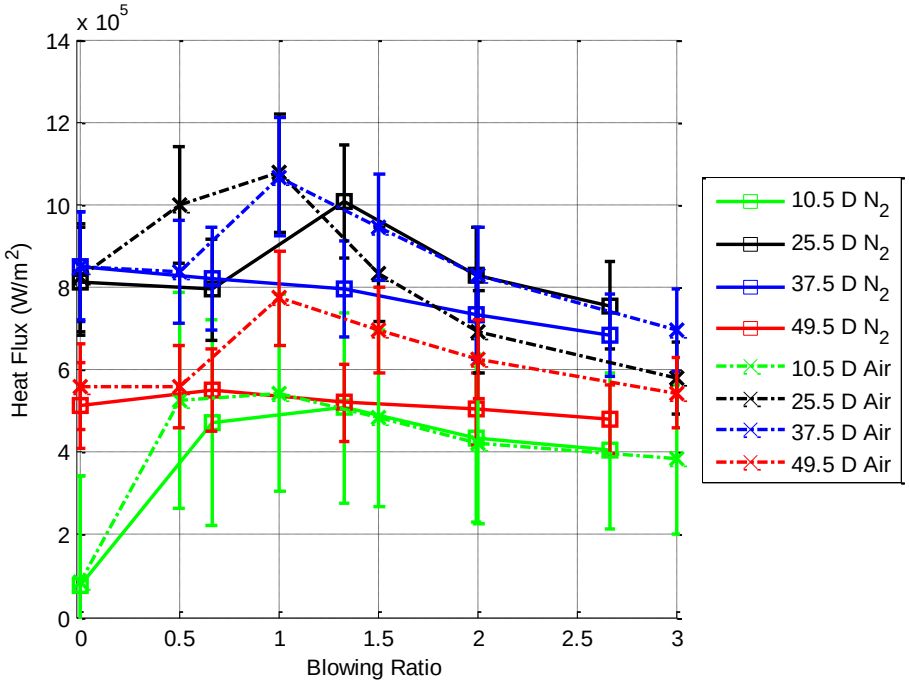

Figure 4-4: Heat flux versus blowing ratio comparison for air and nitrogen

Figure 4-5 shows overall effectiveness versus blowing ratio for the air and nitrogen comparison. The FCR exit temperature indicated a 300 K drop in freestream temperature was expected through the length of the rig. Since the test plate was located midway between the inlet and the exit of the FCR, 150 K was subtracted from the FCR inlet temperature for each data point to obtain the T_∞ used for the overall effectiveness calculations. As with the heat flux, the results were similar between the gases, with the air coolant gaining an advantage at the higher blowing ratios. This was likely a result of the internal coolant of the air lowering the surface temperature slightly causing a small increase in the overall effectiveness. These values are in agreement with the values reported by Andrews [18] for full coverage film cooling. Overall, the different coolant gases show similar results. Nitrogen will make an acceptable coolant substitute to gather

non-reactive film data at high Φ conditions to compare with the reactive results from an air coolant.

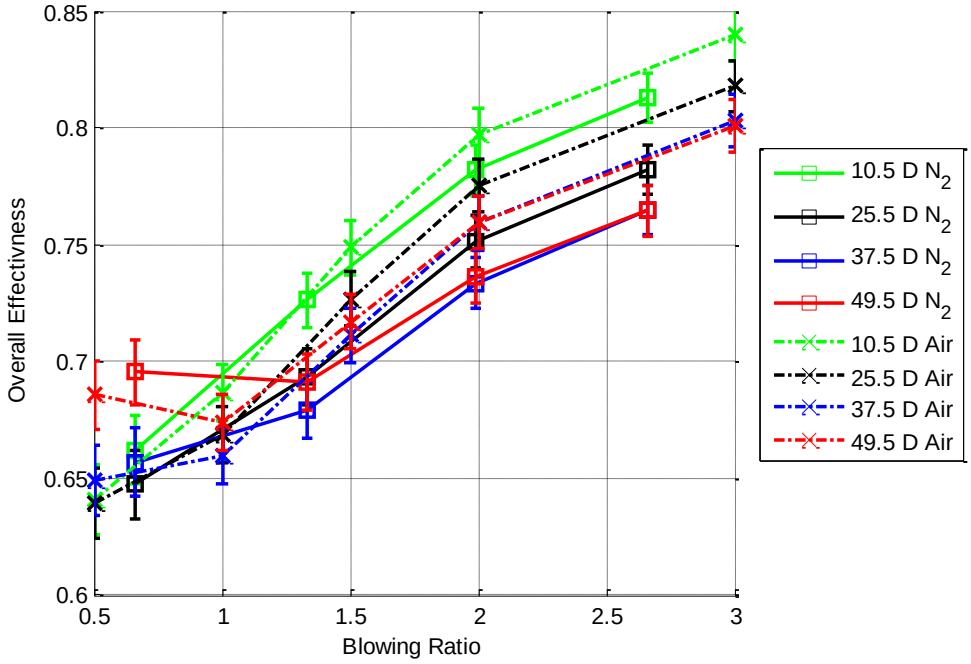

Figure 4-5: Overall effectiveness versus blowing ratio for air and nitrogen coolant

4.3.2 Flame Images

To gain a better understanding of the extent of the reactive film at different blowing ratios, visual images were acquired with a Nikon D5100 Digital SLR camera viewing through the side quartz window. The camera settings were 2 second shutter time, ISO 100, and f/16 aperture. The long shutter time averages out any unsteady effects, and the small aperture setting was used to maintain contrast in the image. The images were assembled into a single image, then post processed together using Microsoft Office Picture Manager where the colors were enhanced by setting the red hue to -100, and the saturation level to +50. Black lines marking the thermocouple locations were added for reference.

Figure 4-6 shows one of the resulting flame images taken for a Φ = 1.3. For reference, internal geometry of the test plate assembly has been overlaid on the image. The thermocouple locations have been identified as well. The IR camera viewing window spans from approximately the 10.5 *D* to 49.5 *D* locations. The images were also used to determine the flame length. However, what is the flame length? The flame does not suddenly end, but rather slowly fades away with the colors changing from blue, to green, to yellow to the orange of the background. Where the flame color is blue corresponds to where the reaction is most intense, and also is the easiest to distinguish when it ends, so it served as the most convenient color to use for the flame length. Using this method, flame start and end locations can be identified as they are in Figure 4-6. The locations were determined where the blue RGB values decreased below 130.

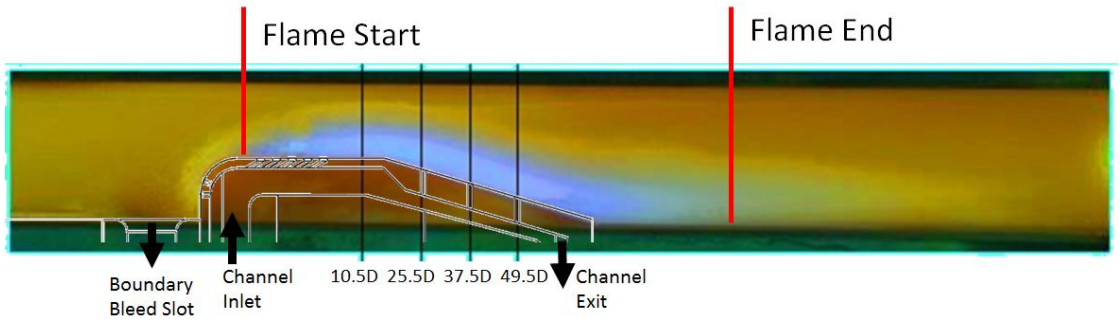

Figure 4-6: *M* = 1 flame image with the flame start and end locations marked.

Figure 4-7 shows the resulting flame images for the reactive film study with Φ = 1.3 at multiple blowing ratios. The *M* = 0 image shows no detectable flame as expected since there was no oxygen rich coolant for the fuel rich mainstream to react with. *M* = 0.5 produced a small flame that remains focused over the test plate and quenches shortly after the trailing edge of the test plate. The IR images of the test plate, shown on the right side of Figure 4-8, indicated the peak surface temperature occurred between 25.5 *D* and 37.5

D downstream which corresponds with where the blue core of the flame starts to fade to a green hue. There is a lack of flame in the showerhead region for $M = 0.5$. Furthermore, the flame starts at the location of the first trench. This suggests that there is insufficient coolant driving pressure at this low mass flow for the coolant to overcome the stagnating pressure on the leading edge of the plate. It is also possible that ingestion was occurring through the showerhead holes at this $M = 0.5$ case.

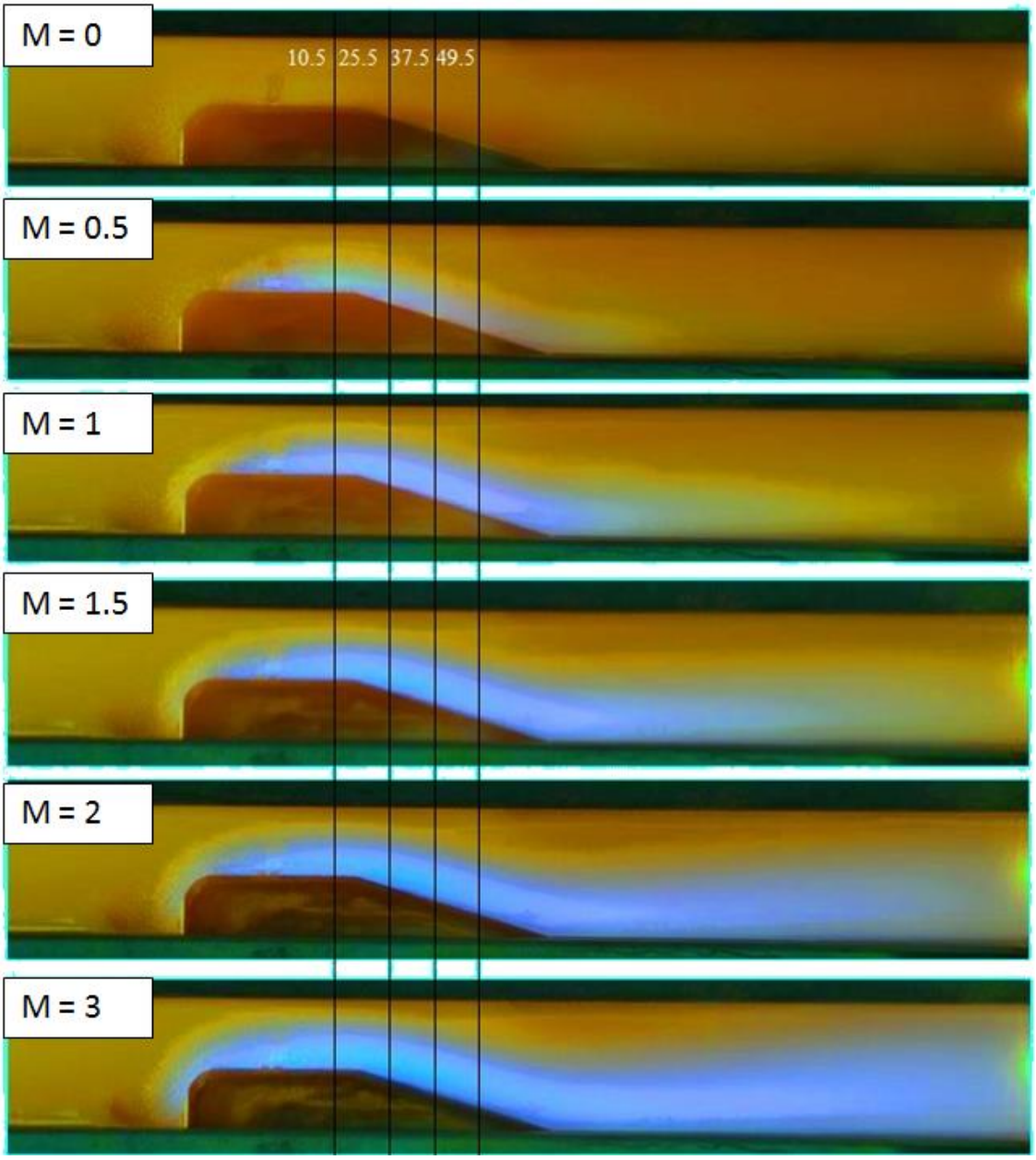

Figure 4-7: Enhanced flame images for the reactive film cooling cases

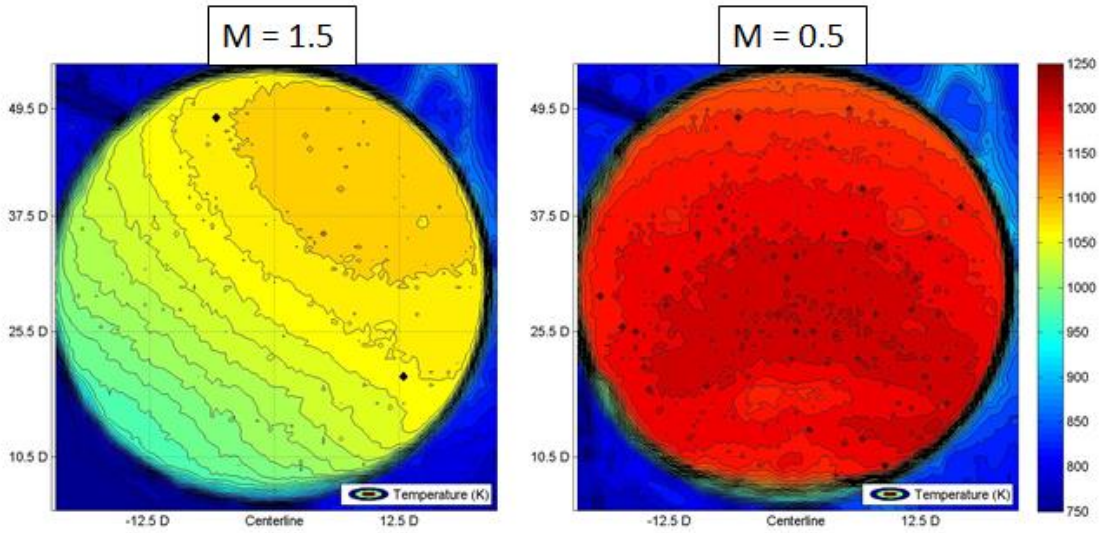

Figure 4-8: Comparison of high and low blowing ratio surface temperature

The flame appears to remain well attached to the surface of the test plate at all blowing ratios. This indicates the coolant is remaining well attached, even with the 16 degree turning angle along the trailing edge of the plate. M = 1 produced a longer flame and some interaction over the leading edge of the plate can be seen. M = 1.5 has a flame which extends almost a chord length past the trailing edge of the plate, this means the reaction is much more spread out and helps lessen the heat load to the plate as seen on the left side of Figure 4-8. The is a left to right variance shown in the IR image for the M = 1.5 case indicative of the leading edge cooling having some effect downstream versus the symmetric profile of the M = 0.5 case. By M = 2, the flame was more than two chord lengths long. Also, clearly visible flame was seen over the leading edge of the plate indicating the showerhead coolant is reacting shortly after exiting the holes. By M = 3, the flame extended past the end of the image and had grown very thick, encompassing almost the entire flow passage over the test plate. This long flame is concerning in actual engine applications as there would be an additional cascade of airfoils located inside this

trailing flame sheet. Thus, the leading edge of those downstream blades would be exposed to a flame.

These flame images may also provide a way to quickly estimate the *Da* number of the flow. Recall from Equation 2-16 that *Da* is a ratio of the flow time to the chemical time. The flow time can be characterized as the time required for the freestream to pass over the length of the test plate. The chemical time is the time required for the reaction to complete, and can be characterized as the time required for the freestream to move the length of the flame. Thus, *Da* can be expressed using Equation 4-2 as a ratio of the test plate length of the flame length.

$$Da = \frac{\tau_{flow}}{\tau_{chem}} = \frac{\frac{L_{test\ plate}}{U_\infty}}{\frac{L_{flame}}{U_\infty}} = \frac{L_{test\ plate}}{L_{flame}} \qquad \text{Equation 4-2}$$

As discussed at the beginning of this section, the flame length was determined to be the streamwise distance from the start of the blue flame to its end.

Table 4-5 shows the estimated *Da* values versus blowing ratio based on the flame images using the method described above. As described by Kirk *et al.* [23], longer flames correspond to lower *Da* numbers. For $Da > 1$, the reaction would be concentrated over the plate as is seen for the $M = 0.5$ flame image. This is also apparent in the thermocouple measurements in Table 4-2 and the IR image in Figure 4-8 which showed an increase in surface temperature of almost 100 K versus the $M = 0$ case. $Da < 1$ results in long flames where the heat release is distributed over a large area.

Table 4-5: *Da* versus blowing ratio based on the flame images

M	***Da***
0.5	1.3
1.0	0.8
1.5	0.5
2.0	0.4
3.0	< 0.4

4.3.3 Heat Flux Measurements

One of the goals of the third objective was to compare the performance of reactive and non-reactive film layers. This was accomplished by using air as a coolant for two different freestream conditions; Φ = 0.8 for non-reactive film, and Φ = 1.3 for reactive film. The difference in average freestream temperature for these tests was small at 1460 K for the Φ = 1.3, and 1430 K for Φ = 0.8. Figure 4-9 shows heat flux measurements for four downstream locations at multiple blowing ratios at equivalence ratios of 1.3 (right) and 0.8 (left). The heat flux was initially calculated using Fourier's Law provided in Equation 3-1. The tick mark label "high h" represents an increase in the internal coolant equal to $M = 0.5$. The actual blowing ratio was held constant between "0.5" and "0.5 high h" as discussed at the beginning of Chapter 4. Thus, $M = 0.5$ high h had the same amount of total coolant flow as $M = 1$ as can be seen in Table 4-1. This allowed the effectiveness of internal heat transfer coefficient to be compared with the increase in blowing ratio.

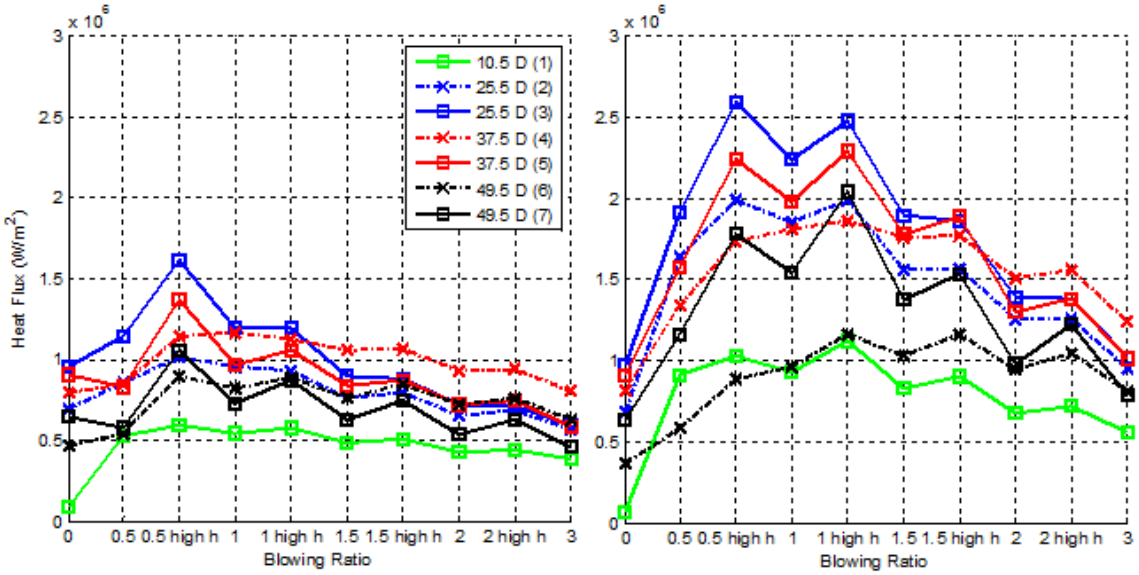

Figure 4-9: Heat flux vs blowing ratio for each thermocouple location for non-reactive (Φ = 0.8, left) and reactive film (Φ = 1.3, right)

The reactive film cooling on the right resulted in almost twice the heat flux through the plate as the non-reactive film cooling shown on the left. While the trend between reactive and non-reactive film were similar to those reported by Lynch *et al.* [25] and Shewhart [26], the absolute heat flux values were higher. It would be expected that a thin wall with a "cold" driving fluid temperature on the backside would result in higher values due to a reduced thermal resistance to heat flux. The heat flux generally decreases with blowing ratio, and a higher internal *h* has the effect of increasing the heat flux at each blowing ratio. This was due to a reduction of the average internal channel temperature from the increased mass flow as well as a potentially increased internal *h*. The heat flux values also approach each other with increasing *M*. This is indicative of the five rows of trench's ability to create a layer of coolant underneath the flame, thus buffering the wall from the elevated driving temperature. This is consistent with the results Lynch *et al.* [25] and Shewhart [26].

The showerhead holes eject coolant toward the odd thermocouple pair side. This is the left hand side of test section as shown previously in Figure 3-16 or Figure 4-2. However, the heat flux is generally higher for the odd side versus the even side for Φ = 1.3 as shown in Table 4-6. Figure 4-10 shows the surface temperature acquired by the IR camera for M = 1 with both low Φ and high Φ mainstream. Since the surface temperature is lower on the left than the right, a lower heat flux would be expected assuming relatively uniform spanwise internal channel temperature. There is a larger than expected variance for the backside wall temperature leading to the varied heat flux measurements. This is most evident with the higher equivalence ratio temperatures where the difference between the odd and even backside temperatures is several times the difference in surface temperature for the same downstream distance.

Table 4-6: Temperatures and heat fluxes for each location at M = 1.

	Φ = 0.8			**Φ = 1.3**		
Location	**T_s (K)**	**T_b (K)**	**q" (W/m^2)**	**T_s (K)**	**T_b (K)**	**q" (W/m^2)**
1	960	929	544000	1117	1070	925000
2	992	854	959000	1148	901	1850000
3	953	771	1190000	1113	797	2240000
4	984	811	1170000	1147	906	1810000
5	975	833	966000	1142	875	1980000
6	978	859	819000	1139	1017	961000
7	959	853	727000	1124	918	1540000

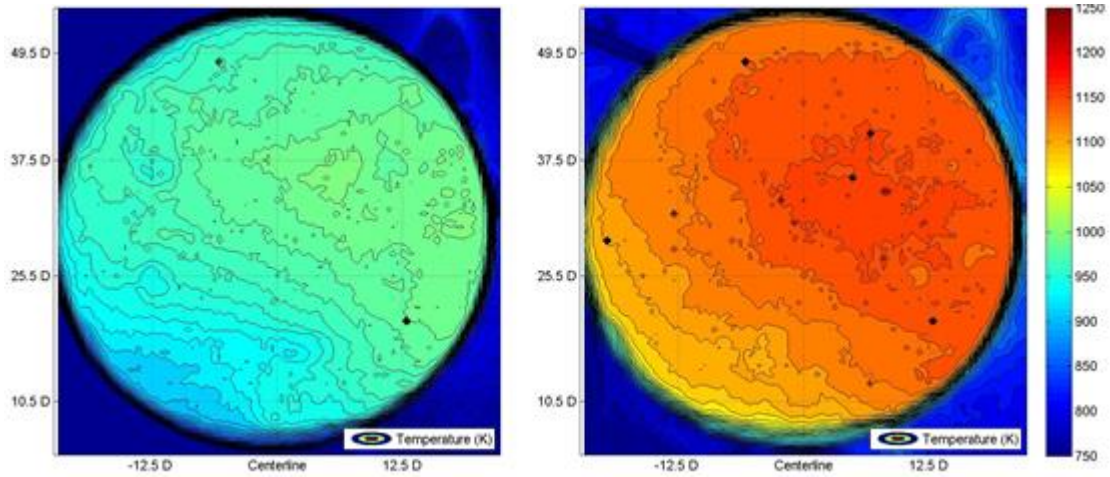

Figure 4-10: IR surface temperature plots for *M* = 1 of non-reactive film (left) and reactive film (right)

The unusual behavior described above of the backside wall temperature raised some concerns regarding the heat flux accuracy. It would be expected to have fairly consistent convective heat transfer coefficients in the internal channel, which are plotted in Figure 4-11 where *h* was calculated from Equation 4-3.

$$h = q''/(T_{backside} - T_c) \qquad \text{Equation 4-3}$$

The value for thermocouple pair 3 was a large negative value due to the measured wall temperature being lower than the internal channel coolant temperature at some blowing ratios. The values for *h* are much higher than typical values for the internal cooling channels of vanes and blades which are usually between 1,000 and 10,000 W/m^{2}K [6]. Also of concern is the general disparity between the two equivalence ratios as the equivalence ratio should have little effect on the internal *h*. There was a good agreement between the two cases for the 10.5 *D* thermocouple pair. Also note that *h* for the 10.5 *D* location varies little with coolant mass flow. Increasing the blowing ratio from 0.5 to 3.0 increases total coolant flow by a factor of six, but *h* only increases about 30 percent.

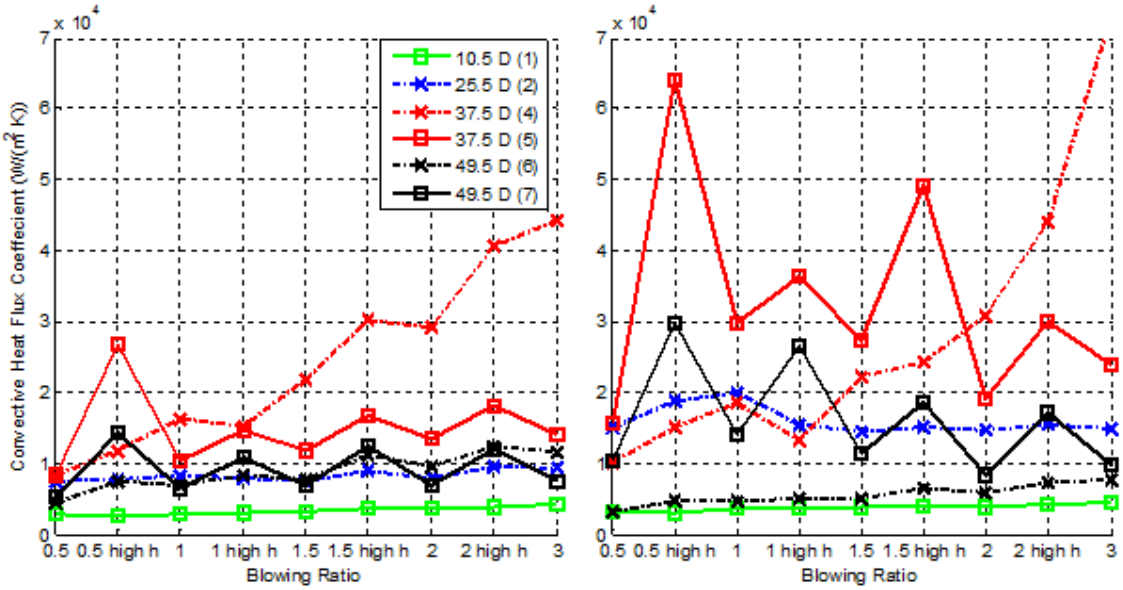

Figure 4-11: Internal channel convective heat transfer coefficient versus blowing ratio. For non-reactive (Φ = 0.8, left) and reactive film (Φ = 1.3, right)

It is suspected the thermocouples intended to read the backside wall temperature of the test plate at Locations 2 through 7 were not actually reading the wall temperature due to not being imbedded in the plate, but rather had their tip pressed against the surface as shown in Figure 4-12. This potentially allows the internal channel coolant to cool the thermocouple down from the wall temperature so that it reads a temperature between the actual wall temperature and the coolant temperature. This would artificially increase the measured temperature difference through the test plate thickness and yield an erroneously high value for heat flux using Fourier's Law. A higher *q"* and lower $T_{backside}$ both increase the calculated internal *h* value.

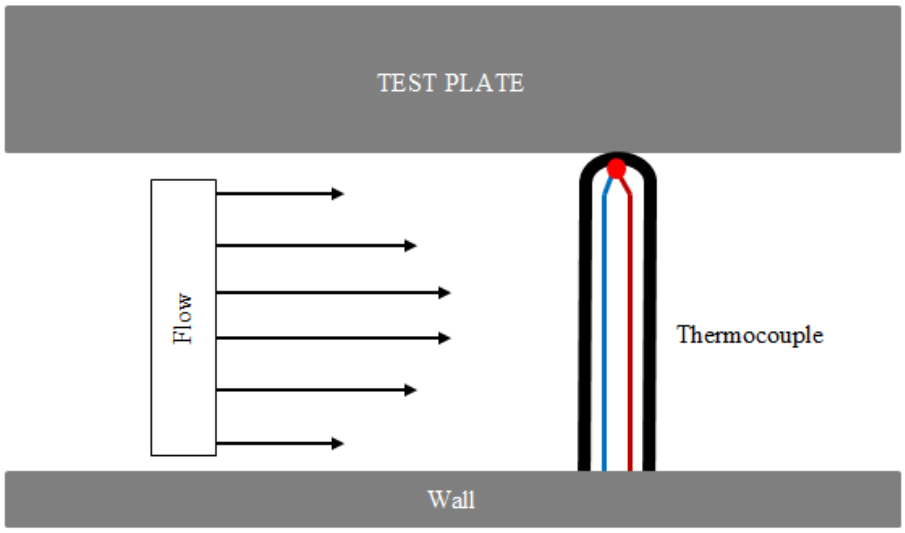

Figure 4-12: Depiction of the backside thermocouple

Unlike the thermocouples at Locations 2 through 7 which were pressed against the surface as depicted in Figure 4-12, the backside thermocouple at Location 1 was strapped to the backside surface with a thin Inconel strap which has been resistance welded across the thermocouple's tip where the bead would be located. In other words, the thermocouple was laid across the surface rather than sitting normal to the surface. This should have held it more tightly to the wall and also protected it from some of the cooling effects of the channel coolant thus increasing the accuracy of its measurements in comparison to the other backside thermocouples.

In an attempt to increase the accuracy of the heat flux calculations at all thermocouple locations, the heat flux was recalculated using a one dimensional series resistive heat transfer circuit as given by Equation 4-1. A generic *h* value was used for all locations and was taken to be the internal channel convective heat transfer coefficient calculated at the 10.5 *D* location for each blowing ratio. The value for *h* at 10.5 *D* was chosen because its values were the most consistent and in agreement with the literature.

Figure 4-13 shows the heat flux versus blowing ratio values using the resistive circuit analogy. It was expected for 10.5 *D* to have the highest heat flux because the wall is only 1.27 mm thick at 10.5 *D* versus 3.175 mm thick at the other locations. A thinner wall reduces the thermal resistance, allowing high heat fluxes. At high blowing ratios, heat flux increases with downstream distance which would indicate a reduction in the effectiveness of the film cooling at protecting the wall either from mixing, the presence of the flame, or both. The trend was reversed at low blowing ratios. This was likely due to an increased internal channel coolant temperature reducing the temperature difference between the surface, and the internal channel. At low blowing ratios, the internal coolant gained 20 to 30 K as it flowed through the channel. This increase in coolant temperature near the tailing edge of the test plate was not accounted for in the heat flux calculations. As the coolant flow rate increased, the coolant temperature dropped as shown in Table 4-7. Above a blowing ratio of 1, the coolant had to be heated with an inline heater to keep its temperature in the channel above 730 K and was constant within a few degrees down the length of the channel.

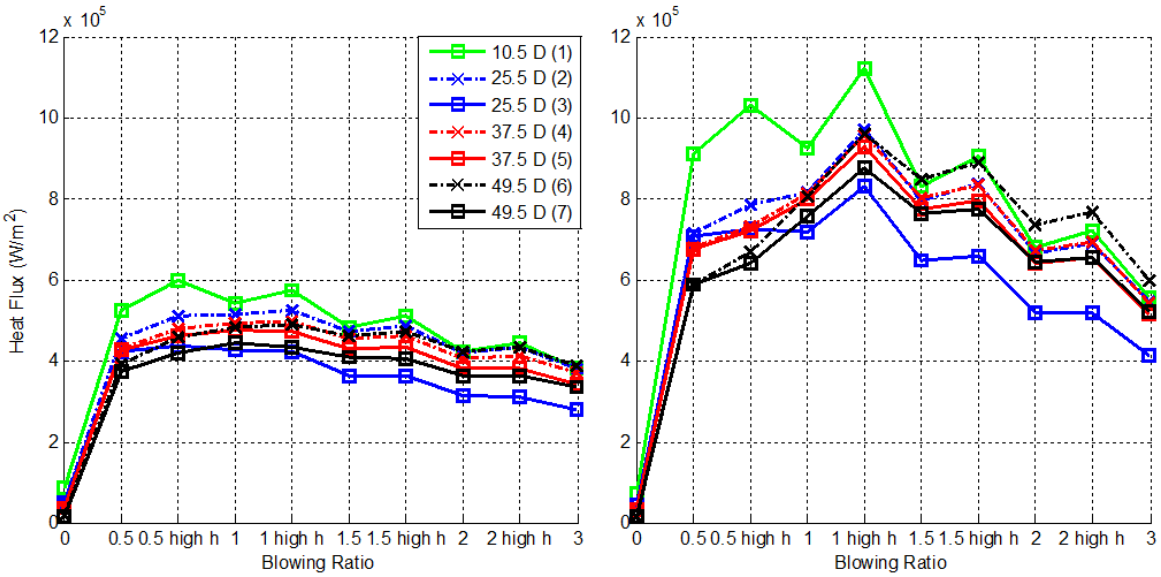

Figure 4-13: Heat flux versus blowing ratio for non-reactive (Φ = 0.8, left) and reactive film (Φ = 1.3, right) calculated using resistive thermal circuit analogy.

Table 4-7: Coolant inlet temperatures at low blowing ratios.

M	T_c (K) Φ = 0.8	T_c (K) Φ = 1.3
0.5	830	892
0.5 high h	752	808
1	739	808
1 high h	731	733

The use of the resistive circuit analogy did well at reducing the variance in the heat flux values that was seen in Figure 4-9. Furthermore, the odd thermocouple side which received additional coolant from the showerhead rows consistently yielded lower heat flux values than the even thermocouple side. The reactive film still produced a 1.5 to 1.8 factor increase in heat flux which was expected given the flame near the wall raising the freestream driving temperature.

4.3.4 Net Heat Flux Reduction

NHFR was one of the desired comparative parameters to evaluating reactive versus non-reactive film cooling. However, as discussed in Section 4.1.2, determining the

appropriate no-film heat flux values is difficult. Since the solid surface test plate required to attain the appropriate measurements for the no-film case was not available for this study, the no-film heat flux values used in the calculation of *NHFR* were determined using the same methodology described at the conclusion of Section 4.1.2. These are pseudo-no-film heat flux values and are presented here for the enablement of a discussion on comparative *NHFR* values between non-reactive and reactive film. The resulting pseudo no-film cooling heat flux values are plotted in Figure 4-14, where the left graph uses the channel conditions from the non-reactive film set, and the right graph uses the channel conditions from the reactive film set. Both graphs use the surface temperatures from the internal cooling only data set.

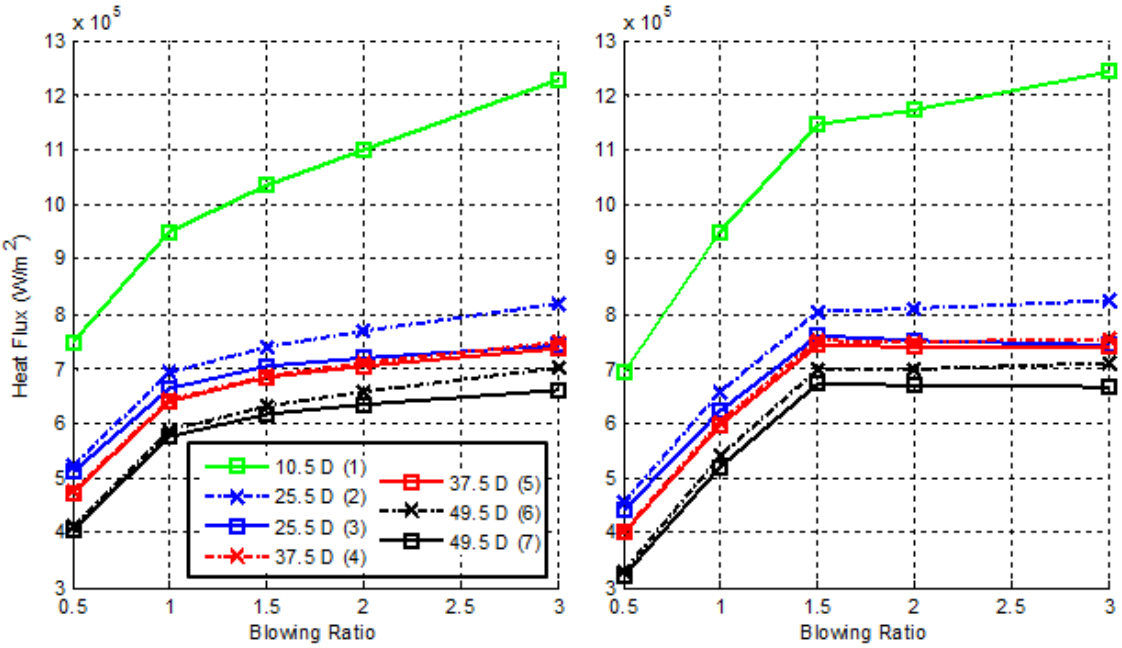

Figure 4-14: Pseudo no-film cooling heat flux values for non-reactive (Φ = 0.8, left) and reactive film (Φ = 1.3, right)

Using the pseudo no-film cooling heat flux values from Figure 4-14 and the heat flux values from Figure 4-13, NHFR versus blowing ratio was plotted in Figure 4-15. The

non-reactive *NHFR* values are consistently positive and increase with blowing ratio while decreasing with downstream distance. The reactive *NHFR* values likewise increase with blowing ratio and decrease with downstream distance, but due to the additional heat of the flame in the film, the reactive film results in negative *NHFR* values at the lower blowing ratios. These trends are in agreement with those reported by Lynch *et al.* [25] and Shewhart [26]. At *X/D* = 22 for a flat plate with five rows of trenches, they reported non-reactive *NHFR* values between 0.2 and 0.5 for blowing ratios of 0.5 to 3, and reactive *NHFR* values between -0.2 and 0.4 for the same blowing ratio range. Because of the use of pseudo-no-film heat flux instead of the actual no-film heat flux, a direct comparison of the results in Figure 4-15 to their results is not possible. There was also the added effect of the curvature, the showerhead rows, and a different boundary layer development due to the boundary layer bleed that existed in this study that was not present in their flat plate studies.

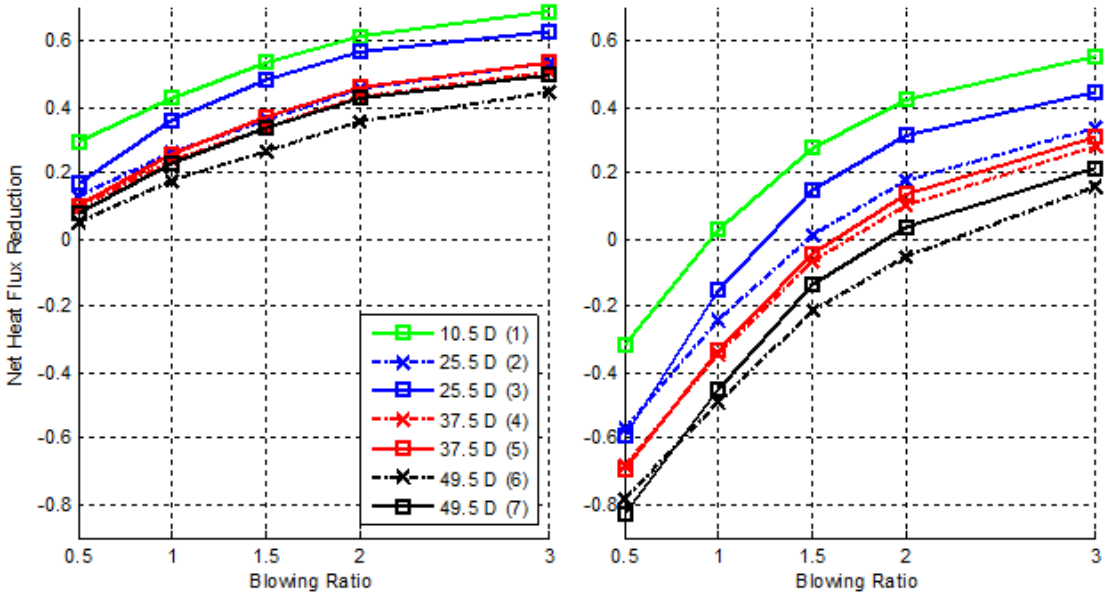

Figure 4-15: *NHFR* versus blowing ratio for non-reactive (Φ = 0.8, left) and reactive film (Φ = 1.3, right).

While the *NHFR* results presented here can be justifiably questioned due to method used for determine the no-film heat flux values, they can still provide the comparative analysis desired for non-reactive versus reactive film cooling for the third objective. The use of coolant in a reactive environment may have a detrimental effect on the blade. The negative *NHFR* values seen especially at the low blowing ratios indicate the heat flux to the airfoil was increased with the addition of coolant. While heat flux and surface temperature are related, the ultimate goal of film cooling is to reduce the surface temperature, not the heat flux. The addition of a flame adjacent to the airfoil surface may be the cause of the increased heat flux, while the surface temperature was still reduced. For this reason, an examination of the surface temperature and overall effectiveness is warranted to gain a more complete picture of the benefit or determent of the film cooling.

4.3.5 Overall Effectiveness and Surface Temperature Measurements

Overall effectiveness was the second comparative parameter of the third objective. Overall effectiveness is calculated using Equation 2-4. T_∞ was estimated to be the average the FCR inlet and outlet temperatures as the test plate was located approximately midway between the two locations. T_c was again measured in the internal coolant channel between the showerhead rows and the trenches. Figure 4-16 shows the overall effectiveness for the "5 Trench + 2 Shower" test plate. Again, reactive results were obtained using air coolant with the WSR operating at an equivalence ratio of 1.3. The non-reactive results were obtained using air coolant with the WSR operating at an equivalence ratio of 0.8. T_∞ was approximately 1430 K for the Φ = 0.8 cases, and 1460 K for the Φ = 1.3 cases.

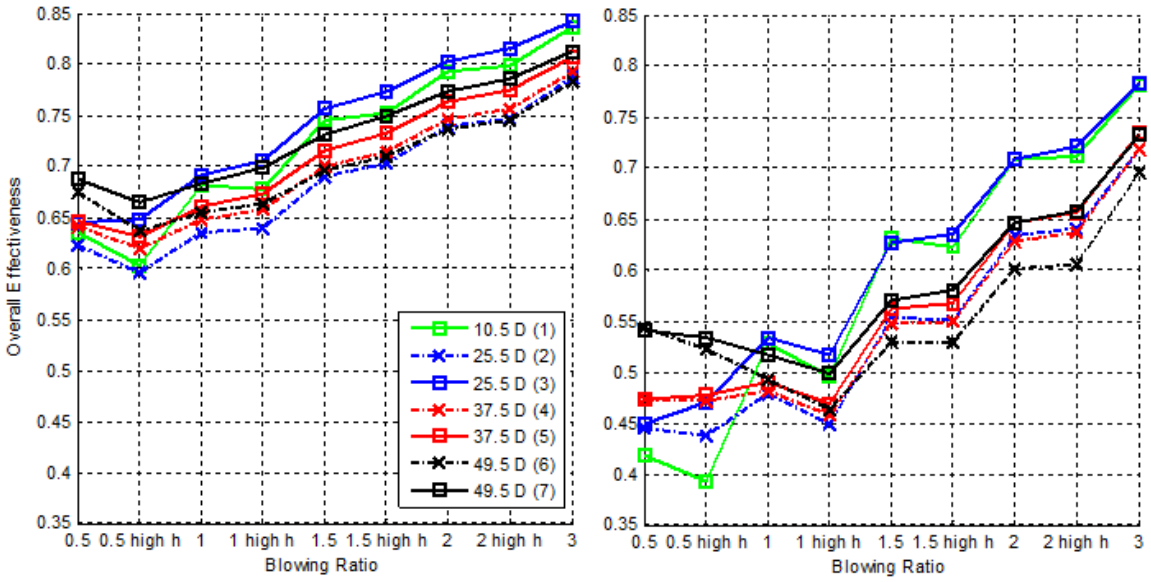

Figure 4-16: Overall effectiveness versus blowing ratio for non-reactive (Φ = 0.8, left) and reactive film (Φ = 1.3, right)

Examining Figure 4-16 shows the non-reactive film consistently outperforms the reactive film cooling as it did in the NHFR plots. The performance generally increases with blowing ratio, and the difference in effectiveness between reactive and non-reactive cooling decreases with increasing blowing ratio. The reduction in effectiveness between M = 0.5 and M = 0.5 "high h" was a result of the reduction in coolant temperature from the higher coolant flow without a sufficient concurrent reduction in the surface temperature as shown in Figure 4-17 with similar results at M = 1 for the reactive case. Above M = 1, the coolant temperature was maintained between 730 K and 740 K for all cases. Unlike the heat flux measurements, the overall effectiveness increased with the "high h" case at the higher blowing ratios. This means the additional internal coolant was lowering the surface temperature despite the increased heat flux. Between M = 1 and M = 1.5 seems to be a critical range in which the performance of the reactive film increases

significantly. This was probably when the coolant supply is sufficient to maintain a non-reactive buffer between the flame and the wall.

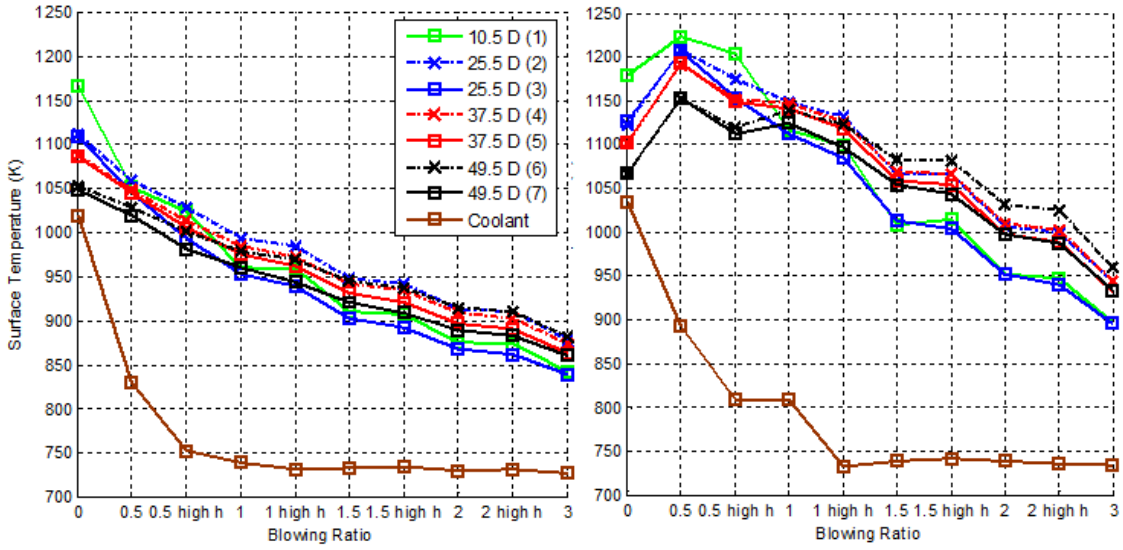

Figure 4-17: Measured surface and coolant temperatures versus blowing ratio for non-reactive (Φ = 0.8, left) and reactive film (Φ = 1.3, right).

Figure 4-17 further highlights a result seen with the *NHFR* values in Figure 4-15. *NHFR* values at low blowing ratios with reactive film suggested the film had a detremental effect on the blade. This result is confirmed with the surface temperature measurements displayed in Figure 4-17. The reactive film provides a reduction in surface temperature near the holes, that progresses downstream as the blowing ratio increases. Figure 4-18 displays a plot of the surface temperature recorded for M = 1 reactive film, subtracted from the surfaced temperatuer recorded for M = 0. This provides an example of an initial benefit of the film cooling that fades as the downstream distance increases.

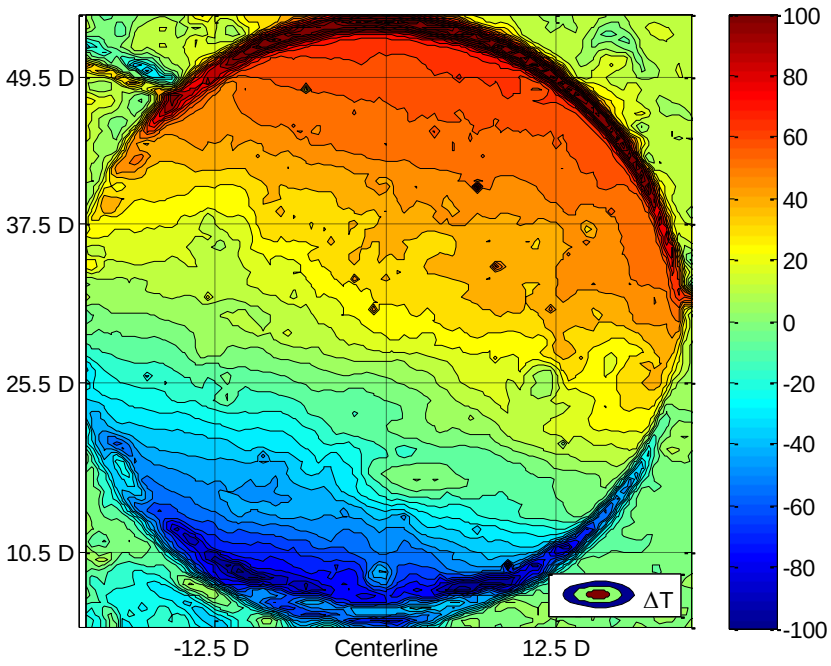

Figure 4-18: Change in surface temperature as a result of the film for M = 1 versus M = 0.

Figure 4-19 shows results obtained using the IR camera. The first four IR images have been processed to show the surface temperature of the test plate for the no cooling case and a blowing ratio of 0.5 for both non-reactive cooling on the left, and reactive cooling on the right. With no cooling, the temperature is slightly higher for the high mainstream equivalence ratio due to T_∞ being about 30 K higher than the low equivalence ratio flow. However, the temperature profiles are similar in magnitude and shape. When M = 0.5, the non-reactive case showed a noticeable decrease in surface temperature over the M = 0 case. The reactive cooling case showed a large increase in surface temperature over the M = 0 case. The film formed a flame over the test plate heating the surface. The final row of images shows the IR images processed to display overall effectiveness. As seen previously in Figure 4-16, the overall effectiveness of the

reactive case was significantly lower than the non-reactive case due to the higher surface temperature.

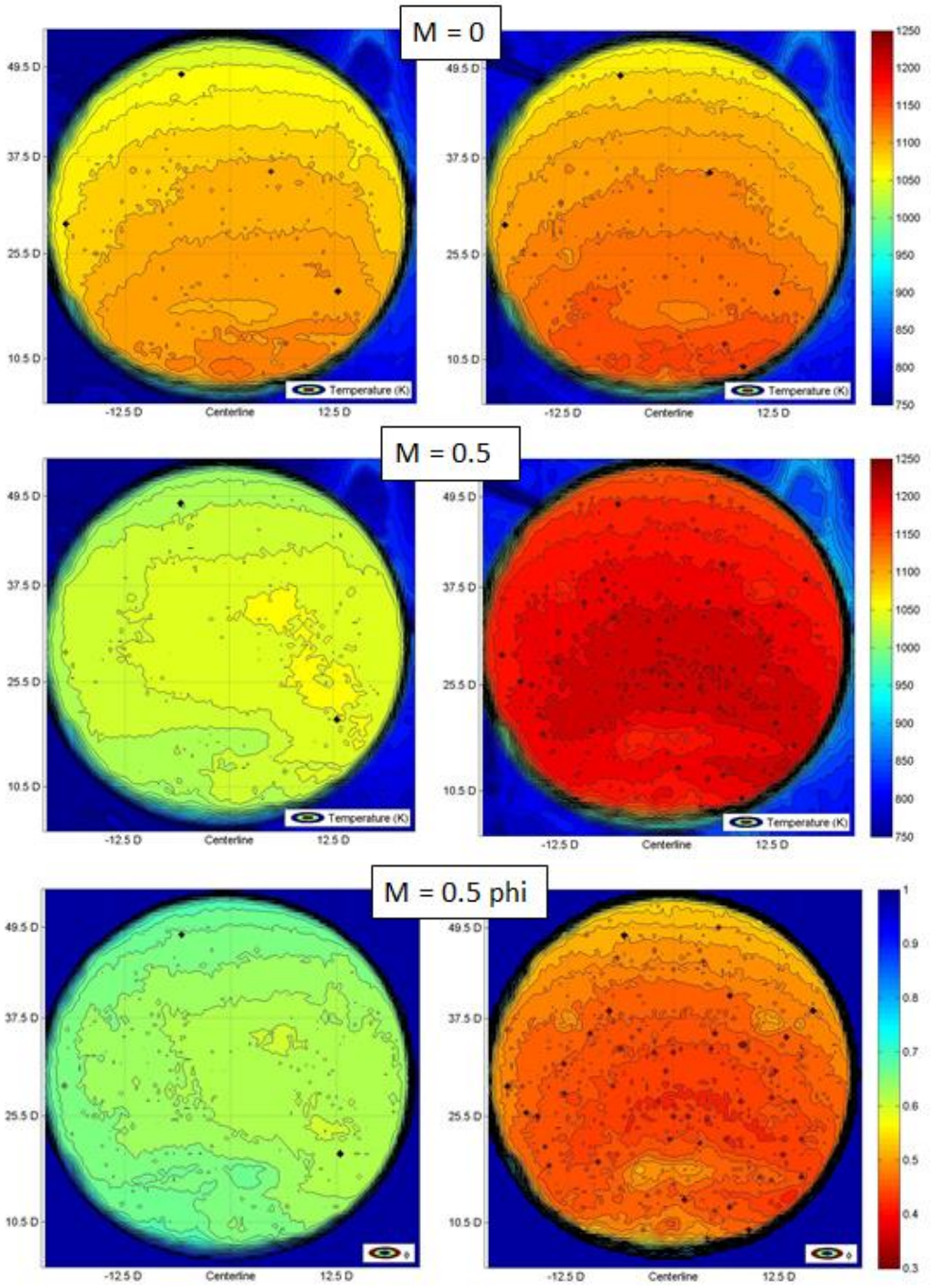

Figure 4-19: IR surface temperature measurement for non-reactive cooling (left) and reactive cooling (right) and M = 0 and M = 0.5, and ϕ for M = 0.5

A helpful method to compare the overall effectiveness between reacting and non-reacting film is to calculate the difference between the two cases ($\Delta\phi$). This is a different $\Delta\phi$ than described by Rutledge *et al.* [11]. Their value described the difference between an internal cooling only case, and a film cooling case, thus gaining the benefit of the film. The value presented here is a reduction in the overall effectiveness resulting from the presence of the flame and is given by Equation 4-4.

$$\Delta\phi = \phi_{non-reacting} - \phi_{reacting} \qquad \text{Equation 4-4}$$

Using this $\Delta\phi$ comparison with the IR images, a plot such as the one shown in Figure 4-20 for M = 0.5 can be generated. It shows a large decrease in overall effectiveness near the lower portion of the image where the flame was very intense. The reduction in ϕ decreases with downstream distance as the flame dies out as seen in the flame image in Figure 4-7. This trend can be seen in Figure 4-21 which displays the pitchwise averaged $\Delta\phi$ versus downstream distance for -12 D and +12 D spanwise locations. A pitchwise average is the average between the centers of two holes, or the hole pitch. The average reduction in overall effectiveness for the area from 10.5 D to 49.5 D in the streamwise direction, and -12 D to +12 D in the spanwise direction was 0.18.

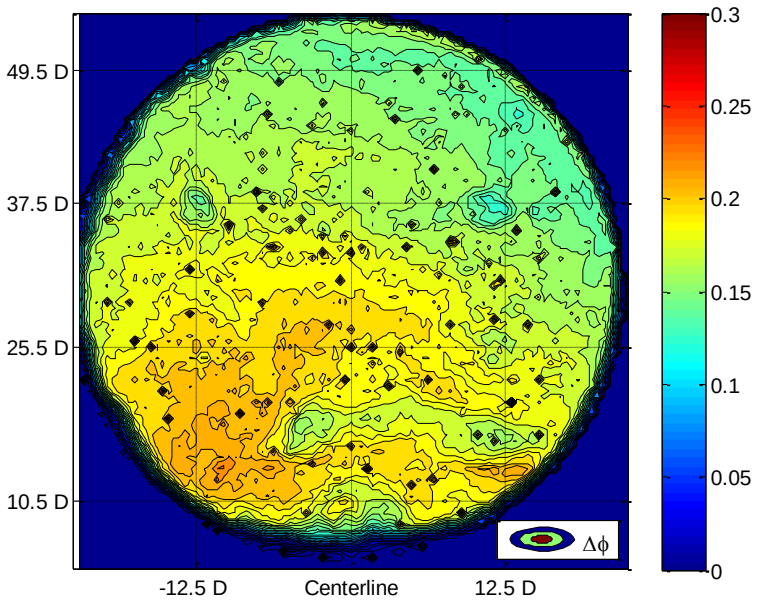

Figure 4-20: $\Delta\phi$ for M = 0.5.

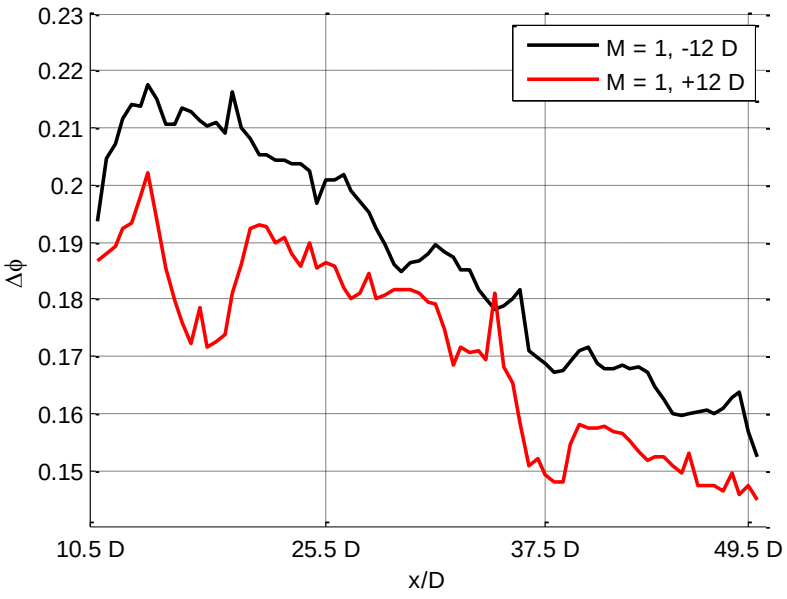

Figure 4-21: Pitchwise averaged $\Delta\phi$ versus downstream distance for -12 D and +12 D spanwise location for M = 1.

Figure 4-22 shows the processed IR images for M = 1. The reactive case shows a reduction in surface temperature and an increase in ϕ over the M = 0.5 case. However, the performance does not match the non-reactive film, and the surface temperatures of the

reactive case are not lower than the $M = 0$ case. Thus, because of the flame in the film, the film is not always providing benefit to the plate as was seen in Figure 4-18. A trend that is starting to become more noticeable is the left to right variance in both surface temperature and ϕ. This was from the coolant of the showerhead rows, which was blowing towards the left side of the images, providing additional cooling on that side of the test plate. However, the $\Delta\phi$ plot for $M = 1$ shown in Figure 4-23 displays a symmetry along the centerline of the test plate indicating the flame is also symmetric and its shape is not affected by the showerhead cooling. Unlike the $\Delta\phi$ plot for $M = 0.5$ in Figure 4-20, the reduction in ϕ is consistent with downstream distance. Both of these trends can be seen in Figure 4-24 which displays the pitchwise averaged $\Delta\phi$ for two different spanwise locations. A pitchwise average is the average between the centers of two holes, or the hole pitch. This even streamwise reduction of the overall effectiveness resulted from the flame extended past the end of the airfoil section as seen in Figure 4-7. The average $\Delta\phi$ for $M = 1$ was 0.18.

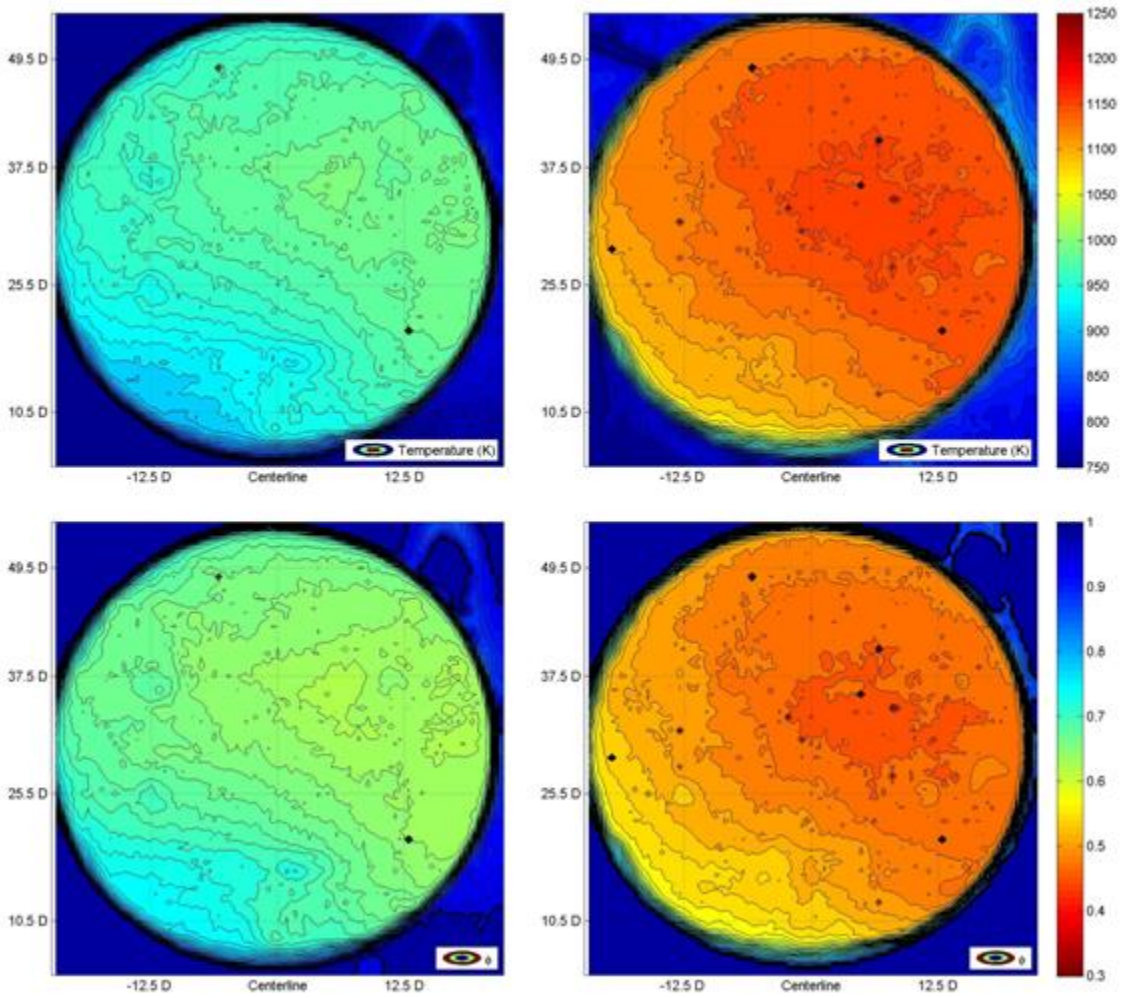

Figure 4-22: ϕ (bottom) and surface temperature (top) for M = 1 with non-reactive (left) and reactive (right) cooling

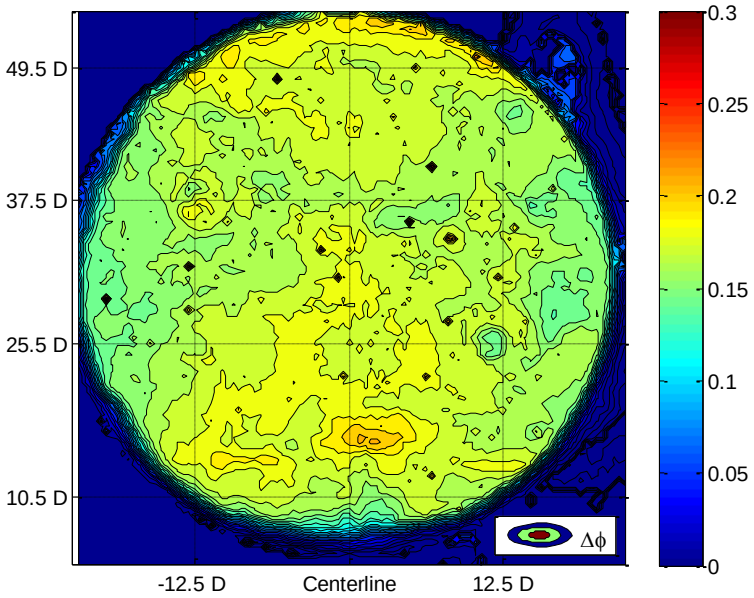

Figure 4-23: $\Delta\phi$ for M = 1

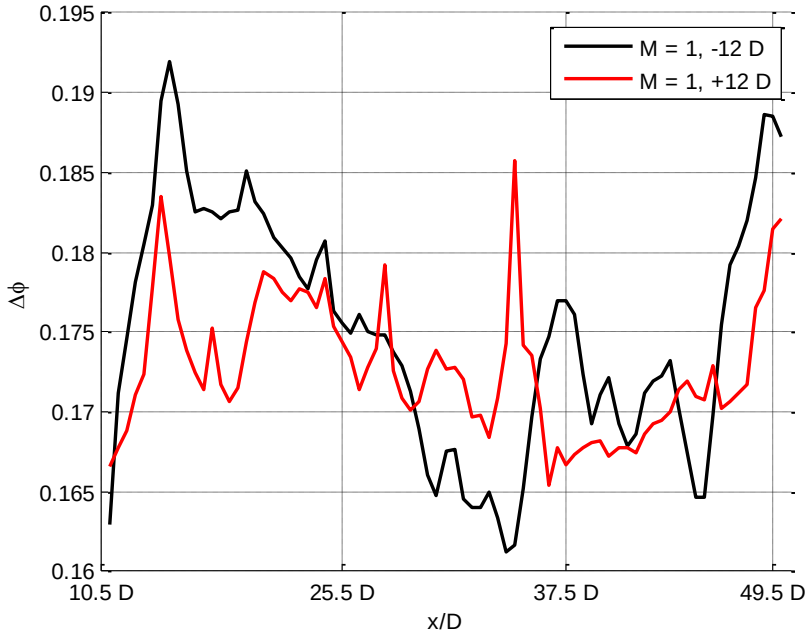

Figure 4-24: Pitchwise averaged $\Delta\phi$ versus downstream distance for -12 D and +12 D spanwise location for M = 1.

Figure 4-25 shows the processed IR images for M = 2. The non-reactive cooling provided excellent protection for the wall with the temperature in the bottom left of the

image close to the coolant temperature which is 729 K. The cooling was providing a reduction to the wall temperature even with a reactive film layer. Some of the thermocouples are visible in the images. This was from the welded material on the thermocouples having a slightly different emissivity and being raised slightly above the surface of the plate. Figure 4-26 shows the reactive versus non-reactive $\Delta\phi$ for M = 2.0. Contrary to the individual non-reactive or reactive film cooling plots of ϕ where there was a gradient moving from left to right in the image, the $\Delta\phi$ plot shows symmetry between the left and right sides. This indicates the heating from the flame is fairly uniform across the span of the test plate and the reduction in overall effectiveness seen with the reactive film versus the non-reactive film is a result of an increase in the driving freestream temperature from the flame. This close symmetry between the left and right sides can be seen in Figure 4-27. As the film is able provide a sufficient amount of coolant to buffer the reaction away from the surface, the average $\Delta\phi$ has been reduced to 0.14.

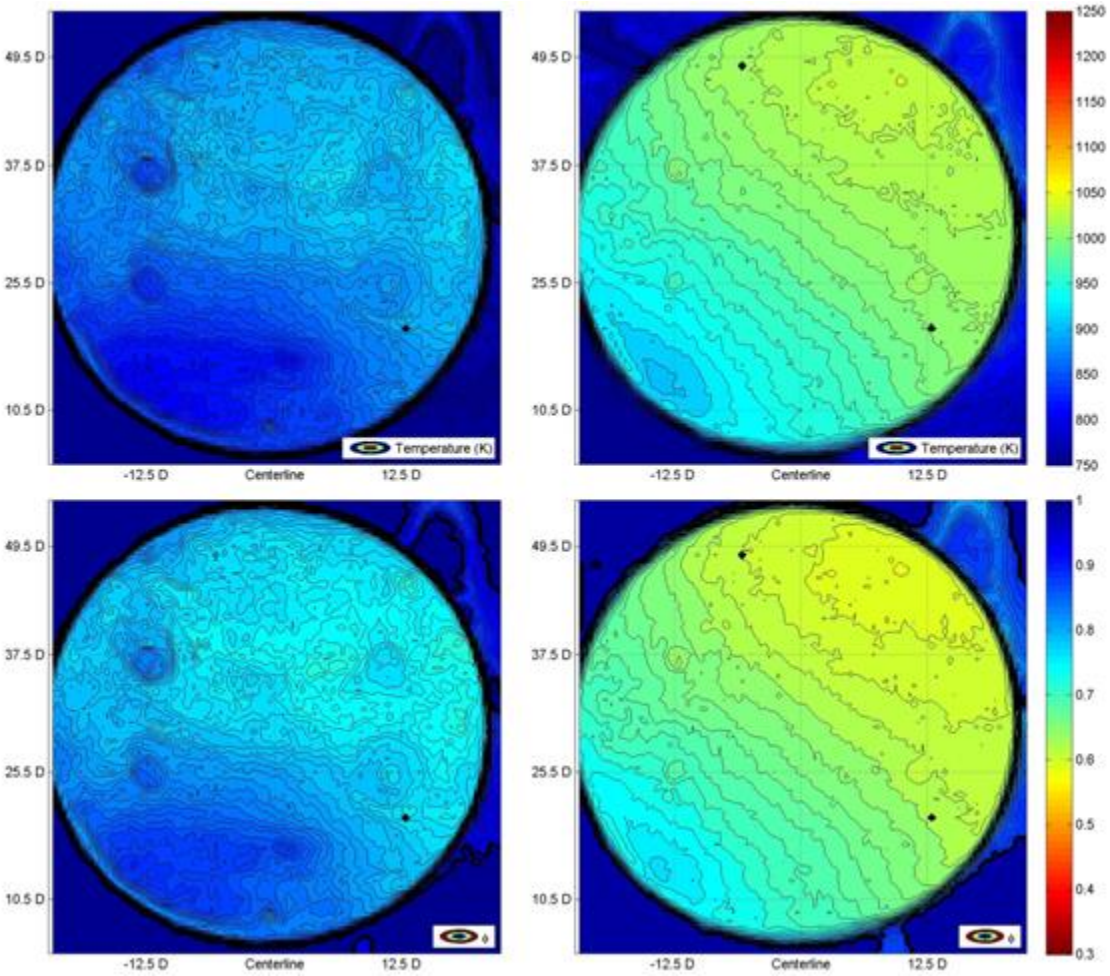

Figure 4-25: ϕ (bottom) and surface temperature (top) for M = 2 with non-reactive (left) and reactive (right) cooling

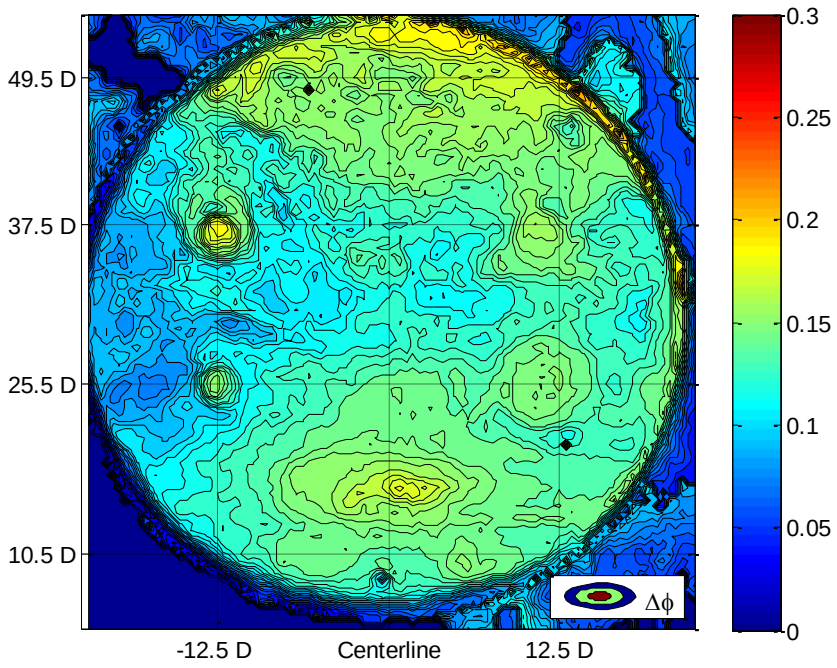

Figure 4-26: $\Delta\phi$ for M = 2.0

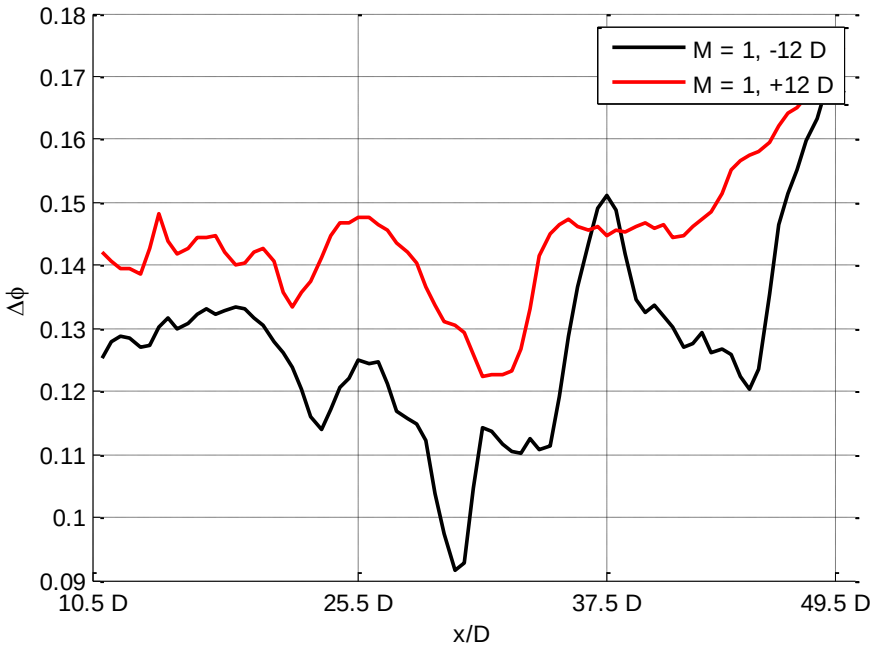

Figure 4-27: Pitchwise averaged $\Delta\phi$ versus downstream distance for -12 D and +12 D spanwise location for M = 2.

For a different view on the left to right effect the showerhead holes are having on the surface temperature downstream Figure 4-28 shows a comparison of the surface temperature taken from the IR images between the left (-12 *D*) and right (+12 *D*) of the IR image. The difference decreased with downstream distance as the effect of the showerhead rows is washed out by the trenches. The difference is more pronounced for the higher blowing ratio indicating the blowing from the showerhead holes was fairly week for the $M = 1$ case. This would agree with the flame images in Figure 4-7 where at $M = 0.5$ there was no evidence that film was ejected from the showerhead holes, and at $M = 1$ there was a weak flame around the leading edge of the plate. However, by $M = 2$ the flame at the leading edge of the plate became more pronounced.

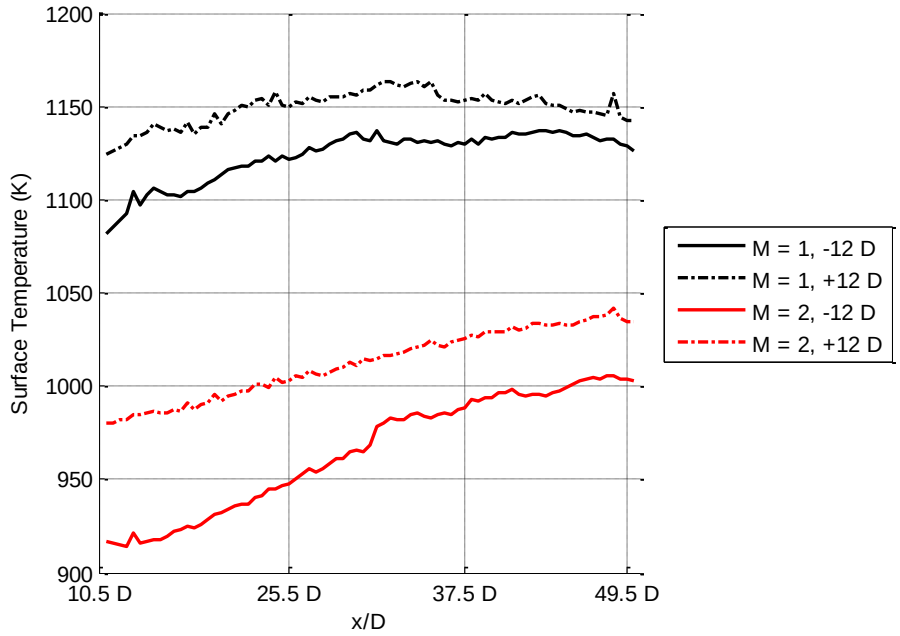

Figure 4-28: Left (-12 *D*) to right (+12 *D*) comparison of surface temperature versus downstream distance for two blowing ratios.

Figure 4-29 shows the processed IR images for $M = 3$. At this high blowing ratio, the non-reactive film provides excellent protection to the plate keeping almost the entire

examined area close to the coolant temperature of 727 K. Furthermore, the left to right variance has been reduced as the symmetric cooling of the trenches dominates the film layer. Also, the coolant remained well attached to the surface initially, even at this high blowing ratio, but it may have separated slightly moving over the tapered trailing end of the test plate as indicated by a sudden decrease in overall effectiveness. The reactive cooling still has the gradient from bottom left to top right. The performance is higher than it was at $M = 2$, but it is not as uniform as the non-cooling case.

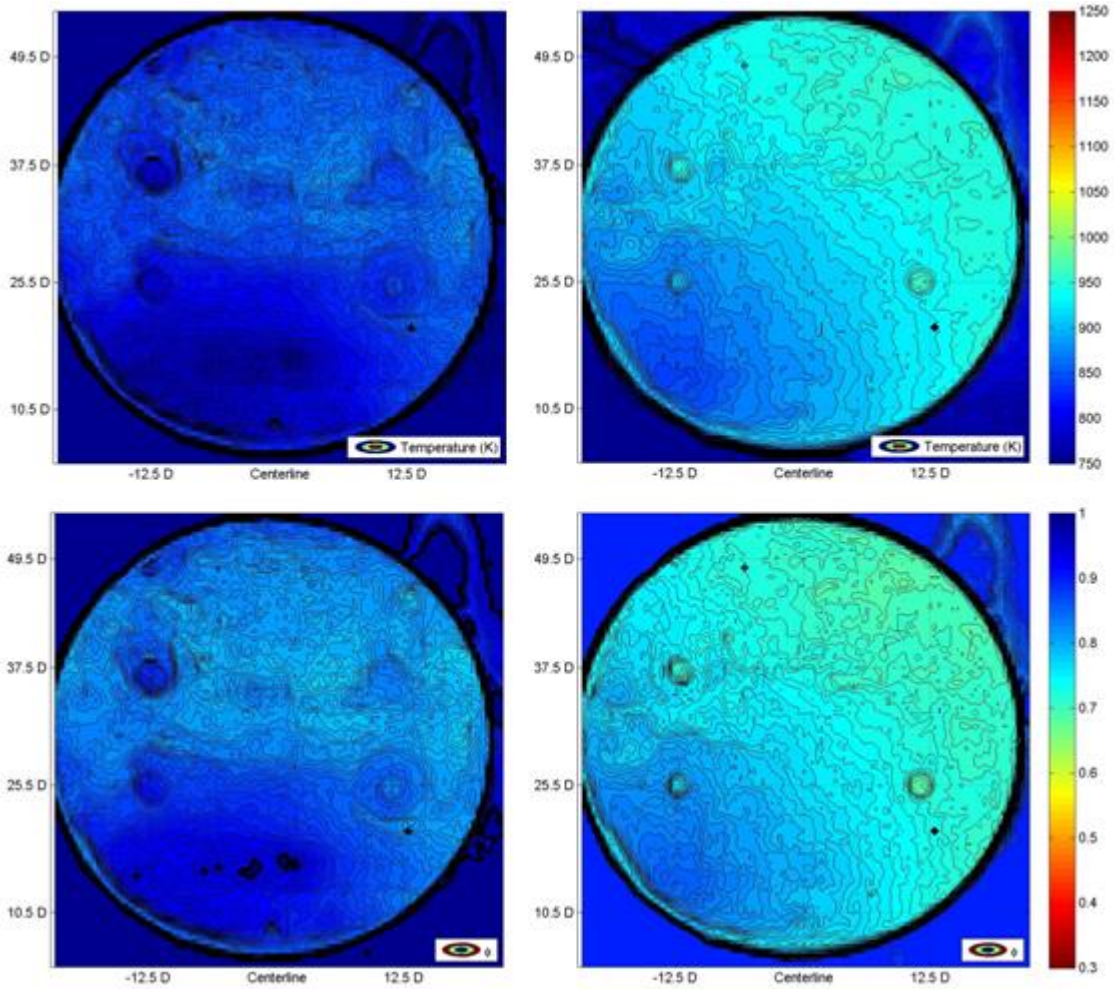

Figure 4-29: ϕ (bottom) and surface temperature (top) for $M = 3$ with non-reactive (left) and reactive (right) cooling

Figure 4-30 shows the $\Delta\phi$ plot for M = 3. Unlike the the $\Delta\phi$ plots for the lower blowing ratios which displayed a symmetry about the centerline, Figure 4-30 shows a large reduction in $\Delta\phi$ between 25.5 D and 37.5 D on the left side of the image. Reviewing the ϕ plots from Figure 4-29, the apparent seperatation of the film occurred in this same region for the non-reactive case with the sudden reduction in overall effectiveness where as the reactive case did not show the sudden reduction. This large drop in $\Delta\phi$ is evident in Figure 4-31. The average $\Delta\phi$ had been reduced to 0.09 with the high level of film cooling flow.

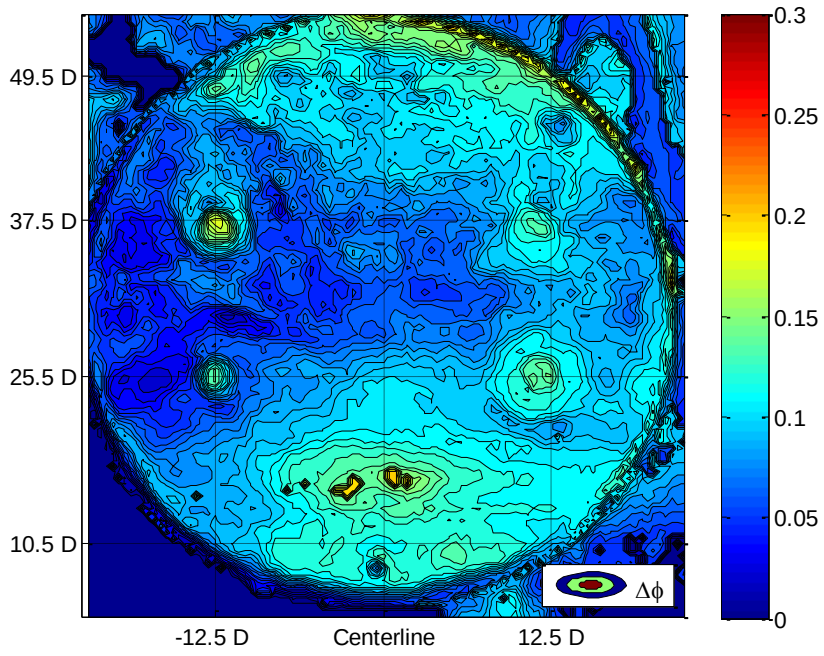

Figure 4-30: $\Delta\phi$ plot for M = 3

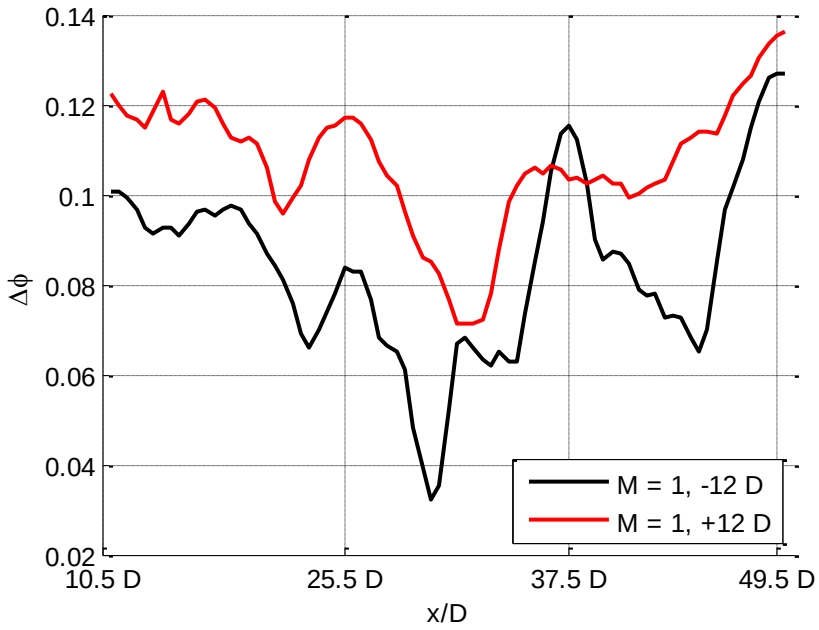

Figure 4-31: Figure 4-32: Pitchwise averaged $\Delta\phi$ versus downstream distance for -12 *D* and +12 *D* spanwise location for *M* = 2.

This section completes the goals of objective three to develop techiniques for comparing various film cooling conditions. Several parameters may be used for this comparison, most notably NHFR and overall effectiveness. However, additional parameters which are useful for such comparisons are $\Delta\phi$, which can compare the overall effectiveness of different blowing ratios, reacting or non-reacting films, or film cooling to no-film cooling if the internal condition of the test plate is matched.

5. Conclusions and Recommendations

5.1 Summary of Findings

This study consisted of three primary objectives. The first objective was to finish the design and construct a test rig capable of testing reactive and non-reactive film cooling schemes over a surface with curvature at multiple Mach numbers with an engine representative temperature. The second objective was to develop the methods to analyzing the two parameters of interest for this study: net heat flux reduction, and overall effectiveness. The third objective was to apply these parameters for the comparative analysis between reactive and non-reactive film. These objectives were fully accomplished.

A new film cooling test rig and well-stirred reactor were constructed to study reactive and non-reactive film cooling schemes at multiple Mach numbers and with surface curvature at engine representative temperatures to fulfill the first objective. The test channel flow was supplied using a propane/air well-stirred reactor capable of providing fuel rich or fuel lean air at temperatures in excess of 1600 K. The film cooling rig was a module design allowing for a test plate to be quickly and easily replaced between studies. The channel height could be adjusted to allow variation in the mainstream Mach number.

To achieve the second objective a combination of thermocouples and an infrared camera were utilized. Net heat flux reduction is the comparison of heat flux with film cooling versus the heat flux of the test article without film cooling. Using surface thermocouples on each side of the test plate, the heat flux for each test condition was acquired. A no-film cooling heat flux was also needed where the internal coolant channel temperature must be matched to the coorsponding film cooling case. Overall

effectiveness was acquired by measuring the external surface temperature with either the thermocouples or the IR camera. The coolant temperature was measured with thermocouples placed inside the internal cooling channel. Finally, the freestream temperature was measured at the rig inlet and exit and a linear interpolation was used to determine the approximate freestream temperature over the airfoil section.

There were some challenges with acquiring net heat flux reduction. The acquisition of this parameter was difficult for two reasons. First, there is uncertainty in the accuracy of the heat flux measurements in general due to the method the temperature of the backside wall of the test plate is acquired. However, some of the inconsistencies of the heat flux values were removed by using a resistive heat flux circuit analogy to re-calculate the heat flux values using the coolant temperature and the convective heat transfer coefficient from a thermocouple pair was mounted more ruggedly to the test plate. The second problem encountered with obtaining net heat flux reduction measurements was determining a method to acquire the appropriate no film cooling heat flux values for the comparison. Through an investigation of heat flux measurements using internal cooling only, nominally without any film, the importance of the backside condition came to light. The backside condition of the heat flux gauge, in this case the test plate, must match between the film cooling case and the no film cooling case. In this case, the coolant channel temperature must be consistent between the no-film cooling and the film cooling cases.

The second parameter of interest was overall effectiveness which is the non-dimensionalization of the test plate surface temperature with the freestream temperature and the film coolant temperature. The heat transfer properties of the test plate are

important to make comparisons between laboratory studies and actual engines components. The most important parameter is the Biot number of the test plate or blade wall. By using a test plate of similar material and size to actual engine components, the Biot number is closely matched at $Bi = 0.5$. Furthermore, internal coolant was routed through an internal coolant channel of the test plate to provide cooling to the backside of the test plate. Due to matching cooling conditions and the Biot number to actual engine components, the overall effectiveness measurements obtained closely matched published results. The non-reactive cooling outperformed the reacting film cooling, but as with net heat flux reduction, the performance gap narrowed with increasing blowing ratio. Furthermore, IR surface temperature imaging allowed for detailed surface overall effectiveness maps to be generated for each cooling scheme allowing for the interaction of the coolant to be better understood.

To achieve the third objective, a comparison of nitrogen to air coolant for a non-reactive film cooling was made, and comparisons between reactive and non-reactive film layers. These comparisons were done on a plate with five rows of holes in trench with two rows of cylindrical showerhead holes. To make the comparisons, net heat flux reduction, overall effectiveness, and the change in overall effectiveness were used.

The nitrogen to air coolant comparison was done with a freestream equivalence ratio of 0.8. This ensured the oxygenated air cooling would not have combustible species available to react with. Overall, the two coolant gases performed similarly. The air showed slightly better performance, although this is attributed to an increased internal flow of the air cases over the nitrogen cases. The close performance of the two coolant gases allows for nitrogen to be used as a non-reactive coolant in studies where it is

desired to compare reactive and non-reactive films without changing the freestream fuel content.

The reactive versus non-reactive film comparisons were made using freestream equivalence ratio of 1.3 for the reactive film cases, and a freestream equivalence ratio of 0.8 for the non-reactive cases. Both net heat flux reduction and overall effectiveness showed a better film performance with the non-reactive film. At low blowing ratios, the reactive film produced a net heating of the plate over a no-film condition. The showerhead rows were seen to have an effect at cooling the side they were blowing to for both the reactive and non-reactive cases. Examination of the change in overall effectiveness between reactive and non-reactive cases removed the left to right variance showing the flame sheet resulting from the reactive film was heating the plate evenly. Images of the flame showed for the high blowing ratios where the film is providing a benefit to the airfoil, the flame sheet extends over half a chord length past the tip which would allow it to impact the leading edge of the next cascade of airfoils in an actual turbine.

5.2 Future Work

First, the acquisition of the backside surface temperature needs to be improved to provide more accurate measurements. The best method to accomplish this would be to strap the tip of the thermocouples down to the surface using thin metal bands. This would ensure the thermocouple is in contact with the surface and the metal band would help shield it from the cooling effects of the internal channel coolant.

Second, with the methods now developed to obtain and analyze film cooling data at elevated temperatures, a larger test matrix should be executed to quantify the

performance of various cooling schemes with changes in Mach number and blowing ratio over a surface with curvature. The first cooling scheme that should be tested is a solid surface test plate to obtain the appropriate no-film heat flux and overall effectiveness values. Additional cooling schemes which should be tested include one row, three rows, and five rows of cylindrical holes to examine the building up of film cooling rows. Also the five rows of cylindrical holes would provide a baseline comparison for the holes in trench configuration. An examination of the leading edge section of the plate with reactive film cooling should also be conducted with IR imaging to determine the stagnation location on the leading edge and the heating effect on the leading edge of the reacting film.

Third, the test rig is highly configurable and able to be operated at a variety of temperatures. Experimental verification of the important scaling parameters outlined by Greiner *et al.* [199] and Rutledge and Polanka [19] could now be accomplished between low temperature studies and engine representative temperatures with this facility.

Appendix A

Starting the WSR:

1) Turn on switch damper switch for running the UCC
2) Turn on Fan 2 and Fan 1B
3) Flip switch to DAQ tower on.
4) Turn on the lower propane vaporizer in the tank farm and allow it 30 minutes to warm up, continue with startup procedure while it warms up
5) Turn on both control boxes in back of DAQ tower and press the output button on each
6) Load the "WSR/FCR Rig Control" Labview program, select the file to save the data to, and press "RUN"
7) Turn on air to the 3/4 inch and the 3/8 inch line. Turn the 3/4 inch line slowly and wait for the regulator to fully close before opening the valve completely.
8) In Labview, turn the 3/4 inch line flow up to 400 SLPM (7.4 %)
9) Turn on the wall heater and set to 17.5 % power
10) Turn on the Mokon water coolant supply
11) Turn on the Mokon and heat to 300 F
12) Turn on the WSR water coolant and set both flow rates to 0.1 GPM
13) Wait for the air line temperature to reach between 410 and 450F and the Jet Ring temperature to exceed 375 K. Adjust wall heater if necessary.
14) Turn on both propane tanks connected to the lower vaporizer and open the ball valve between the tanks and the vaporizer
15) Open the ethylene bottle

16) Open the ethylene valves in the lab to provide Ethylene to the flow box
17) Open the propane line valve with the black handle, make sure the valve after the Brooks propane mass flow controller is pointed towards the WSR
18) Turn on the ignitor air flow (25 SLPM)
19) Turn on the ignitor
20) Turn on the ignitor ethylene flow (3.5 SLPM)
21) Turn on the propane to 13.2 SLPM (phi = 0.8)
22) After ignition, turn off the ignitor, ignitor ethylene, and ignitor air
23) Turn the WSR coolant water up to 0.35 GPM for the bottom, and 0.45 GPM for the top
24) Turn on the boundary layer bleed vacuum pump
25) Allow the rig 10-20 minutes to warm up.
26) When increasing propane flow, make small 1-2 SLPM adjustments to prevent large overshoots which could result in unstable WSR performance.
27) If testing at high fuel/air ratios, it is recommended to increase the ratio above stoichiometric at 400 SLPM of air to prevent overheating the WSR
28) Alternate increasing propane and air until 600 SLPM (11.1 %) of air is achieved

<u>Turning off the WSR</u>

1) Set propane flow to “0”
2) Turn air up to 12 %
3) It is helpful to run some film coolant flow to cool the FCR
4) Set both WSR water coolant lines to 0.3 GPM
5) Turn the Mokon temperature down to 100 F

6) Set the wall air line heater to 0 % and turn it off
7) Shut the propane and ethylene tank valves
8) Wait for the rig to cool.
9) Once the air temperature is below 150 F and the jet ring temperature is below 330 K, bleed the ethylene line
10) Turn the propane flow up to 10.0 SLPM while keeping the air flow at 12 %
11) Once the propane line is bled, close the valve between the propane tanks and the vaporizer
12) Turn off the propane vaporizer
13) Turn off the Mokon system.
14) Close the air supply valves
15) Turn off the exhaust fans and turn the UCC damper control off
16) Turn off equipment
17) Empty water trap
18) Run the vacuum pump for 10 to 15 minutes to remove any possible condensation from its cylinders.

Appendix B

Calibration of the mass flow controllers

In order to reduce and quantify uncertainty, all of the mass flow controllers were calibrated prior to the start of the experimental phase. Calibration readings for mass flows from 5 to 500 SLPM were obtained from a Bios Definer 1020 made by DryCal Technology. For the calibration, the mass flow controllers were connected to a dry compressed air supply. The calibration unit was connected in series downstream from the mass flow controller. Mass flow readings were recorded for set point from 5 to 100 percent of the flow rate. The set points were staggered between increase flow rates and decreasing flow rates to ensure the controllers did not exhibit a history bias. Each set point had 3 calibration flow measurements taken with the average entered as the reported value.

Once all of the flow measurement had been recorded for a given mass flow controller, typically 10 to 20 measurement points for each, the actual flow rate was plotted versus the set point. A linear regression trend line was fit to the graph using Excel. If the y-axis intercept was not within 0.25 of 0, the zero dashpot on the mass flow controller was adjusted until the changed in the actual flow reading from the calibration unit matched the discrepancy. A correction for the slope was achieved by adjusting the gas correction factor in the control box. For example, if the slope was approximately 0.98, the gas correction factor was adjusted from 1.00 to 0.98. After the corrections were made, the measurement sweep was repeated with the measurements and set points plotted and a linear fit trend line applied. If the equation for the trend line was approximately $y = x$, the

calibration was complete. Figure A-0-1 shows an initial measurements of one of the mass flow controllers, and Figure A-0-2 shows the calibrated results.

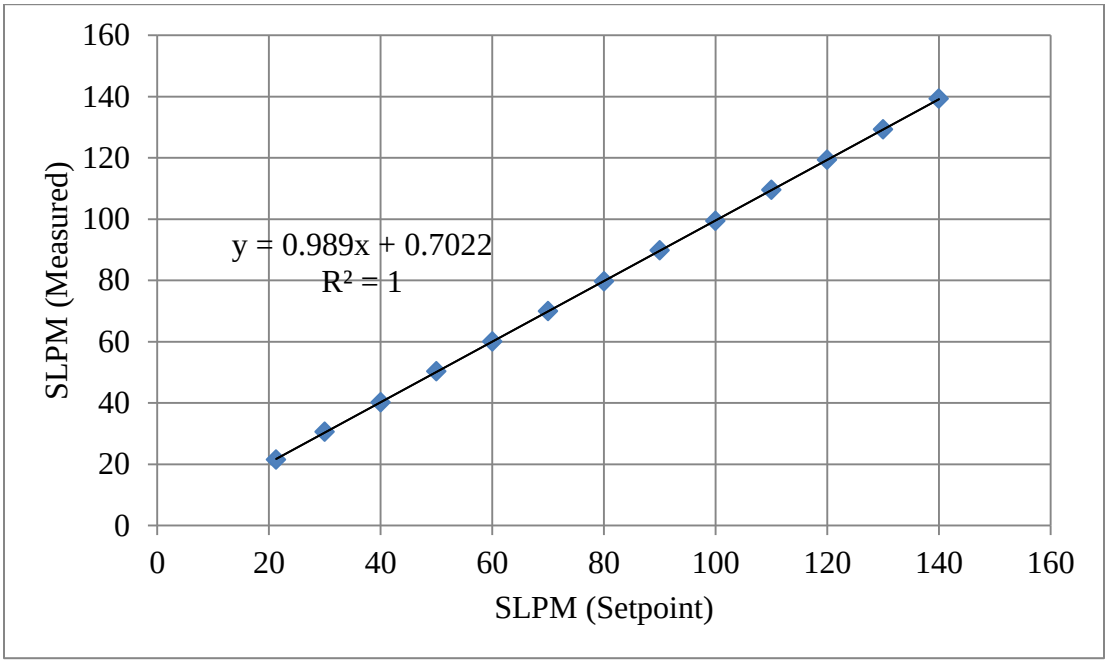

Figure A-0-1: Initial measurements for one of the mass flow controllers

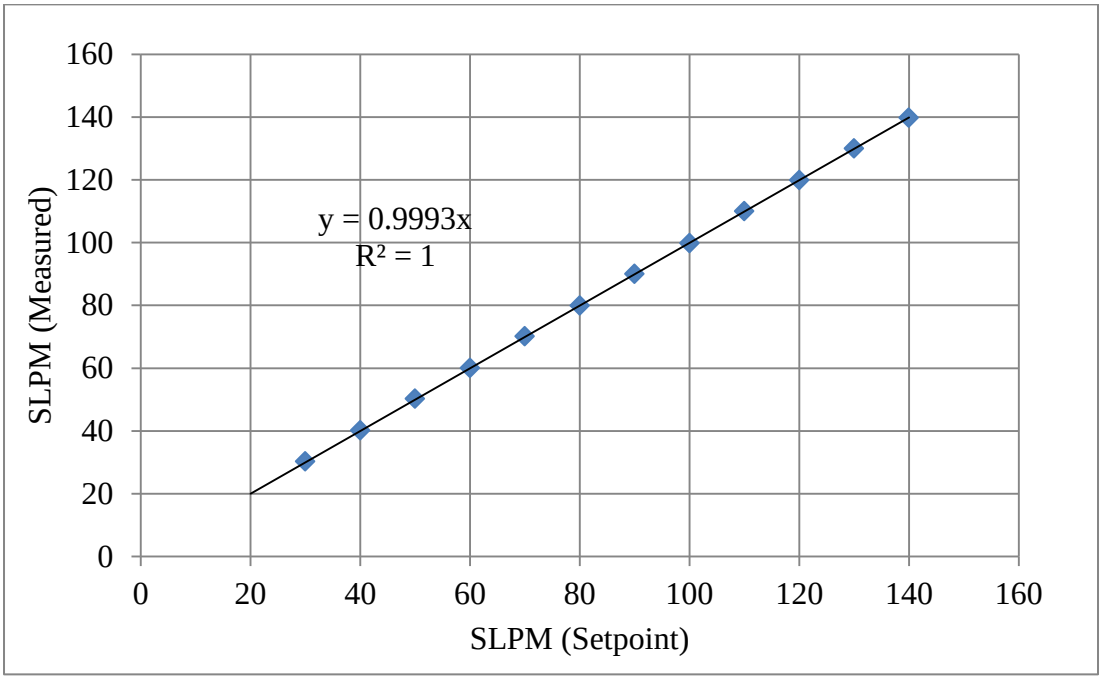

Figure A-0-2: Calibrated measurements for one of the mass flow controllers.

Bibliography

1 Bogard, *D*.G., and K. A. Thole. "Gas Turbine Film Cooling." *Journal of Propulsion and Power,* Vol 22, No 2, April, 2006: 249-270.

2 Dittmar, J., Schulz, A., and Wittig, S., "Assessment of Various Film-Cooling Configurations Including Shaped and Compound Angle Holes Based on Large-Scale Experiments." *Journal of Turbomachinery,* 2003: 57-64.

3 Incropera, F. P., Dewitt, *D*.P., Bergman, T. L., and Lavine, A. S., "Introduction to Convention." In *Fundamentals of Heat and Mass Transfer*, Hoboken, NJ: John Wiley & Sons, Inc, 2007: 347-385.

4 Mattingly, J. *D*., Heiser, W. H., and Pratt, *D*.T., *Aircraft Engine Design.* Reston, Virginia: American Institute of Aeronautics and Astronautics, Inc., 2002.

5 Kays, W. *M*. and Crawford, *M*. E., *Convective Heat and Mass Transfer*. McGraw-Hill Inc., 380-388.

6 Davidson, T. F., Kistenmacher, *D*. A., and Bogard, *D*. G., "Film Cooling with a Thermal Barrier Coating: Round Holes, Craters and Trenches." *ASME Turbo Expo.* Copenhagen, Denmark: ASME, 2012.

7 Eberly, *M*. K., Thole, K. A., "Time-Resolved Film-Cooling Flows at High and Low Density Ratios." *ASME Turbo Expo.* San Antonio, TX: ASME, 2013.

8 Harrington, *M*. H., WcWaters, *M*. A., Bogard, *D*. G., Lemmon, C. A., and Thole, K. A., "Full-Coverage Film Cooling with Short Normal Injection Holes." *Journal of Turbomachinery,* 2001: 798-805.

9 Greiner, N. J., Polanka, *M*. *D*., and Rutledge, J. L. "Scaling of Film Cooling Performance From Ambient to Engine Temperatures." *ASME Turbo Expo.* Dusseldolf, Germany: ASME, 2014.

10 Lawson, S. A., Straub, *D*. L., Casleton, K. H., and Sidwell, T., "Direct Measurements of Overall Effectiveness and Heat Flux on a Film Cooled Test Article at High Temperatures and Pressures." *ASME Turbo Expo 2013.* San Antonio, Texas: ASME, 2013. 1-12.

11 Rutledge, J. L., Polanka, *M*. *D*., and Bogard, *D*. G., "The Delta Phi Method of Evaluating Overall Film Cooling Performance." *ASME Turbo Expo GT 2015-43288.* Montreal, Canada: ASME, 2015.

12 Han, J., Dutta, S., and Ekkad, S., *Gas Turbine Heat Transfer and Cooling Technology*. Boca Raton, Florida: CRC Press, 2012.

13 Smith, *D*.E, Bubb, J. V., Popp, O., Grabowski III, H., Diller, T.E., Schetz, J. A., and Ng, W. F. "An Invertigation of Heat Transfer in a Film Cooled Transonic Turbine Cascade, Part 1: Steady Heat Transfer." *International Gas Turbine & Aeroengine Congress & Exbibition.* Munich, Germany: ASME, 2000.

14 Bunker, R. S. "Film Cooling Effectiveness Due to Discrete Holes Within a Transverse Surface Slot." *ASME Turbo Expo GT-2002-30178.* Amsterdam, The Netherlands: ASME, 2002.

15 Polanka, *M. D.*, Zelina, J., Anderson, W. S., Sekar, B., Evans, *D*. S., Lin, C.-X., and Stouffer, S. *D*. "Heat Release in Turbine Cooling 1: Experimental and Coputational Comparison of Three Geometries." *Journal of Propulsion and Power*, 2011: 257-268.

16 Wang, T., Chintalapati, S., Bunker, R. S., and Lee, C. P., "Jet Mixing in a Slot", *Experimental Thermal and Fluid Sciences*, Vol. 22, 2000: 1-17.

17 Sellers, J. P., "Gaseous Film Cooling with Multiple Injection Stations." *AIAA Journal* Vol. 1, No. 9, 1963: 2154-5156.

18 Andrews, G.E. "Full Coverage Effusion Cooling with a Narrow Duct Backside Coolant Supply." *ASME Turbo Expo GT2012-68629.* Copenhagen, Denmark: ASME, 2012.

19 Rutledge, J. L., and Polanka, *M. D.*, "CFD Evaluation of Uncoventional Film Cooling Scaling Parameters on a Simulated Turbine Blade Leading Edge." *ASME Turbo Expo.* Dusseldorf, Germany: ASME, 2014.

20 Bahr, *D*. W. "Technology for the Design of High Temperature Rise Combustors." *Journal of Propulsion*, Vol 3, No. 2, March-April 1987: 179-186.

21 Johnson, *D. D.*, and Polanka, *M. D.*, "Cooling Requirements for an Ultra-Compact Combustor." *50th AIAA Aerospace Sciences Meeting AIAA 2012-0948.* Nashville, TN: AIAA, 2012.

22 Lukachko, S. P., Kirk, *D*. R., and Waitz, I. A., "Turbine Durability Impacts of High Fuel-Air Ratio Combustors Part 1: Potential for Intra-Turbine Oxidation of Partially Reacted Fuel." *ASME Turbo Expo.* Amsterdam, The Netherlands: ASME, 2002.

23 Kirk, *D*. R., Guenette, G. R., Lukachko, S. P., and Waitz, I. A., "Gas Turbie Engine Durability Ipacts of High Fuel-Air Ratio Combustors Part 2: Near Wall Reaction Effects on Film-Cooled Heat Transfer." *ASME Turbo Expo.* Amsterdam, The Netherlands: ASME, 2002.

24 Bohan, B. T., Blunck, *D*. L., Polanka, *M*. *D*., Kostka, S., Jiang, N., and Stouffer, S. *D*., "Impact of an Upstream Film-Cooling Row on Mitigation of Secondary Combustion in a Fuel Rich Environment." *Turbo 12 1055.*

25 Lynch, A. J., Shewhart, A. T., Greiner, N. J., Polanka, *M*. *D*., and Rutledge, J. L., 2015. "Mitigation of Heat Release from Film Cooling in Fuel Rich Environments." *AIAA SciTech 2015.* Kissammee, FL: AIAA.

26 Shewhart, A. T. *Minimization of the Effects of Secondary Reactions on Turbine Film Cooling in a Fuel Rich Environment.* Master's Thesis, Wright-Patterson AFB, OH: Air Force Institute of Technology, 2014.

27 Schwarz, S. G., Goldstein, R.J., and Eckert, E. R. G., 1991. "The Influence of Curvature on Film Cooling Performance." *Transactions of ASME* 472-478.

28 Gritsch, *M*., Schulz, A., and Wittig, S., "Adiabatic Wall Effectiveness Measurements of FIlm-Cooling Holes with Expanded Exits." *Journal of Turbomachinery*, 1998: 549-556.

29 Ninniger, J. E., A. Kridiotis, A., Chomiak, J., Longwell, J. P., and Sarofim, A. F., "Characterization of a Toroidal Well Stirred Reactor." *Twentieth Symposium on Cumbustion.* Combustion Institute, 1984. 473-479.

30 Stouffer, S., R., Justinger, P. G., Heyne, L., Zelina, J., and Ballal, *D*., "Combustion Performance and Emissions Characteristics for a Well-Stirred Reactor for Low Volatility Hydrocarbon Fuels." AIAA Paper No. 2007-5663.

31 White, F. *M*., *Viscous Fluid Flow*, 3rd Edition, McGraw-Hall, 2005.

32 *Hastelloy X Alloy*, Haynes International, Kokomo, Indiana, H-3009C, <http://www.haynesintl.com/pdf/h3009.pdf>, 1997.

REPORT DOCUMENTATION PAGE

Form Approved
OMB No. 074-0188

1. REPORT DATE *(DD-MM-YYYY)*	**2. REPORT TYPE**	**3. DATES COVERED** *(From – To)*
26-03-2015	Master's Thesis	October 2013 – March 2015

TITLE AND SUBTITLE
Overall Effectiveness Measurement at Engine Temperatures with Reactive Film Cooling and Surface Curvature

5a. CONTRACT NUMBER

5b. GRANT NUMBER

5c. PROGRAM ELEMENT NUMBER

6. AUTHOR(S)

Lynch, Andrew J., Second Lieutenant, USAF

5d. PROJECT NUMBER

5e. TASK NUMBER

5f. WORK UNIT NUMBER

7. PERFORMING ORGANIZATION NAMES(S) AND ADDRESS(S)
Air Force Institute of Technology
Graduate School of Engineering and Management (AFIT/ENY)
2950 Hobson Way, Building 640
WPAFB OH 45433-8865

8. PERFORMING ORGANIZATION REPORT NUMBER
AFIT-ENY-MS-15-M-244

9. SPONSORING/MONITORING AGENCY NAME(S) AND ADDRESS(ES)
Spectral Energies
5100 Springfield St, Suite 301, Dayton, OH 45431
(937)256-7733
contact@spectralenergies.com
POC: Dr Sukesh Roy

10. SPONSOR/MONITOR'S ACRONYM(S)

11. SPONSOR/MONITOR'S REPORT NUMBER(S)

12. DISTRIBUTION/AVAILABILITY STATEMENT
DISTRIBUTION STATEMENT A: APPROVED FOR PUBLIC RELEASE; DISTRIBUTION UNLIMITED

13. SUPPLEMENTARY NOTES
This work is declared work of the U.S. Government and is not subject to copyright protection in the United States.

14. ABSTRACT

The thesis presented here details the design, construction and initial testing of rig for use with high temperature film cooling testing. The film cooling rig was supplied with hot mainstream gas from a well-stirred reactor operating on a propane/air mixture capable of multiple equivalence ratios. The Hastelloy test plates contained an internal cooling channel to allow for overall effectiveness measurements. Thermocouples on both the freestream and internal surfaces of the test plate provided temperature differences for heat flux calculations. The test plates had a quarter circle leading edge with a tapered trailing edge to provide surface curvature for the film cooling studies. The height of the test channel could be adjusted for multiple Mach numbers to be set for the mainstream flow. Using a plate containing five rows of holes in trenches and two rows of showerhead holes, methodology was developed for collecting and analyzing the necessary data to obtain net heat flux reduction and overall effectiveness results. This methodology was then applied to the same plate to gather comparative results for reacting versus non-reacting film cooling.

15. SUBJECT TERMS
Reactive Film Cooling

16. SECURITY CLASSIFICATION OF:			**17. LIMITATION OF ABSTRACT**	**18. NUMBER OF PAGES**	**19a. NAME OF RESPONSIBLE PERSON**
a. REPORT	**b. ABSTRACT**	**c. THIS PAGE**			Polanka, Marc *D.*, PhD, USAF ADVISOR
U	**U**	**U**	**UU**	145	**19b. TELEPHONE NUMBER** *(Include area code)* (937) 785-3636, ext 4714 (marc.polanka@afit.edu)

Standard Form 298 (Rev. 8-98)
Prescribed by ANSI Std. Z39-18